technische universität
dortmund

DISSERTATION

Spin noise spectroscopy from the perspective of scattered light and noise formation principles in variety of systems

From the Faculty of Physics
the Technical University of Dortmund
approved dissertatio
to obtain the degree
Dr. rer. nat.
from

Kamenskii Aleksandr
from Saint Petersburg, Russia
Stud.ID 208136

Advisor: Priv.-Doz. Dr. Alex Greilich

Dortmund, Germany
2024

technische universität
dortmund

DISSERTATION

Spinrauschspektroskopie aus der Perspektive des Streulichts und der Rauschbildungsprinzipien in einer Vielzahl von Systemen

Von der Fakultät für Physik
der Technische Universität Dortmund
genehmigte Dissertation
zur Erlangung des Grades
Dr. rer. nat.
von

Kamenskii Aleksandr
aus Sankt Petersburg, Russland
Matr. 208136

Gutachter: Priv.-Doz. Dr. Alex Greilich

Dortmund, Deutschland
2024

Abstract

This work is dedicated to a tool to get information about the spin system ground state with the help of optics: spin noise spectroscopy. Its primary goal is to characterize the virtually undisturbed spin dynamics by obtaining parameters of spin fluctuations in thermal equilibrium.

The homodyne detection scheme with phase stabilization is utilized to improve the responsiveness of the polarization analysis in spin noise spectroscopy. By providing power to the local oscillator, it is possible to overcome the electronic noise and effectively increase the acquired signal - without additional disturbance in the probed spin system while the beam bypasses the sample. This possibility allows the work with lower probing power densities, approaching the desired nonperturbing regime. An improvement larger than half an order of magnitude is present for a bulk n-doped GaAs for small probe intensities. Phase manipulation and stabilization make it achievable to choose the desired parameter - Faraday rotation, ellipticity or a mixture - from the experiment. It avoids otherwise necessary modifications in the arrangement of the optical components.

This improved technique examine further the fundamental characteristics of the spin noise signal construction by obtaining various angular dependencies of the scattered light. The distributed Bragg reflector forming a microcavity amplifies the light-matter interplay, making it possible to detect spin noise from an ensemble of n-doped (In, Ga)As/GaAs quantum dots reliably and extract weak effects. As a proof of principle, we performed an observation of pure scattered field (outside of the transmitted light aperture), as well as extraction of the primary electron spin properties, g-factor and spin dephasing time. We also studied the impact of the microcavity on the spatial and spectral dispersion of the scattered light intensity. Additionally, the interplay of two beam resonance excitation was considered for the potential signal enlargement capabilities.

From that point, the interest in the work is shifted in the direction of probing new systems and their characterization. The fundamentals of the spin noise spectroscopy is transcription of the spin-system magnetization on the angle of the Faraday rotation, which should be sufficient to be measurable. The presence of such a sufficiency can not be extracted from linear magneto-optical effects, which is especially crucial in inhomogeneously broadened systems, exhibiting the *spin noise gain effect*. In this part, the connection between the *spin noise gain effect* and the behavior of the *nonlinear resonant* Faraday effect is established, allowing us to predict the applicability of the spin noise spectroscopy to this type of paramagnet. The experimental evidence is based on intraconfigurational ($4f$-$4f$) transitions of the trivalent rare-earth ions of neodymium and ytterbium in fluorite-based crystals, approving the theoretical estimations.

At last, spin noise spectroscopy is applied to materials conventionally studied by means of the electronic paramagnetic resonance spectroscopy – dielectrics with paramagnetic impurities, which were thought of as inapplicable for the spin noise spectroscopy before. Such belief was founded on their low specific Faraday rotation for strong optical transitions. This work demonstrates that for forbidden intraconfigurational transitions, one can see the spin noise spectroscopy due to the *spin noise gain effect*, which is proportional to a relation of inhomogeneous linewidth to the homogeneous one and can be as high as $\sim 10^8$ in the mentioned system. The requirements for the optical setup to unlock such measurements are discussed, along with the potential applications. Finally, a method is present to simplify the identification of obtained spectra components. Due to the discovered fact that the sum of squares of the magnetic resonance frequencies stays the same for any direction of the magnetic field in cubic crystals with anisotropic impurity centers, if the magnitude of the field is constant, one can match the peaks to corresponding types of centers. The relation between the invariant and the g-tensor components were derived for various kinds of centers and proofed experimentally with the spin noise spectroscopy on a cubic CaF_2-Nd^{3+} crystal.

Zusammenfassung

Diese Arbeit ist einem Werkzeug gewidmet, das mit Hilfe der Optik Informationen über den Grundzustand von Spinsystemen liefert: der Spinrauschspektroskopie. Ihr Hauptziel ist es, die praktisch ungestörte Spindynamik zu charakterisieren, indem die Parameter der Spinfluktuationen im thermischen Gleichgewicht ermittelt werden.

Das Homodyn-Detektionsverfahren mit Phasenstabilisierung wird eingesetzt, um die Reaktionsfähigkeit der Polarisationsanalyse in der Spinrauschspektroskopie zu verbessern. Durch die Erhöhung der Leistung des lokalen Oszillators werden das elektronische Rauschen überwunden und das erfasste Signal ohne zusätzliche Störungen im untersuchten Spinsystem effektiv erhöht. Diese Möglichkeit erlaubt die Arbeit mit niedrigeren Leistungsdichten. Eine Verbesserung von mehr als einer halben Größenordnung ist für ein n-dotiertes GaAs bei kleinen Sondenintensitäten nachgewiesen. Durch Phasenmanipulation und Stabilisierung wird den gewünschten Parameter - Faraday-Rotation, Elliptizität oder eine Mischung - aus dem Experiment gewählt. Es vermeidet ansonsten notwendige Änderungen in der Anordnung der optischen Komponenten.

Mit dieser verbesserten Technik werden die grundlegenden Eigenschaften der Konstruktion des Spinrauschensignals weiter untersucht, indem verschiedene Winkelabhängigkeiten des gestreuten Lichts ermittelt werden. Ein verteilte Bragg-Reflektor verstärkt die Wechselwirkung zwischen Licht und Materie. Der ermöglicht das Spinrauschen eines Ensembles von n-dotierten (In, Ga)As/GaAs-Quantenpunkten zuverlässig zu erfassen und schwache Effekte zu extrahieren. Als Grundsatzbeweis sind eine Beobachtung des reinen Streufeldes (außerhalb der Durchlichtapertur) sowie die Extraktion der primären Elektronenspineigenschaften, des g-Faktors und der Spin-Dephasierungszeit durchgeführt. Der Einfluss der Mikrokavität auf die räumliche und spektrale Streuung der Streulichtintensität wird untersucht. Zusätzlich wurde das Zusammenspiel von Zweistrahl-Resonanzanregung für die potentielle Signalvergrößerung betrachtet.

Von diesem Punkt aus verschiebt sich der Schwerpunkt der Arbeit in Richtung der Erforschung neuer Systeme und ihrer Charakterisierung. Die Grundlage der Spinrausch-Spektroskopie ist die Transkription der Magnetisierung des Spinsystems auf den Winkel der Faraday-Rotation, die für Messbarkeit ausreichend sein sollte. Das Vorhandensein einer solchen Suffizienz kann nicht aus linearen magneto-optischen Effekten abgeleitet werden, was besonders in inhomogen verbreiterten Systemen, die den *Spinrausch-Verstärkungseffekt* aufweisen, entscheidend ist. In diesem Teil wird die Verbindung zwischen dem *Spinrausch-Verstärkungseffekt* und dem Verhalten des *nichtlinearen resonanten* Faraday-Effekts hergestellt. Dies vorhersagt der Anwendbarkeit der Spinrauschspektroskopie auf diese Art von Paramagneten. Die experimentellen Beweise bestätigen die theoretischen Abschätzungen und basieren auf intrakonfigurationalen ($4f$-$4f$) Übergängen der dreiwertigen Seltenerd-Ionen von Neodym und Ytterbium in Kristallen auf Fluoritbasis.

Schließlich wird die Spinrauschspektroskopie auf Dielektrika mit paramagnetischen Verunreinigungen angewandt. Diese Materialien, der Standard der elektronischen paramagnetischen Resonanzspektroskopie, galten bisher ungeeignet für die Spinrauschspektroskopie wegen ihrer geringen spezifischen Faraday-Rotation für starke optische Übergänge. Diese Arbeit zeigt die Spinrauschspektroskopie auf verbotenen intrakonfigurationalen Übergängen aufgrund des *Spinrausch-Verstärkungseffekts*, der proportional zum Verhältnis der inhomogenen Linienbreite zur homogenen Linienbreite ist und in dem genannten System bis zu $\sim 10^8$ betragen kann. Die Anforderungen an den optischen Aufbau sowie die möglichen Anwendungen werden diskutiert. Die Methode für die Identifizierung der erhaltenen Spektralkomponenten ist vorgestellt. Die Beziehung zwischen den Invarianten und den g-Tensorkomponenten wurden für verschiedene Arten von Zentren abgeleitet und experimentell mit der Spinrauschspektroskopie an einem kubischen CaF_2-Nd^{3+}-Kristall nachgewiesen.

Acknowledgments

I express my most profound appreciation to Prof. Dr. Manfred Bayer, Prof. Dr. Marc Aßmann and Priv.-Doz. Dr. Alex Greilich for the opportunity to perform the studies, gentle guidance and support.

I'm incredibly grateful to the International Collaborative Research Center, supported by the German Research Foundation (Deutsche Forschungsgemeinschaft) TRR 160, for funding the research project.

Special thanks for the productive collaboration, scientific discussions and help go to Valerii Zapasskii, Gleb Kozlov, Mihail Petrov, and Scott Crooker.

I want to extend my sincere thanks to the non-scientific staff of the chair - Lars Wieschollek and Daniel Tüttmann for the daily technical support, helium supply and recovery maintenance, Michaela Wäscher and Katharina Goldack for the administrative help, and the staff of the preparation lab - Dirk Schemionek and Gisela Pike for the sample processing.

I am grateful to all my colleagues from the chair of experimental physics 2 for the supportive and friendly atmosphere at work and during recreational activities.

I am also thankful to Mikhail Glazov for his introduction to the topic, my colleague Ivan Khakhalin for sharing provided opportunities, and all the friends, who guided me on this hard way.

Last but not least, I thank my mother Tatiana and my soulmate Lena for all the love, support and understanding.

Aleksandr Kamenskii
2024

Contents

1 Motivation

1.1 General introduction

Spin Noise Spectroscopy (SNS) is a method in development; there are still lots of white places, which need to be addressed. The working principle of SNS can be explained as an impact of magnetization fluctuations on (linear) polarization of laser light by means of the Faraday rotation. SNS is promising due to its principally non-perturbing measurement, which can be used to study relaxation processes of the system in its ground state. In this thesis, SNS is applied on bulk semiconductor and semiconductor nanostructures to deepen the understanding of the SN signal formation. This work also aims for pioneering SNS by extending the class of SNS applicable systems by crystals doped with rare earth ions.

1.2 Main goals

Our main goal is two-fold. First, the nature of the SN and how does it function in different conditions. Second, to extend the class of SNS applicable systems. To fulfill the first part of the goal, we have set the following tasks:

(a) achieve a high polarimetric sensitivity by implementation of the homodyne detection,

(b) proof the scattered nature of SN and scattered light modification by DBR,

To achieve the second goal, we have set the following tasks:

(c) find a connection between Faraday rotation spectrum and SNS applicability,

(d) implement SNS on a system with a high value of *the gain factor*[1].

1.3 What's known about SNS already

There are several reviews [90, 31, 79] that have extensively covered both experimental and theoretical advances in SNS as of 2017, the short extract is given below.

In 1981, more than 40 years ago, Valerii Zapasskii and Eugene Aleksandrov [4] were the first who observe the magnetic resonance in an optical Faraday rotation noise spectrum on atomic vapors. From this alone, it is deduced that the SN signal does not require spin-system polarization. Therefore, an insignificant (as in high temperatures or low magnetic fields) population difference between spin sublevels did not impede the SN resonance detection.

In 2005, Michail Oestreich and his colleagues [65] were the first to use SNS in a semiconductor system -bulk n-doped GaAs. Following conclusions from their article are important for this thesis: (a) Extracted values for g-factor and lifetime of localized donor bound electrons confirmed that SNS

[1] Inhomogeneous to homogeneous linewidth ratio, introduced in publication[89]

can probe a system leaving it unperturbed in a thermodynamical equilibrium in contrast to pump-probe technique. (b) In the SN spectroscopy, electron paramagnetic resonance (EPR) measurements are not strictly bound to any determined frequency, as is normally the case in conventional EPR spectroscopy; one can acquire panoramic EPR spectra over a wide spectral range at once. (c) The main drawback was the accumulation time, 62 averages of 10 minute intervals.

The use of Fast Fourier Transformation-based (FFT) spectrum analyzer allowed Roemer et al. to "reduce the measurement time by more than two orders of magnitude" [71]. Now, one could get comparable signal-to-noise ratio in less than 5 minutes instead of 120 minutes.

Later on Field Programmable Gate Array-based (FPGA) spectra analyzer appeared to reduce measurement dead-time to zero, the fast Fourier transform of the digitized signal was performed in real time. These FPGAs were produced for the needs of astronomers, but they fully enabled the SNS on semiconductor nanostructures, Crooker et al. pioneer measurements on InGaAs quantum dots in 2010 [16]. Four years later a single quantum well [69] and a single quantum dot [19] was measured by SNS. An extensive study on quantum dots from the viewpoint of perturbativity of SNS is done by Glasenapp et al. [26].

In 2009, it was shown that SNS posses the abilities of nonlinear methods, with no nonlinear effects taking place. Roemer et al [70] were able to capture a Z-scan of a sample. This spin noise technique provides the electron paramagnetic resonance (EPR) spectroscopy with more degrees of freedom than classical EPR implementation has. The use of optical access grants spectral selectivity for the studied system and high spatial resolution both laterally and in depth (three-dimensional tomography). In the same year, it was shown by Mueller et al. [62] that a 80 MHz pulsed laser can be used to implement heterodyne detection for SNS beyond the detector bandwidth.

Starting from 2010, several milestones in SNS theory were introduced. First, Kos and co authors [42] developed extensive theoretical description of the SNS for both systems that had been studied to that moment: atomic vapors and conduction electrons in semiconductors. Two years later, Glazov and Ivchenko [27] added theoretical explanation of SNS in QDs. Later, a theoretical proposal of a two-beam SNS was made by Pershin et al. in [66] for the detection of spatial correlations. Then Kozlov et al. [44] published a more experiment-oriented theoretical extension, where the second beam is not collinear to the main one.

Finally, in 2015 Glazov and Zapasskii [28] made sophisticated comparison between SNS and spin-flip Raman scattering (SFRS) theory. It was shown in 1983 by Gorbovitskii and Perel [29] that SNS can be explained by forward-Raman-scattered light, not only as Faraday rotation in the media due to fluctuation of magnetization. The first scattered-light-related experiment was made by Cronenberger et al. [13], as they observed atomic-like SNS in solid state.

One of the goals of this work was inspired by a recent article of Cronenberger [12], in which the implementation of a homodyne detection seemed to provide extra amplification for the noise of Faraday rotation in addition to the regular Faraday rotation amplification in Ref [51]. It was also shown for the bulk semiconductor that in the scattered light one can pick different angular components.

Published concurrent to the thesis

Theoretical description of two-beam SNS with a tilted auxiliary beam was applied in experiment by Kozlov et al. [45] for Cs atomic vapor.

In parallel to the course of this work, article ”optical amplification of SNS via homodyne detection” [82] was published by Sterin et al. The results of their investigation strongly overlaps with materials of this thesis, with major difference in the studied system, which was vapor of rubidium atoms (Rb).

One more significant publication in the time of writing this work is Cronenberger et al. [14], where measurements on bulk CdTe were performed on the scattered nature of SNS signal formation, as they choose a part of aperture to interfere with local oscillator.

1.4 Literature review for the second part of the work

Literature review for this work should be supplemented by publications related to Faraday rotation, which is intensively used for the second part of experimental chapters.

First of all, optical amplification of Faraday rotation signal was shown in experimental work of Laforge et al. [51].

Faraday rotation cross section was introduced later by Giri et al. [24].

Theoretical connection of Faraday rotation with its noise was developed by Zapasskii et al. [89], the gain factor was also introduced in that work. The effect of spin-noise gain, which should be observable in many paramagnetic impurities with not completely filled electronic shells, could widen the class of objects to which SNS can be applied, and thus enhance the potential of EPR spectroscopy for studying impurity paramagnets.

Another significant research made by Zapasskii and Kozlov [86] was about field dependencies of FR for rare-earth elements (REE) and modulation magneto-optical spectroscopy. Two years later Zapasskii [87] addressed the applicability of SNS to REE by comparison of the expected signal amplitude to already studied systems. Based on the regular Faraday response, SN should lie well below the detection limit of current experimental setups. Along with this, from point of spin noise spectroscopy, there is the gain factor, and theoretically REE can have a gigantic (up to 10^8) gain factor on their forbidden transitions: homogeneous linewidth can be as low as hertz at helium temperatures and their inhomogeneous linewidth is in gigahertz range.

2 Theory

Matter consists elementarily of electrons, protons, and neutrons. Its macroscopic properties are defined by electromagnetic forces. Essential microscopic parameters for the definition of particle dynamics are mass m, electric charge q, and elementary intrinsic angular momentum, spin $\vec{S}$.

2.1 Spin noise

Spin $\vec{S}$ is an intrinsic angular momentum that appears only in quantum mechanics. Each rotation with angular momentum $\vec{L}$ produces a magnetic moment $\vec{\mu}$, linked via a gyromagnetic ratio γ:

$$\vec{\mu} = \gamma \cdot \vec{L}, \gamma = g\frac{q}{2m} \tag{2.1}$$

The gyromagnetic ratio γ has a very important co-factor, the Lande factor g. It is unity in classical physics, but varies in quantum physics for (quasi-)particles, defining their response to a magnetic field. In the macrosphere, the collective response of spins to a magnetic field $\vec{B}(t)$ is a magnetization $\vec{M}(t)$, its dynamic was empirically described by Bloch [10]:

$$\frac{\partial}{\partial t}\begin{pmatrix} M_x(t) \\ M_y(t) \\ M_z(t) \end{pmatrix} = \gamma \begin{pmatrix} M_x(t) \\ M_y(t) \\ M_z(t) \end{pmatrix} \times \begin{pmatrix} B_x(t) \\ B_y(t) \\ B_z(t) \end{pmatrix} - \begin{pmatrix} \frac{M_x(t)}{T_2} \\ \frac{M_y(t)}{T_2} \\ \frac{M_z(t)-M_0}{T_1} \end{pmatrix} \tag{2.2}$$

M_0 is the magnetization value in thermodynamical equilibrium for the given external magnetic field. After deviation, this equilibrium is approached exponentially with a characteristic time T_1, called a spin lifetime or a longitudinal relaxation time. Second time constant in this picture is T_2, called a transversal relaxation time. The latter is responsible for the dephasing via rotation of the polarization direction with a Larmor frequency $\omega_L = \gamma B$. The linear response of a system magnetization to an external magnetic field $\vec{B}(t)$ can be described by the medium susceptibility function $\chi(t)$ as $\vec{M}(t) = \chi(t)\vec{B}(t)$.

In absence of external magnetic field, there are thermally exited magnetization fluctuations, denoted as δM. Dynamics of such fluctuations follow the same Bloch equations as magnetization itself. This fact is founded by fluctuation-dissipation theorem: a thermal fluctuation of a physical variable decays as if it is an external perturbation. Experimentally, these fluctuations are visible as noise. From this noise by means of mathematics we can extract information: fluctuation-dissipation theorem gives a connection between the imaginary part of the Fourier transform $\hat{\chi}(\omega)$ of the medium susceptibility $\chi(t)$, thermal energy $k_B T$, and the two-sided power spectrum $S_{zz}(\omega)$.

$$S_{zz}(\omega) = \frac{2k_B T}{\omega}\mathrm{Im}[\hat{\chi}(\omega)] \tag{2.3}$$

As power spectral density is equal to a squared absolute value of a Fourier transform, we use Fast Fourier to more efficiently accumulate spin noise and separate it from other noises. Fourier transform of a decaying sine wave has a Lorentzian profile, therefore we can expect spin noise to have exactly this profile.

Kos et al. [42] performed a more detailed theoretical derivation and analysis, which accounts for moving fermions. A general formula for a spin noise power spectrum is given by:

$$S_{zz}(\omega) \simeq \frac{\pi}{2} \coth \frac{\omega_L}{2T} \frac{M_x^{(0)}}{g\left(t_{tr}^{-1}, \tau_s^{-1}\right)} f\left(\frac{\omega - \omega_L}{g\left(t_{tr}^{-1}, \tau_s^{-1}\right)}\right) \tag{2.4}$$

Equation contains the equilibrium magnetization $M_x^{(0)}$ of the analyzed volume induced by permanent magnetic field B_x. Time constant t_{tr} denotes the duration of fermion transfer trough the probed volume, time constant τ_s stands for the spin-decay time. Function f describes peak profile, f is normalized to have a unit width and height, peaking at zero. Peak width function g tends to yield the larger value between its two arguments.

	$R < v\tau(ballistic)$	$R > v\tau(diffusive)$
$k_BT < E_F$ (degenerate)	Trapezoidal (for $\hbar\omega_L/2 < E_F$) Parabolic (for $\hbar\omega_L/2 > E_F$)	Lorentzian
$k_BT > E_F$ (classical)	Gaussian	Lorentzian

Table 2.1. The noise spectral lines' shapes in the four regimes are outlined for the case of an infinite τ_s.

2.2 Optical spin noise spectroscopy (SNS)

There are several ways for the detection of the spin noise. First realizations relied directly on the radio frequency transitions between spin sublevels in a strong magnetic field - nuclear magnetic resonance (NMR) and electron paramagnetic resonance (EPR) methods.

Alternatively, one can use Faraday effect: tilt of the linear polarization maps magnetization fluctuations as laser beam passes through the medium. A magnetic resonance in the Faraday-rotation noise spectrum was detected in 1981[4], but it was shown a couple years later in Ref. [29] that process can be viewed as interference of (Raman) light scattering (on spin energy levels) with transmitted light (red arrow in Figure 2.2). Glazov and Zapasskii [28] made careful theoretical comparison between optical spin noise spectroscopy and spin-flip Raman scattering. Schematically, the main difference is the order of detection (PD) and spectral analysis (SA), as shown in Figure 2.2.

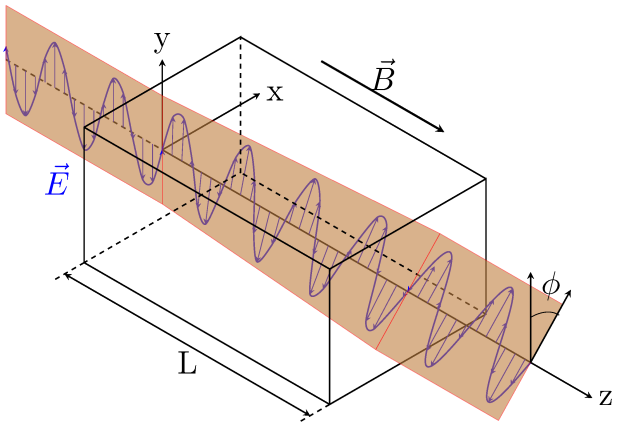

Figure 2.1. Faraday effect: polarization plane is tilted by ϕ degrees after passing the medium length L with magnetic field B applied.

From the Faraday rotation point of view, spins precess around the magnetic field along x-axis, thus having an oscillating projection on light wave vector along z-axis. This rotation occurs at Larmor frequency ω_L. From the spin-

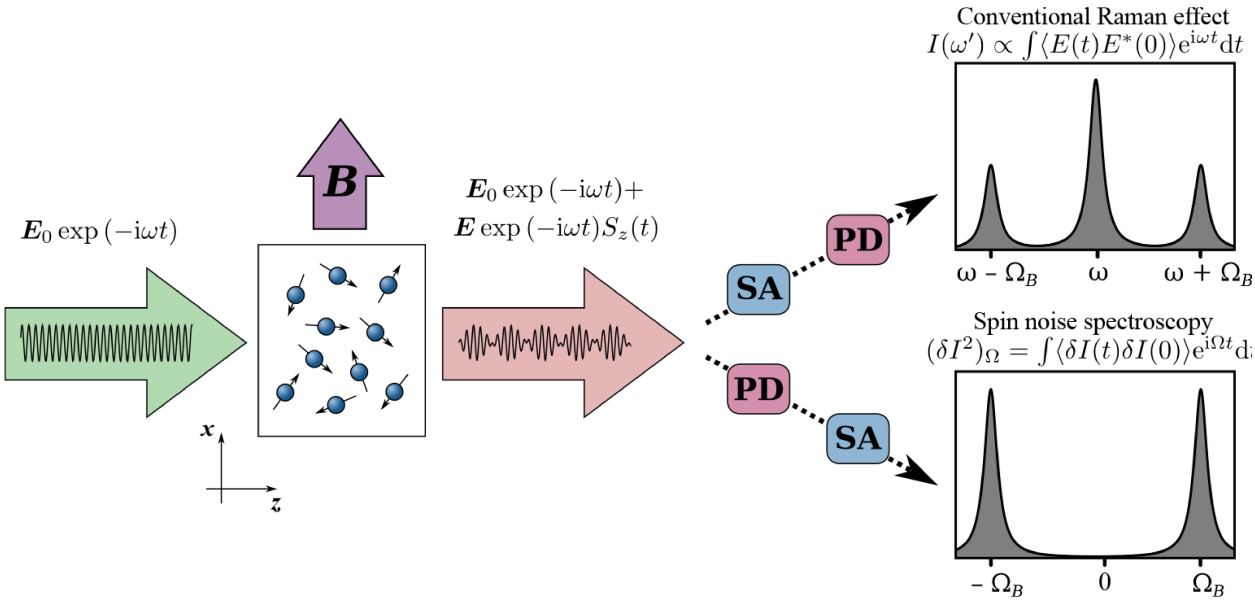

Figure 2.2. Probe beam (green arrow) goes trough the sample and gets a component from a spin noise $S_z(t)$ (red arrow). SA stands for spectrum analysis, PD is photodetection [28].

flip Raman scattering point of view, light is scattered by a spin carrier to the orthogonal linear polarization with energy shifted by Larmor precession quanta Ω_B.

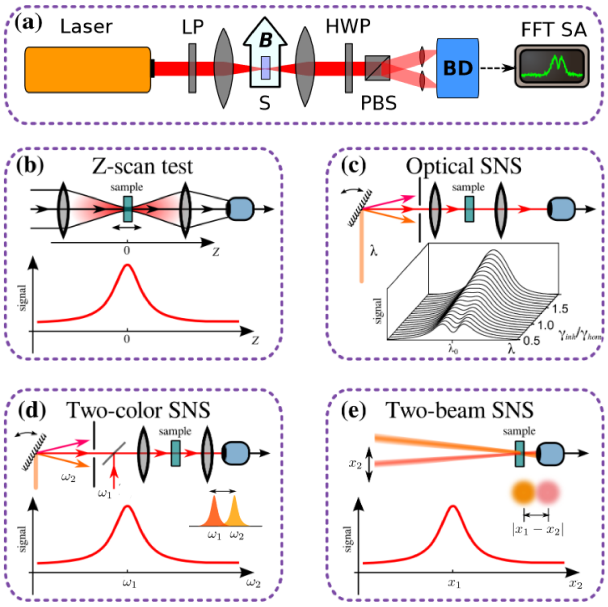

Figure 2.3. The demonstration of advances of SNS over linear spectroscopies due to sensitivity for a inhomogeneous to homogeneous broadenings ratio [28].

As shown in Figure 2.2, spin noise spectroscopy relies on intensity I rather then the electric field E of the light. Therefore, we can detect nonlinear behavior even when the intensity is insufficient to reveal nonlinear effects. Examples of SNS advantages over linear spectroscopies are shown in Figure 2.3. Figure 2.3 (c) is of the special interest. It illustrates how the SN amplitude depends on wavelength in the vicinity of an optical transition for various ratios(ε) of inhomogeneous broadening to homogeneous one. We see in Figure 2.4 (a) that the spectral profile changes from a double-peaked to a single-peaked as ε grows above unity. The highest amplitude is located at a transition center for the high values of ε and at half linewidth detuning from that transition center for small values of ε.

ε defines not only the spectral position of maximal SN, but also its amplitude. As seen in Figure 2.4 (c), the amplitude of spin noise is enhanced with rising ε. From this, ε acts as a spin noise gain factor and will be denoted further as such.

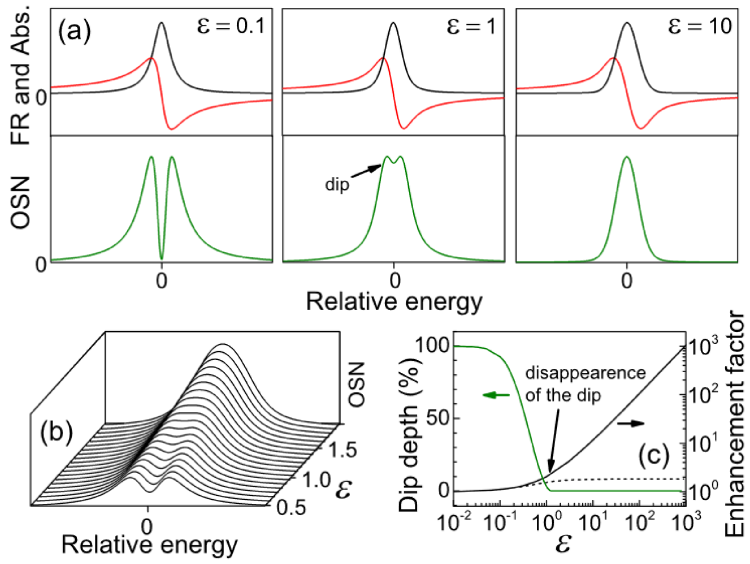

Figure 2.4. Spin noise spectral shapes for different ratios of inhomogeneous to homogeneous broadening(ε) [89].

Here we review an energy diagram of optical transition as a reminder of broadening types. The Figure 2.5 shows two-level system with ground state E_1 and exited state E_2. Lifetime of an exited state defines the homogeneous linewidth of transition, shown as a narrow blue Lorentzian curve on the right.

An ensemble of identical two-level systems shows a broader linewidth, if each system is in a different surrounding: transition energy $\hbar\omega_i, i = 1..N$ will be different from the unperturbed value $E_2 - E_1 = \hbar\omega_0$. Such broadening is called an inhomogeneous Γ, and can be much larger than the homogeneous linewidth, as shown in Figure 2.5. This circumstance as long as independent and identical distribution determines the Gaussian shape of a transition for the whole ensemble. Inhomogeneous broadening also enhances spin relaxation rate via dephasing, resulting transverse spin relaxation time is denoted as T_2^*.

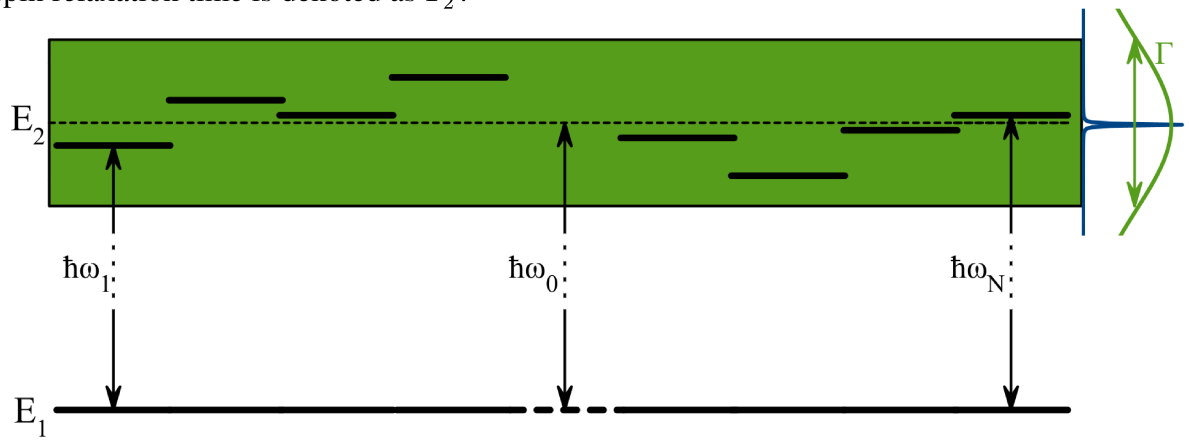

Figure 2.5. A schematic representation of the inhomogeneous broadening of a two-level system. The ensemble of isolated two-level systems can have different absorption maximum energy due to the local environment's influence. If one fixes the ground state, it can be viewed as a variation of the position of the exited level. Such a broadening is inhomogeneous and can exceed the homogeneous one by many orders of magnitude.

2.3 Faraday rotation (FR)

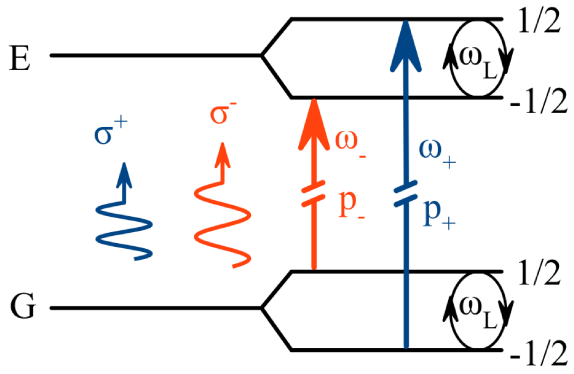

Figure 2.6. The most straightforward energy level diagram of a half-integer spin (Kramers) impurity ion in a magnetic field with G being the ground and E the excited states correspondingly. $\pm 1/2$ mark the spin levels split by a longitudinal magnetic field (ω_L).

As chapter 6 refers to nonlinear Faraday rotation, fundamentals of FR are presented below.

It is commonly known that the classical approach for the calculation of the rotation angle ϕ is the difference of the refraction $n_{\pm}(\omega)$ for the right- and left- circular polarization components $\sigma_{\pm}$ of the traveling wave:

$$\phi = \frac{\omega l}{c}\Big[n_{+}(\omega) - n_{-}(\omega)\Big], \qquad (2.5)$$

with the optical frequency of the probe beam ω, the sample length l, and the speed of light c.

As follows from the value of the photon spin, only those possible transitions of impurities commit to the refractive index $n_{+}(n_{-})$, which cause the change of the angular momentum projection on the light k-vector by one $\Delta M = \pm 1$, shown in Figure 2.6. With no magnetic field present, $B = 0$, situation becomes degenerate for the both polarizations (transition energies coincide $\omega_{\pm} \equiv \omega_0$, no population difference as well $p_{\pm} \equiv p$), therefore no FR present, $\phi = 0$.

At any nonzero magnetic field, the Zeeman splitting is present and it matches to the Larmor frequency $\omega_L \equiv g\mu_{\mathrm{B}}B/\hbar$, g is characteristic magnetic splitting for the chosen ion, μ_{B} is the Bohr magneton, and $\hbar$ is the reduced Planck constant. The frequencies and populations are not equal anymore:

$$\omega_{\pm} = \omega_0 \pm \omega_L, \quad p_{\pm} = p \pm \hbar\omega_L/2k_{\mathrm{B}}T, \qquad (2.6)$$

k_{B} being the Boltzmann constant, and T - the temperature (Equation 2.6 is given in the approximation of $\hbar\omega_L/2k_{\mathrm{B}}T < 1$). If one thinks of a system without inhomogeneous broadening, the central frequency for each element of it equals to ω_0, and expression may be rewritten:

$$n_{\pm}(\omega) = \frac{2\pi \mathrm{d}^2}{\hbar} N p_{\pm}\, f(\omega_{\pm} - \omega) = \frac{2\pi \mathrm{d}^2}{\hbar} N[p \pm \hbar\omega_L/2k_{\mathrm{B}}T] f(\omega_0 \pm \omega_L - \omega), \qquad (2.7)$$

with the dipole moment d of the optical transitions $\sigma_{\pm}$, and the concentration of the impurity centers N. The function f stands for the frequency dependence of the refractive indices $n_{\pm}(\omega)$, which is Lorentzian for the homogeneously broadened optical transition [42]:

$$f(\omega) = \frac{\omega}{\omega^2 + \gamma_h^2}, \qquad (2.8)$$

γ_h being the width of the homogeneously broadened transition. Equation 2.7 omits the refraction of the background, which is everything beyond the taken into account transition.

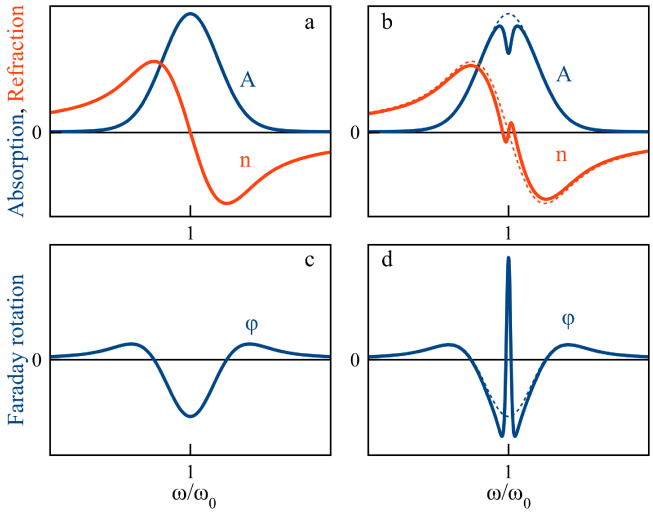

Figure 2.7. (a) and (b) absorption (A) and refraction (n) spectra of an isolated inhomogeneously broadened optical transition; (b) for the transition with a spectral hole burnt by monochromatic laser light. (c) and (d) corresponding spectra of diamagnetic FR (ϕ). The spectra of the transition with a spectral hole are supposed to be measured with an additional light source.

For the case of small magnetic fields (so that $\hbar\omega_L < \hbar\gamma_h, k_\mathrm{B}T$) FR angle is proportional to the magnetic field and, therefore, the Larmor frequency ω_L, as follows from Equation 2.5:

$$\frac{\phi}{\omega_L} = \frac{\omega l}{c}\frac{d}{d\omega_L}\Big[n_+(\omega) - n_-(\omega)\Big]\Big|_{\omega_L=0}. \tag{2.9}$$

Taking the $n_\pm(\omega)$ from Equation 2.7, one gets:

$$\phi = \frac{V\hbar}{2k_\mathrm{B}T}f(\omega_0-\omega) - Vp\frac{\partial}{\partial\omega}f(\omega_0-\omega) \equiv \phi_C - \phi_A, \quad V \equiv \frac{4\pi \mathrm{d}^2 N}{\hbar}\,\frac{\omega_L \omega l}{c}. \tag{2.10}$$

The summand ϕ_C, commonly referred to as *paramagnetic* or *C-term* [11] originates from the difference in populations of the above-mentioned levels, and, therefore, (and from Equation 2.10) gets smaller with the rising temperature, following Curie's law. As mentioned before, the temporal behavior of this component in the changing magnetic field is limited by the time of restoration of thermal equilibrium, that is, the spin relaxation time T_1. The component ϕ_C subsides at frequencies higher than $1/T_1$. Either a high enough modulation frequency of the magnetic field [3] or a high temperature ($k_\mathrm{B}T \gg \hbar\omega_L$) allows one to ignore the part ϕ_C.

The term ϕ_A is commonly named as *diamagnetic* or *A-term* [11] and corresponds to the change in energy levels of impurity in the present magnetic field Figure 2.7 (c). As soon as it is temperature-independent and responds much faster than T_1, it will be in the focus of further analysis of experimentally obtained information in conditions of high probe power densities and inhomogeneous broadening in chapter 6.

In case of powerful resonant monochromatic excitation, a hole-burning in an inhomogeneously broadened line transforms the absorption spectra from being like in Figure 2.7 (a) to a Figure 2.7 (b), which correspondingly induce changes in the refraction and FR, the latter receives a sharp peculiarity with an opposite sign and a larger amplitude Figure 2.7 (d). Relation between the heights of the new component and the unperturbed prior one, must be somehow defined by the relation of inhomogeneous to homogeneous linewidth.

3 Experimental Methods

This chapter introduces the experimental methods used in the current work. Techniques for the sample characterization - transmission, PL and FR - are presented in section 3.1. The spin noise measurement setup is described in section 3.2.

3.1 Used techniques

The main scope of this work is spin noise spectroscopy. It requires detailed information on the spectral properties of the samples to be studied. Although the materials of samples are known, and there are sets of table parameters in the literature, one always needs to recheck that precisely this probed volume behaves appropriately. Transmission, photoluminescence and Faraday rotation measurements take place before spin noise spectroscopy.

3.1.1 Transmission

Information about absorption lines, their broadening and relative strength can be obtained from either transmission or reflection measurements as $t + r + a = 1$. We choose transmission in order to be less prone to stability issues and generally get higher levels of the signal. Additionally most of the samples are bulk material and are optimized for transmission.

The general setup to measure the transmission is given in Figure 3.1. We guide light from a source to a detector through the sample. To get a spectrum from sample we can either

1) use a source with broad spectrum and select the detected wavelength with the detector

2) use a narrow source and scan it over the desired range

We obtain the reference by moving sample out of the beam, all the other components stay the same. The difference tell us about specific only for the sample peculiarities, which in turn can be more precisely studied by a laser scan spectra, while the monochromator resolution is mostly limited by the slit width, that was 50 microns in our case.

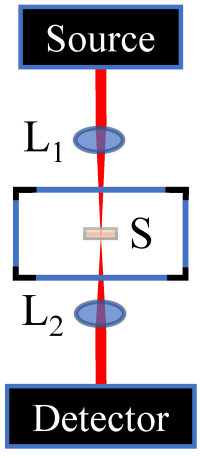

Figure 3.1. Transmission measurements setup: light from Source is focused by lens L_1 on the sample S in, then is collimated with lens L_2 for routing to the Detector.

White light transmission

We use an incandescent light bulb as a wide spectrum light source in chapter 5. Focusing guaranties that light hits only the sample. Collimated light after the sample is coupled to a multi-mode fiber. The other end of the fiber is connected to the Acton monochromator with a liquid nitrogen-cooled CCD attached to it. The diffraction grating in monochromator has 600 lines/mm and together with 1340 pixel CCD grants one-shot spectra with spectral width of ≈50 nm. Software allows to shift the center of the window and glue several separate spectra into a single one. For the reference measurement cryostat was shifted so that the light does not go through the sample (but optimally still goes through the windows of the cryostat). The spectrophotometer Cary is a commercial alternative for the scheme above, which was used in chapter 7.

Tunable laser direct absorption (TLDA)

A tunable CW Ti:Saph laser is a suitable source for tunable laser direct absorption method. This method suits for spectrum with narrow features present. The measurement goes in the following way: an intensity-stabilized laser beam is mechanically chopped at 1.5 kHz rate and is focused on the sample, the detector catches the transmitted light, and the lock-in amplifier detects signal on the chopper frequency. A computer program reads values from the wavelength meter and the lock-in amplifier simultaneously, providing one point of transmission spectrum at a time. The wavelength meter has an absolute accuracy of 0.0001 nm, which also defines the maximal achievable resolution.

To get the spectrum, we scan the laser wavelength using a cavity mirror on the piezoelectric mount. This smooth tuning provides only up to 40 GHz range, which equals 0.08-0.13 nm depending on the central wavelength. If a broader range is needed, the acquisition is stopped, the scan window is moved by rotation of either thick etalons (≈0.02 nm step, ≈1 nm range) or the birefringent filter (225 GHz (≈5 nm) step, ≈100 nm range), and then the scan is started.

For the stability of the light intensity during the scan is responsible the device from BEOC company, which is a combination of a liquid crystal retarder, a polarized beam splitter, a diode and feedback electronics. Depending on the purpose and the required accuracy, several configurations of the equipment were used:

1) a fixed ratio non-polarizing beam splitter (nPBS) before the sample, and the power meter heads one after the sample and other one in the second arm of nPBS, the reference measurement is when the head after the sample is moved in front of it.

2) a polarization detection scheme with the balanced diode, that has not only the difference output, but the monitor output from single diodes as well, in current case, Nirvana or New Focus, but for due to the fact of the almost-DC measurement, Nirvana is more preferable due to better signal-to-noise ratio (SNR) and less to no crosstalk between outputs.

3.1.2 Photoluminescence

The photoluminescence is based on the relaxation of carriers from the excited states to lower-laying ones and reveals the bright states emission. We use the photoluminescence as a way to find the right probe wavelength and a spatial position for semiconductor samples. We use in this work direct band gap materials: either bulk GaAs or InGaAs-based heterostructure.

For the case of bulk material, the lowest energy emitting state is usually an exciton bound to donor or acceptor. For the case of a heterostructure, it strongly depends on the strength of a quantum size effect. In this work the last sentence is the case for quantum dot samples.

Scheme of the setup is shown in Figure 3.2. We illuminate the sample with light from 785nm diode laser. Corresponding excitation energy is higher than the band gap, but not too high, so that absorption is close to optimum. The emitted with a lower energy light is then collected to the multi-mode fiber. The other end of the fiber is connected to the same Acton monochromator as was used in white light transmission. We used two geometries of photoluminescence collection: the reflected back - with the help of a pellicle or just from the side window of the cryostat. The latter helps to omit the influence of a 2D heterostructure on the photoluminescence spatial distribution or spectral filtering, see chapter 5 for more details.

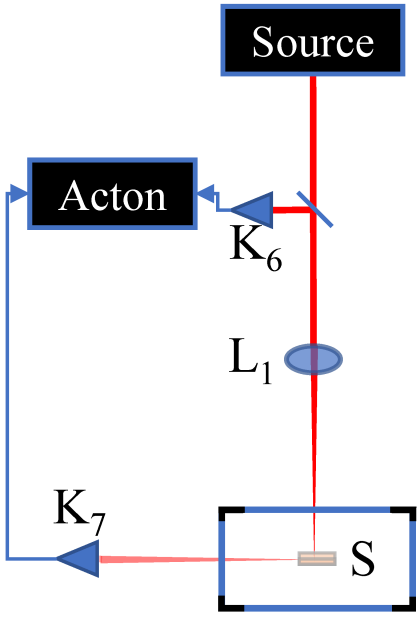

Figure 3.2. Both photoluminescence geometries used in this work: in reflection trough fiber coupler K_6 and from the side trough fiber coupler K_7. The target detector - Acton - is a monochromator with liquid nitrogen cooled CCD.

3.1.3 Faraday rotation (diamagnetic)

A Faraday rotation angle spectrum is one of the intermediate results used in parts of this work. For obtaining of a Faraday rotation we need a scheme like in subsubsection 3.1.1 with an addition of an electromagnet coils, see Figure 3.3.

The TLDA working principle - how do we scan the laser - is already described. If we want to measure FR, we need to add a controllable magnetic field source and replace a simple detector to a polarimeter scheme. As seen in Figure 3.3, a coreless electromagnet with split coils and a polarimeter based on half wave plate, Wollaston prism and a balanced photodetector are used.

For the cases, when the balanced photodetector has not only difference signal output, but a monitor one, like, for example, is Nirvana, it is possible to measure FR and absorption simultaneously.

To measure the diamagnetic part of the Faraday rotation, it is possible to use lock-in technique by modulating the magnetic field. The magnetic field modulation helps also to reduce the background electronic noise and to get a stronger response. The cut-off frequency of the modulation amplitude

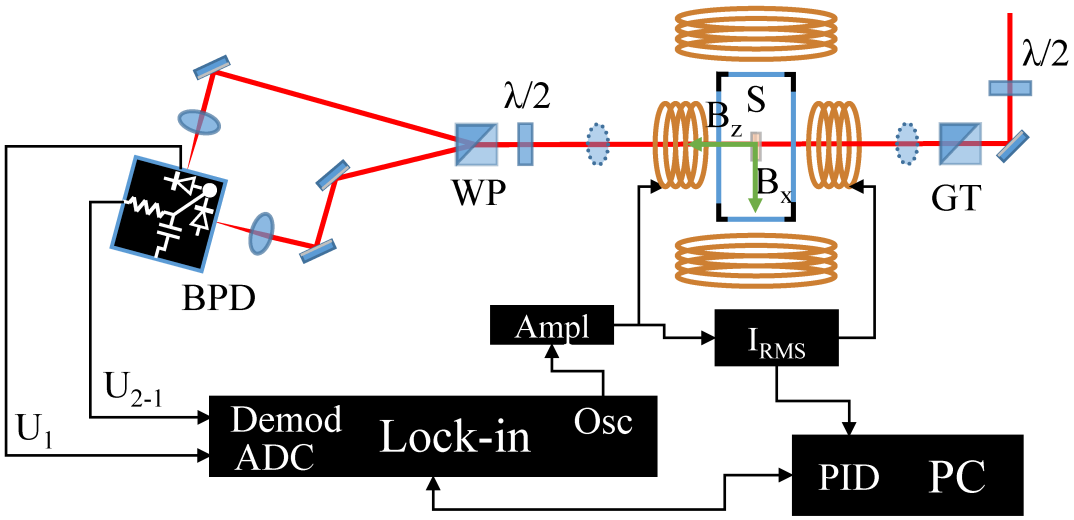

Figure 3.3. The drawing shows the experimental setup for the diamagnetic FR measurement: transmitted through the sample laser light is analyzed with the balanced photodiodes. A $\lambda/2$ and a Glan-Taylor (GT) prism after the laser allow one to control the incident power and the direction and quality of the linear polarization of the beam. A pair of lenses (L_1, L_2) were used for the high power density and were removed for the low power density measurements; the iris opened at 2 mm ensured the overlap of these regions. The audio amplifier works perfectly for 8 Ohm coils of the electromagnet and allows one to apply the AC magnetic field in the longitudinal direction with a very stable frequency, defined by the internal oscillator of the lock-in amplifier. The transmitted beam polarization is analyzed by a $\lambda/2$, and a Wollaston prism (WP), the signal from one diode (I_1) and the difference of $I_1 - I_2$ are fed to lock-in to be able to get the absolute rotation in a single measurement.

is defined by the coil inductance and equals 333 Hz. This frequency was chosen as a modulation frequency throughout the work.

The lock-in itself is a pure sinus waveform source with a precise and stable frequency. The modulation signal from the lock-in is amplified with the D-class audio amplifier to get the desired magnetic field amplitude in the electromagnet.

It is important that the current in the coil can heat it enough to change the active resistance of windings. To keep the amplitude of the magnetic field constant, we connect electromagnet through the RMS current meter. The measured value serves as process variable for PID controller, which adjusts the amplitude voltage on the lock-in output.

The results of the performed measurements discussed in details in chapter 6.

3.2 Experimental setup

3.2.1 Devices for spin noise spectroscopy

Laser system

Most of components of the laser system are pictured in Figure 3.4 above the legend and to the left of the dashed blue line. The beam starts at the diode pumped solid state laser (DPSS). The DPSS in this work is Verdi V-10 from Coherent. It uses second harmonic of Nd:YVO_4, providing up to 10 W of monochromatic 532 nm laser light. We tune the power to 8 W route it with two dielectric mirrors to pump the MBR-110.

MBR-110 is a continuous-wave single-mode single frequency tunable ring cavity Ti:sapphire laser from Coherent. It can produce coherent monochromatic light up to 1 W of power in the range from 700 to 1000 nm with linewidth below 100 kHz. In all experiments MBR-110 is the main laser source to probe the system.

The tunability of MBR-110 is guaranteed by its controller. This controller manipulates optical elements inside the MBR-110 resonator. We use it for the external wavelength stabilization and for the smooth laser scanning.

To allow the wavelength monitoring and stabilization, a wavelength meter HighFinesse WS6-600 (WS-6) receives a small fraction of the beam from MBR-110. The glass plate in the output beam reflects 4 % of the incoming intensity. The ND filter further decreases the beam power to avoid saturation and damage of WS-6. The use of polarization maintaining fiber (PMF_1) provides additional stability of WS-6 readout against mechanical vibrations.

For easier routing and to secure the single mode operation, laser emission of MBR-110 is coupled to a single-mode polarization-maintaining optical fiber PMF_2. The telescope Tel_1 expands the beam to maximize the use of coupler K_2 aperture. A faraday rotator FR blocks the back reflections from K_2, preventing lasing instabilities. A half wave plate $\lambda/2$ and a Glan-laser prism GL serve to keep the power at K_2 below its damage threshold.

On the other end of PMF_2 the laser light is collimated by K_3. The noise eater BEOC LPC-RD-40 VIS/NIR controls the transmitted intensity. BEOC serves for the beam power stabilization up to 1 kHz both for fixed and scanned wavelength of MBR-110. The last component, that defines laser beam for all schemes is telescope Tel_2. It expands the beam for a tighter focus on the sample. Tel_2

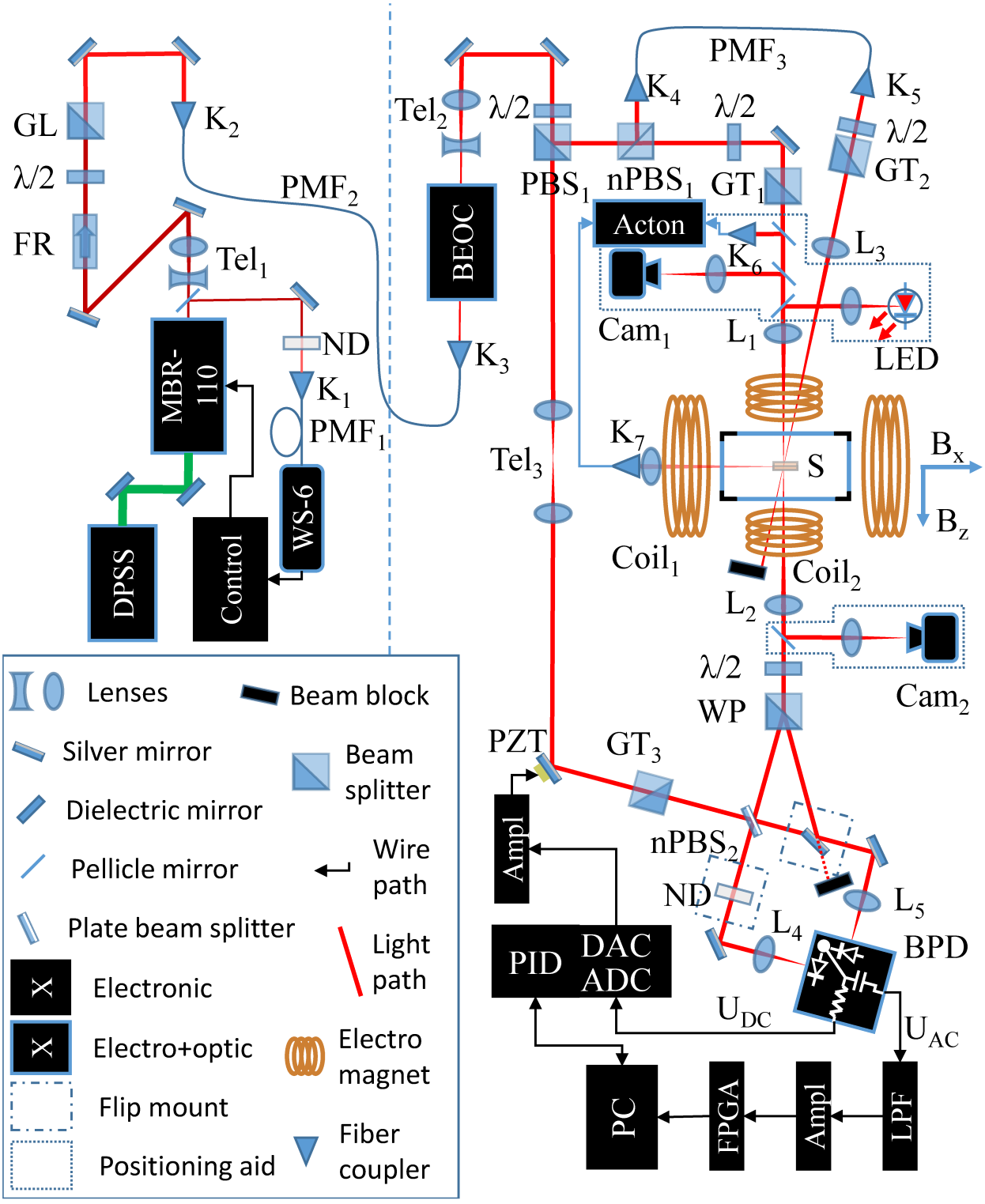

Figure 3.4. A most complete schematic of the measurement setup.

is either a combination of 2 achromatic doublets (-40 mm and +60 mm) or a single objective with adjustable focal length.

Sample environment control

In Figure 3.4 the sample S is shown in a rectangular, which represents a section of a MicrostatHe-R flow cryostat. As it is a sample-in-vacuum system, so we need a vacuum pump to prevent gas freezing on a sample during cooling down. We use a combined pumping station Pfeiffer Vacuum HiCube 80 Eco. It includes turbopump and backing pump and allows to reduce pressure in cryostat to as low as $3e^{-7}$ mbar.

Except for the sample spatial orientation, temperature and magnetic field are two the most important parameters to be controlled. There are two temperature controllers. The original one is a MercuryiTC Oxford, connected to the temperature sensor and the heater. Both of them are build in the cryostat heat exchanger. MercuryiTC helps to control the sample cool-down and can stabilize temperature above the helium one. The custom temperature controller consists of a Cernox sensor in the cold finger and a digital Keithley multimeter. Due to higher proximity to the sample, it gives a better estimation of the temperature.

To control the magnetic field a bipolar power source for the electromagnet is used. After a calibration, it allows creation of a very precise magnetic field, providing DC current up to 30 A.

Detection

The balanced photodiode (BPD) converts the incoming light into charge carriers, takes the difference of analogue currents and gives it to consumer devices as the output voltage. BPD acts as a converter of the signal from optical frequencies (≈300 THz) to the radio frequencies (from 0 to 1 GHz), in form of U_{AC}, which can be processed electronically.

We use analogue low pass filters (LPF) to limit the bandwidth of U_{AC} from 0 to 1 GHz. The LPF reduces the influence of electronic noises outside of the detection bandwidth on amplifier and prevents aliasing in FPGA board.

The amplifier (Ampl) increase the incoming signal by 20 dB in bandwidth from 0 to 1 GHz. By doing so, the amplifier matches the voltage from BPD with the full scale of ADC on the FPGA board.

The FPGA board (FPGA) has an ADC to digitize the incoming voltage with sampling rate up to 2 GS/s. FPGA itself is capable to compute and accumulate powers spectrum at rates from 0.4 to 2 GS/s in real time. Such a device is crucial for spin noise spectroscopy due to the inherent weakness of the signal in most of the systems.

At this point one can readily obtain spin noise spectra and process them on PC, but for advanced techniques we need two more devices.

The HF2LI lock-in amplifier (PID, ADC, DAC) is a multifunction device. It can be used as a normal lock-in amplifier, but it also has a precision sinus wave generator and a PID controller, shown in Figure 3.4. HF2LI serves as a simple lock-in amplifier in measurements of transmission and Faraday rotation. PID controller of HF2LI is a part of phase stabilization chain, its DAC generates the compensation signal for the PZT mounted mirror.

HF2LI solely cannot provide enough voltage to drive PZT in the full range. To overcome this we add piezo amplifier (Ampl) between DAC and PZT. Ampl multiplies by 15 the incoming voltage from 0 to 10 V in the 30 kHz bandwidth. With Ampl we are able to move the mirror on PZT for several wavelength distance to stabilize the phase.

3.2.2 Devices for characterization and check-ups

A sound amplifier (SA) is used for Faraday rotation measurements. SA can increase the voltage and the power of the incoming signal from 20 Hz to 20 kHz with no quality loss. We place this amplifier between HF2LI generator and electromagnet $Coil_2$ to protect the HF2LI from overload and to reach higher magnitude of the modulating magnetic field.

A higher magnitude requires for stabilization a root-mean-square current meter in the $Coil_2$ circuit. It can be used in a PID control loop to adjust voltage and keep RMS current constant.

A two-channel oscilloscope up to 100 MHz helps to balance the BPD based polarimeter and check signal amplitudes for safety for sensitive electronics.

A 785 nm diode laser is used only for PL measurements as excitation source. It is much more convenient to use, then to tune MBR-110 to this wavelength as MBR-110 requires the mirror change in the internal cavity.

The Acton monochromator and attached to it CCD are used for white light transmission spectra and for PL measurements. The spectral resolution is defined by the slit width and grating of the monochromator, and the CCD pixel size and spacing. The possibility to get a broad spectra at one shot make it very helpful for alignment procedures as well

3.3 Measurement protocol

In this section a complete measurement procedure is given for the ease of results reproduction.

The longest process for measurements on a flow cryostat is the vacuum pumping of the cryostat. Therefore it should be switched on first. The time dependence of the pressure shows if there is a leak. For the used devices and a pumping from atmospheric pressure, sensor readings should be less than $3e^{-3}$ mbar at one minute mark and less than $3e^{-4}$ mbar at two minutes mark. In case of series of measurements, it is reasonable to have the vacuum pump attached and running all the time except for the actual measurement time.

All electronic devices that are going to be used in experiment are switched on. The order of switching on should go from a signal source to signal consumer: first diodes, then their amplifier. The used FPGA board needs to be switched on before the computer. Other devices can be switched on in arbitrary order. Temperature transient effects take up to 30 minutes until devices reach their datasheet parameters. The laser is switched on as well, and the shutter is opened after approximately a couple of minutes, when the current has stabilized. A beam block should be present or placed at the laser output to ensure the safety of optical elements.

While the devices warm up, software for the readout and manipulation of controlled parameters is started. The value from the calibrated temperature sensor on the cold finger in the vicinity of the sample is obtained by 4-wire method every two seconds and is plotted on a live graph. The

wavelength meter and laser wavelength stabilization programs work with maximal update rate, mostly limited by the exposition time of the wavelength meter.

The next step is the transfer tube insertion and connection to the helium recovery system. The needle valve should be opened prior to insertion in the liquid helium vessel to prevent the freezing. As the transfer tube is slowly inserted in the vessel, overpressure builds up and will be used to push the liquid helium without additional pumping. When the transfer tube is hermetically sealed to helium panel, the needle valve is closed and the whole volume exposed to air is vacuumed with membrane pump. The needle valve is then opened to fill the volume with gaseous helium, and as soon as the overpressure in vessel (0.1-0.2 bar) is higher than in the recovery system, the ball-valve will allow the flow. A quarter turn from the closed position for the needle valve allows the slow and low helium consumption cooling down to 6 K given the mentioned overpressure.

This is the best time to write down the measurement plan - which dependencies are needed, what is the reasonable accumulation time, etc.

The steady state of the laser in term of the temperature regime is seen on the wavelength chart. When the change over several tens of seconds is on order of a readout noise, a PID control stabilization of the chosen wavelength is switched on.

Then we check the power level of the laser beam and the alignment of the optical setup. First point - prior to the fiber to ensure that the power does not exceed damage threshold for the fiber, in our case 300 mW at 850 nm. Second point - after the fiber to check that the coupling is efficient enough. The non-perfect mode of the laser output leads to ≈ 50 % coming out of the fully aligned fiber. Further the intensity of the beam up to 1 kHz is stabilized by BEOC at the level of 50-60 %. Further power routing and redistribution depends on the scheme used.

After the laser source part of the setup is proved, the temperature should be checked. After the liquid nitrogen temperature, we close the vacuum valve on the cryostat and shut the vacuum pump down. We know that the cryostat reached the liquid helium temperature when the temperature saturates (5.7-6 K) and the temperature variation drops down significantly to several mK. Such a regime allows also a high stability of the sample position.

Further we need to pick the point on the sample to probe with the laser beam. The coarse alignment can be performed with cameras and 3-axis kinematic mount of the cryostat. For a more precise choosing of the right spot, we use either transmission, PL or both methods. Final focus adjustments are performed with spin noise spectroscopy to maximize the spin noise amplitude.

For all spin noise measurements we need the polarimeter scheme to be balanced, but the exact way depends on the chosen scheme for SNS. There are three of them:

1) classical

2) homodyne

3) side illumination

For the classical scheme we adjust the power going to the sample so that the power on the detector will not reach the damage threshold. Then we check power in front of each eye of the balanced photodetector. If there is a difference, the half-wave plate in front of the Wollaston prism is adjusted until the difference is on order of 0.1 % of the value. Now the balanced photodetector signal should give on oscilloscope a noise trace close to zero. If it is not the case, each of the eyes adjusted individually at lower power until balance is met.

When the preparations are done, measurements can be started.

To separate the spin noise spectra from the background we need to have a reference to subtract

from. In the classical scheme the most reasonable reference is a measurement in a different transversal magnetic field.

The amplification coefficient, acquisition parameters and reference magnetic field value are selected and varied according to the observed spin noise spectra. The noise trace should occupy the maximum of the ADC full scale, but should not lead to overflow.

For the homodyne scheme we first set up the power of the local oscillator. Its intensity is chosen so that diodes will be on the edge of their linear response. Then we need to check the interference of the probe beam with LO - both the spatial and their wave fronts. As soon as we get the maximal centered bull-eye pattern, the adjustment is complete. Then solely the LO is balanced on BPD with the help of a gradient neutral filter. To select the proper polarization, we rotate the half wave plate to reach the minimum intensity of the transmitted probe beam going to interfere with LO. We scan the phase of LO by piezo mounted mirror and choose the desired phase working point, which is then PID stabilized. The P, I and D coefficients are chosen empirically for each piezo mount used.

For the side illumination we first perform the procedure for the homodyne scheme. Then we check the spatial overlap of the probe and the external beams on the sample. For the coarse alignment one uses cameras and maximization of the scattered light in the detection scheme by lock-in amplification with chopper in the external beam path. The fine tuning is done with the help of the spin noise signal itself.

Both homodyne and side illumination schemes can use as a reference measurement not only the spectra at other magnetic field, but the measurement with the blocked probe as well. It is automatized with the help of a shutter in transmitted probe path before the interference with LO.

At this point the setup is ready for the measurements. All magnetic field series measurements are automatized, and one only needs to enter the chosen range and step. The obtained and published results are presented in the experimental part: chapter 4-chapter 7.

4 The homodyne scheme for the spin noise detection

The long publication silence after the first article on SNS [4] originates from low signal-to-noise ratios in optically detected spin noise in solid materials[65]. In this chapter 4, we compare self-homodyne and homodyne techniques sensitivity in spin noise spectroscopy. The homodyne method has higher polarimetric sensitivity, which is needed to have higher SNR in SNS. Due to the reason the local oscillator (LO) laser beam does not pass through the sample, eliminating constraints on its intensity due to potential spin system perturbations. By adjusting the LO power within the photodiodes' dynamic range, we achieve a reduction in the minimal probing strength by over three times, bringing us closer to the nonperturbing regime. We approved the efficiency of the method by studying the classical semiconductor n-doped GaAs. Moreover, the stabilized manipulation of the optical phase between LO and probe laser beams enables us to measure Faraday rotation and ellipticity without changing of polarization optical components in setup.

4.1 Introduction to homodyne technique

The concept of homo- or heterodyning for amplification of the signal was developed in the beginning of radio era[20], the optical realizations are relatively young [41], their development started as soon as coherent light laser sources became widespread. In general, the idea of such a measurement setup is a direct parallel to the electrotechnical version of it: a high frequency carrier monochromatic field is modulated by a low frequency component, for detection it is mixed with a reference (local oscillator), which has either the same frequency as a carrier (homodyne) or a different one (heterodyne). The main reason to use a homo- or heterodyne scheme is to obtain an extremely high precision [52], originating from the phase sensitivity, latter allows one also to get access to the quantum optical properties of the light [77, 5, 78]. Possible applications of homodyne schemes range widely from astrophysics and detection of gravitational waves to the characterization of spin system in a cold atomic gas[60]. It can be used also for detection of a carrier spin in a variety of semiconductor materials[22, 80] or the time standard on a single ion in the magneto-optical trap[72].

This thesis focuses on spin properties of semiconductors. A classical method of studying the spin properties is pump-probe Faraday/Kerr rotation[6]. The pump creates the spin polarization of the system according to the optical selection rules. The probe then tests a system, getting its polarization changed due to the magneto-optical effects.

To study the system in the equilibrium state, one should exclude the pump, and this leads us to the spin noise spectroscopy[4, 15, 65, 89, 90, 31, 79]: a CW probe beam senses the fluctuations of the magnetization by the means of the Faraday rotation. Such fluctuations occur in a thermodynamic

equilibrium and a corresponding signal originates from a spin-flip scattering[29], causing a Raman-shift of the interacted photons, being interfered with the transmitted light[28]. As a stochastic signal, spin noise is intrinsically small and requires an excellent polarization sensitivity.

There are several ways to increase the Faraday rotation angle: one can pick a more paramagnetic material, increase the magnetic field or make the sample longer. For the latter purpose a structure under investigation can be placed into a macro-[88] or micro-[43, 69, 68] optical resonator (cavity). Linearly polarized light rotates in the same direction after each reflection, so all passes are adding up to a total Faraday rotation angle, equal to a single-pass Faraday rotation multiplied by cavity finesse.

Increasing of the probe intensity allows to improve the Faraday rotation signal. However it leads to the perturbation of the tested spin system by probe[25], which one need to avoid in the optical experiments.

Not to omit are possibilities to increase the SNR of the Faraday rotation by alternating the sample (by incorporating magnetic particles and coupling a carrier spin to it[13]) or the light (squeezing the coherent state's Poissonian statistics to sub-Poissonian one and therefore reducing the photon shot noise level[55]), both requiring the significant effort for the effective implementation.

In this part of the work, the homodyne detection of the Faraday rotation is used for combining the HPE detection[25] with a low probe power. For the first time the improvement of sensitivity by homodyne detection was shown in pump-probe technique[50, 51], variation of which was later inherited by spin noise spectroscopy[12], with an accent on the quantum-limited homodyne and heterodyne detection. The advantage of the homodyne is that the reference beam can be made as powerful as required, without interacting with the tested system, the only limit being the dynamic range of photodiodes.

With the help of Mach-Zehnder interferometer we implement a balanced homodyne technique and apply it to the well-studied system - n-doped GaAs epilayer - to compare measured spin noise spectra of electrons at the edge of the Fermi sea with results obtained by the traditional scheme. The implementation of the interferometer phase stabilization by means of optical path length control, gives access to quadrature measurements as well as long-time accumulations of the spin noise signal. The latter allowed us to increase the range of probing power densities up to three orders of magnitude for the measurements of electron-spin relaxation rates.

4.2 Sample description

A 170 μm epitaxial layer of negatively doped ($\approx 2 \cdot 10^{16}\,\mathrm{cm}^{-3}$ at 0 K) GaAs serves as an object for the study. Refs. [17, 25] contain an extensive characterization of this sample (sample B in Ref. [17]). Such background reduces unknown parameters, making the comparison between the conventional method and the newly implemented more reliable.

Additionally, the sample reveals a high SNR for spin noise power spectra. The SNR is directly connected to the resident electron spin lifetime, which is defined by the electron density. The sample is n-doped so that the electron density is close to the metal-insulator transition. As soon as donor electrons are thermally activated to the conduction band, the electron density is tunable with the temperature. The chosen sample demonstrates electron density of $3.7 \cdot 10^{16}\,\mathrm{cm}^{-3}$ at 10 K. At low temperature this sample shows the longest electron lifetime in comparison to the similar

samples [40, 21, 23]. Therefore it is a good candidate to approve the efficiency of the spin noise method with the homodyne detection.

4.3 Conventional approach

Out analysis starts with a description of the optical scheme, a simplified version of which is depicted in Figure 4.1. It is similar to the one used in first published experiment on spin noise spectroscopy [4], and, therefore, one can name it a classical scheme. There are three elements, that define properties of the light, traveling along the z axis before the lens L1 comes into play:

A single-frequency single-mode ring-cavity-based Ti:Sapphire CW laser is a source of coherent monochromatic light with close-to-Gaussian spatial profile.

A single-mode polarization maintaining fiber purifies the light spatial mode to be $TEM00$.

The liquid crystal noise eater from BEOC serves to minimize possible low-frequency (up to 1 kHz) intensity fluctuations.

The resulting light is linearly polarized along y direction, further we refer to it as probe or E_0. L_1 and L_2 are anti-reflection coated achromatic doublets, serving for the focusing the light on a sample and the following collimation correspondingly. The initial focal distance for both is chosen to be $F = 100$ mm to match the Rayleigh length with the sample thickness. The light-matter interaction results in formation of secondary waves, we are interested in two groups: refracted with the same linear polarization as E_0 we name a transmitted beam, E_t, and scattered on spin density fluctuations with the orthogonal linear polarization we denote as scattered beam, E_s. Due to net optical activity, orthogonal modes E_t and E_s can experience a relative phase shift as well as a rotation in respect to

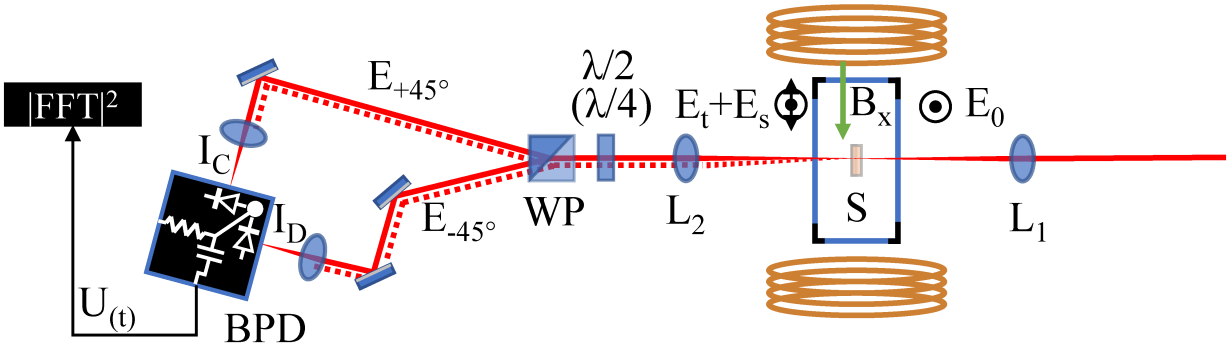

Figure 4.1. Schematic of the classical detection setup. The sample is placed in the probe arm where the spin noise is monitored in the transmission geometry by illuminating it with the probe beam in mode E_0 that is linearly polarized along the y axis. The transmitted and scattered light have orthogonal linear polarizations corresponding to the modes E_t and E_s, respectively. The half-wave plate ($\lambda/2$) and the Wollaston prism (WP) are used to convert these components into diagonally polarized ones, E_{+45° and E_{-45°. Detection results in the photocurrents I_C and I_D in the balanced photoreceiver, where $I^- = I_C - I_D$ is converted into the voltage signal $U(t)$, which is analyzed using a real-time Fourier transformed acquisition.

E_0. The latter is not depicted in the scheme for the simplicity.

A standard polarimetric part of the setup consists of lambda half, polarizing beam splitter and balanced photodiode, which is basically the analysis of the difference of intensities of two orthogonal polarizations. The good working point from the sensitivity perspective to analyze the small signal is when both arms do have the same mean power, for that before the polarizing beam splitter, which is in our case is a Wollaston prism (WP), we rotate the half-wave plate to set the polarization to 45° respective to the original y axis, in case of ellipticity measurements, half-wave plate is replaced with a quarter-wave one. The excess common mode intensity noise is suppressed via the balanced photodiode circuit: diodes are connected in series, and therefore the current flowing from or into the middle point is a difference of the currents of single diodes. It is converted to voltage with a transimpedance amplifier, roughly an operational amplifier, magnifying voltage on some resistor caused by the flow of a difference current via Ohms law. For current setup the reliable bandwidth is from 0.1 to 650 MHz (NewFocus 1607 balanced receiver with two Si photodiodes provided the noise-equivalent power of 40 $pW/\sqrt{Hz}$, and gain of 350 V/W is used). As the spectrum analyzer used on the end stage of signal processing has a minimum full scale of 50 mV, one need to amplify the voltage fluctuations on the output of the diodes, which is made by two low-noise voltage amplifiers, providing combined +20 dB gain. The details of the FPGA based spectrum analyzer we given in Ref. [16].

To measure exactly spin noise spectra, one needs to separate it from the all other noise sources. This separation is done by subtraction a power spectrum $P_2(\nu)$ at sufficiently high magnetic field (for example, $B_x = 100$ mT) from a power spectrum $P_1(\nu)$ at magnetic field of interest (for example, $B_x = 15$ mT), ν is a frequency. To be able to compare different spin noise spectra, we normalize the difference on the power of the photon shot noise $P_{psn} = P_2(\nu) - P_e(\nu)$, $P_e(\nu)$ stands for a sum of all electronic noises. The resulting power spectral density (PSD) formula is

$$\text{PSD (SN)} = \frac{P_1(\nu) - P_2(\nu)}{P_2(\nu) - P_e(\nu)}. \tag{4.1}$$

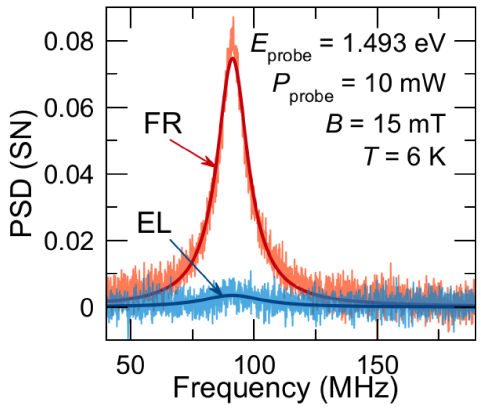

Figure 4.2. Faraday rotation noise (FR) and ellipticity (EL) measured with conventional setup in Figure 4.1.

Figure 4.2 shows typical values of what can be measured for FR and ellipticity. Ellipticity originates from that same residual absorption, which is a measure of perturbation of the system and the acceleration of the relaxation dynamics. Obviously, if you can see the system, the system sees you as well and such a measurement is not a nonperturbing, nor can be considered as one, and requires to go as low on the probe power as one can.

Measurements shown in Figure 4.2 have an analytical interpretation. Even though that the scattered wave E_s has a zero mean amplitude value, it can still give an observable contribution due to unavoidable interference with the transmitted beam. Through the calculations of beam splitter model, one get the difference current of the photodetector,

$$I_{\mathcal{F}}^{-} = \eta(E_t^* E_s + E_s^* E_t) \tag{4.2}$$

for Faraday rotation, and

$$I_{\mathcal{E}}^{-} = i\eta(E_t^* E_s - E_s^* E_t), \tag{4.3}$$

for the ellipticity, for both η is a diode spectral response (sensitivity).

Obviously, the interesting part is only E_s, the other one does not carry spin noise info, but can pick up charge fluctuations [85]. That is the reason why people detect them [49]. One can notice, that E_t can be therefore exchanged with any light field, given that the coherence with probe is preserved over the time span of signal accumulation.

4.4 Homodyne scheme

The scheme, which is called classical, is already a self-homodyne one. It means, that the interacted with the sample part of light interferes with the transmitted one to produce a measurable on the diodes radio frequency signal. Under reasonable circumstances, basically almost always, E_t is much more than E_s, $E_t \gg E_s$, then one sees that Equation 4.2 and Equation 4.3 are the real and imaginary Hermitian quadratures.They can be measured with a phase-sensitive detection scheme like for example, homodyne.

To implement that we use the setup as shown in Figure 4.3. Mach-Zehnder interferometer with sample in one arm followed by the HPE polarimetric scheme. In this case, the HWP is in front of Wollaston prism with extinction ratio of 10^4. To interfere the E_s and LO we use a nPBS 50:50. Worth noting, that exactly before hitting the nPBS, LO polarization is purified with Glan-Taylor (GT), and before that the wave front of LO is matched to E_s with a pair of achromatic doublets. To do that and to ensure the proper spatial overlap, the light mode E_t is used for the obtaining of the interference pattern and optimization its visibility, which is afterwards suppressed by rotation of the HWP, the output of the Mach-Zehnder is the input of the polarimetric part, the spin noise is readout by the same accumulation of the power spectrum as in the classical one.

The phase of the LO is stabilized to ensure the proper field quadrature of E_s, it is done by tuning the optical path length of the LO arm through the piezo driven mirror mount. The PID control is allowed by the leakage of the small part of E_t to the detection scheme either given by the finite extinction coefficient or the purposely tiny rotation of HWP and by the presence of the low-frequency monitor output of the difference output. As a controller for the loop a PID option of the HF2LI is used, its auxiliary input works just as ADC, and its general purpose output connected through the suitable voltage amplifier to the piezo. After the scan over the tuning range of piezo performed, one can choose the desired set point for the phase (Figure 4.3). As a consequence of the stabilized phase, the intensity on the eyes of the balanced photodetector is stable as well, reducing the low frequency drift of the accumulated power spectrum (Figure 4.4a). It is seen as low-frequency noise in one eyed homodyne scheme [12]. Balanced homodyne detection can be even made insensitive to LO quadrature phase noise[84, 76]. As one can see the originating from the field modulation negative peaks in the high frequency area can actually confuse: one would expect linear behavior and therefore, at 5 times the field, 5 times the frequency and 120 MHz*5 is 600 MHz, not 420 MHz. Additionally, negative peaks look asymmetric in comparison to the fitted Lorentzian. At this point one need to remember about aliasing and Kotelnikov-Nyquist-Shannon sampling theorem: by insufficient sampling (1 GS/s in this case), which means that incoming frequencies land not in first one, but in a higher Nyquist zone, these frequencies will be folded to

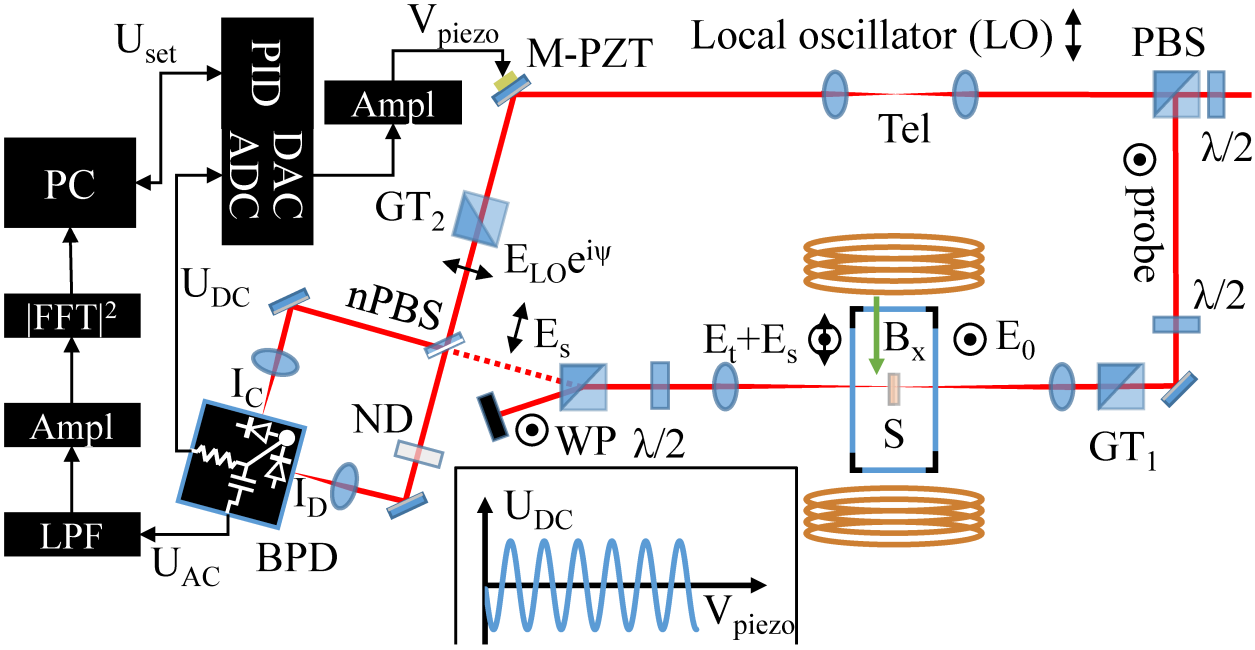

Figure 4.3. Schematic of the homodyne detection setup. The single-mode laser beam is split at the input of the Mach-Zehnder interferometer into the two interferometer arms by a polarizing beam splitter(PBS). The sample is placed in the probe arm where the spin noise is monitored in the transmission geometry by illuminating it with the probe beam in mode E_0 that is linearly polarized along the y axis. The transmitted and scattered light have orthogonal linear polarizations corresponding to the modes E_t and E_s, respectively. The half-wave plate ($\lambda/2$) and the Wollaston prism (WP) are used to filter out the electric-field mode E_t. The passed scattered light mode E_s and the mode of light in the reference arm of the interferometer (local oscillator) are sent to the input of the 50:50 non-polarizing beam splitter (nPBS). The interference of the electric field mode E_s and the local oscillator E_{LO} results in the photocurrents I_C and I_D in the balanced photoreceiver, where $I^- = I_C - I_D$ is converted into the voltage signal $U(t)$. Two components of $U(t)$ are analyzed: the AC component is analyzed using a real-time Fourier transformed acquisition similar to the traditional method, and the DC component is sent to the error input of the PID control loop used to adjust the voltage V_{piezo}. Thereby the relative optical phase shift between the two arms of the interferometer ψ is maintained by tuning the piezo-actuated mirror (M-PZT) to the set point U_{set}. The inset shows a scheme of the U_{DC} versus V_{piezo} dependence.

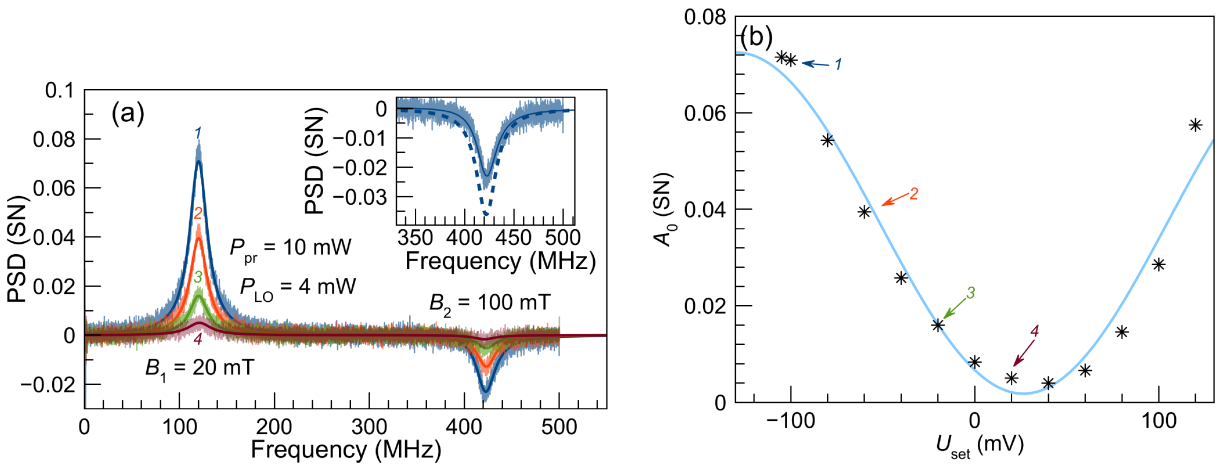

Figure 4.4. Measuring the spin noise using a balanced homodyne technique. (a) Spin noise spectra (noisy curves) and their Lorentzian fits (solid lines) measured in a linear combination of the E_s field quadratures by varying the phase ψ. A continuous evolution of the spin noise of Faraday rotation to the noise of ellipticity is obtained (curves 1–4). (b) The amplitude of the spin noise peak extracted from fitting. The arrows indicate the points where the curves presented in the panel are measured.

the first one without the possibility to distinguish them from low-frequency signal. As soon as we have installed only 600 MHz low-pass filter on the input of the FPGA, the peak is still seen, but is cut by exactly that filter, causing drop in the amplitude and asymmetry. Still, 500+500-420 MHz is 580 MHz and is not an expected 600 MHz, which leads us to the way we measure the magnetic field: we do not. We calibrated our coils, getting the A/T slope as a mean of back and forward scan, meaning, we do not take hysteresis of the cores of electromagnet into account. We do know, that the hysteresis is more pronounced, when we are around 0 mT, so the 100 mT field is more precise. 5.8 MHz/mT for the peak leads to conclusion that 120 MHz peak is actually corresponding to 20.7 mT, 0.7 mT being the difference when we go from 0 mT to 20 mT and from 100 mT to 20 mT. Still even the corrected amplitude is roughly two times less, than the low frequency peak amplitude. The reason for that is the bandwidth of the receiver himself, 650 MHz, meaning, that at this frequency the amplitude of the output is halved.

In Figure 4.4a one can see power spectra at different phase set points, which means different relative optical phases between LO E_{LO} and probe, be it E_t, E_s or E0. Obviously, the amplitude of the signal as well its integral power strongly depends on the phase (see Figure 4.4b). This can be as well explained theoretically: LO is $E_{\mathrm{LO}}e^{i\psi}$, ψ is the introduced controlled shift. as the absolute phase does not matter. then we take the nPBS and get the difference current:

$$I^{-}_{\mathrm{HD}} = K\eta E_{\mathrm{LO}}(E_s^* e^{i\xi} + E_s e^{-i\xi}), \tag{4.4}$$

where K is the spatial overlap and $\xi = \psi + \pi/2$. As one can see, at $\xi = 0$ is the Faraday, and $\xi = \pi/2$ is ellipticity, therefore there is no surprise to see in Figure 4.4a the match between curves 1 and 4 with measured classically under the same excitation conditions and diodes power.

All together, there following advantages of the homodyne vs classic: First, probe power can be reduced by corresponding increase of the LO power, leaving system in less perturbed state with

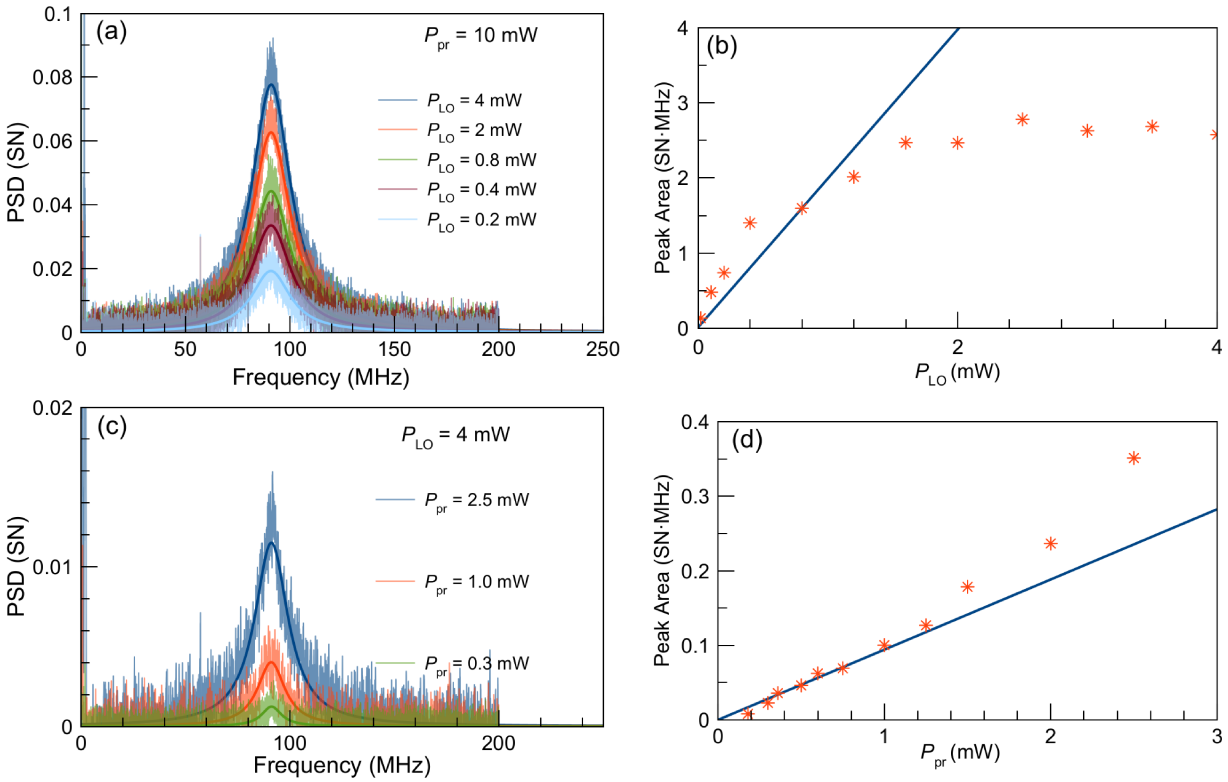

Figure 4.5. Analysis of the perturbation of the spin system using homodyne detection of spin noise. (a) Power spectral density of the Faraday rotation noise measured at fixed probe power using the homodyne technique at varying powers of the local oscillator. (b) Power dependence of the integrated spin noise power (red stars), a linear fit to its area is shown by the blue line. (c) Spin noise spectra measured at varying probe power and constant power of the local oscillator. (d) Area of the spin noise power (red stars) extracted from fitting. A linear fit of the curve is provided by the blue line.

comparable signal level. Second, the homodyne is not limited to the collinear component only, we can pick up different modes, even ones, that are outside of the mode of the transmitted beam. [29].Third, we can measure any quadrature in phase space without changing the setup.

4.5 Demonstration of improved efficiency

Essential distinction between the two described methods - classical and homodyne - is, that the normalization to the shot noise of the LO for the latter allows theoretically infinite increase of SNR. In the practice, it is limited by several reasons, originating from nonlinear behavior. Let us have a look on the measured data of the signal amplitude versus the intensity of LO (Figure 4.5a). First of all, we see that power spectra may be easily tuned by change of the LO power. At the same time predicted due to Equation 4.4 linear dependence saturates around 2 mW on photodetector, which coincides with expected value for saturation of the integrated amplifier. Obviously, dependence eta of $\eta(E_{\mathrm{LO}})$ may not be omitted. Such a measurement of P_{LO} dependence is therefore a

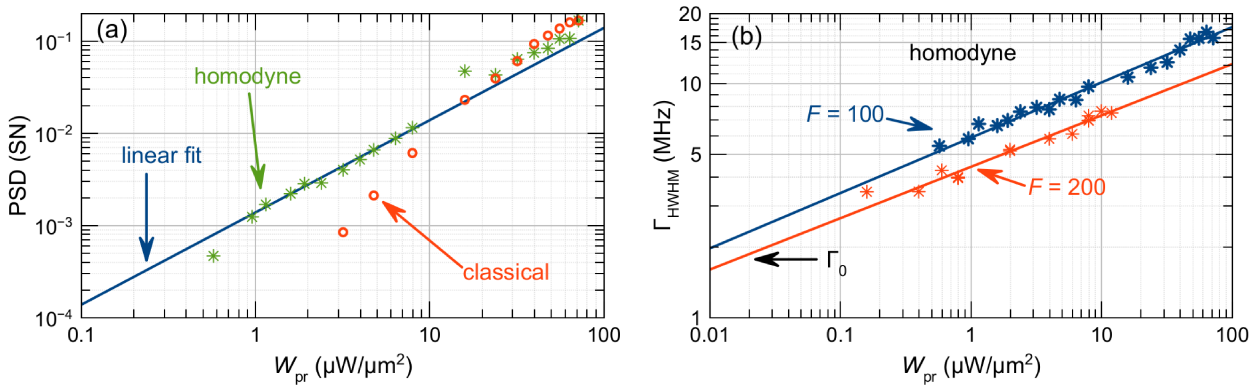

Figure 4.6. (a) Amplitudes of the spin noise PSD peaks versus probe power density measured in the conventional detection scheme (red circles) and with the homodyne detection (green stars). A linear fit is given by the blue line. (b) Electron-spin relaxation rate versus probe excitation power density, extracted from fitting the PSD curves measured with $F = 100$ mm (blue stars) and $F = 200$ mm (red stars) lenses in the probing arm. Lines are fits using a power function: $\Gamma_{\mathrm{HWHM}} \propto W_{\mathrm{probe}}^{0.22}$. The value of the spin relaxation rate in darkness (Γ_0) is indicated.

characterization of photodetector nonlinear behavior. Secondarily, spin system itself possess nonlinearities,expressed in the deviation of the PSD area from strait line when plotted against probe power see Figure 4.5d. Measured data tell us that system becomes noisier by additional carriers. This leads to the peak broadening Γ_{HWHM} as well, which is shown here, in Figure 4.6b, and corresponds to elevation in the relaxation rate of spins. Remember, that we define the diode power solely by the LO intensity, which is kept constant at 4 mW. Transmitted light filtered out by the Glan-Taylor polarizer, leaving only the scattered component to be analyzed, whose power is negligible in comparison to the LO intensity.

To deduce the dependence of the perturbation of the system on the power of the probe beam, a comparative series has been done in both evaluated methods - classical and homodyne ones - in Figure 4.6a. As a more reliable parameter, power density is taken for the x- axis and peak amplitudes are the y-axes correspondingly, both in logarithmic scale. One sees no statistically significant difference between both in the area 10 to 100 μW/μm^2 ($P_{\mathrm{pr}} > 1$ mW). Situation changes drastically as soon as we go below 10 μW/μm^2: the classical one becomes so ineffective, that we could not wait long enough to see any signs of peak presence - electronic noise dominates over all other noise sources, be it spin or photon shot noise.

On the contrary, in the homodyne with the help of LO beam the photon shot noise is kept at a desired level (sufficiently above the electronic noise) the whole time. Which allows even a very subtle signs of spin noise to be collected and processed, following the linear relation, as Equation 4.4 predicts. Nevertheless, the lower the power (density) - the lesser the amplitude and the greater time one needs to wait for the signal to be distinguishable from the background, one hour of accumulation was set as a limit for one measurement, therefore under the 1 μW/μm^2 only a couple of data points was obtained.

An essential part is to estimate at the perturbation of the spin system in the soft excitation regime, that can be done by the calculation of the relaxation time. For that purpose a set of measurements

was carried out with two lenses with distinct focal lengths in the incoming to the sample beam path. To be precise, diameter of the laser light waist was directly measured with a beam profiler, which turned out to be $20\,\mu\text{m}$ and $40\,\mu\text{m}$ for $F = 100\,\text{mm}$ and $F = 200\,\text{mm}$, respectively. By increasing the focus twice, we increase the area by four, dropping by the same amount the power density, resulting in almost a half of an order of magnitude less. Additionally, transit-time broadening decreases with a gain of illuminated area, an estimated length was got in Ref. [17]. and is on the scale of $10\,\mu\text{m}$ in used sample. Figure 4.6b shows the outcome of the measurements. A trend of decline of Γ_{HWHM} adheres to the exponent function with 0.22 coefficient. One can get $\tau_s = (2\pi\Gamma_{\text{HWHM}})^{-1}$ as low as $52\,\text{ns}$ at the minimum achieved power density, that is in the range of measured by the other method (Hanle) in [17]. On the contrary, on the extended pump-probe setup [9, 8] one gets for the relaxation time a value of $(2\pi\Gamma_0)^{-1} = 90\,\text{ns}$, using the same sample and excitation densities. A significant difference is the use of pulsed laser and effective darkness during the evolution of the system between the pump and probe pulses. One would find fits of the experimental points in Figure 4.6b remarkably, the extrapolation gets to the expected value at a power density one order of magnitude less, than we can achieve now.

4.6 Discussion

Control over the optical phase allows obtaining the complete quadratures picture of spin noise without any modification of the optical setup. That is of a great importance, when one coerced to use resonant excitation, this happens in atomic-like systems, for example, in QDs, where the signal is present exactly there, where the inhomogeneously broadened absorption line is located.

As dictated by the nature of interference, after mixing on the beam splitter, single photons tend to group and exit either one port or the other one, Hong–Ou–Mandel effect. We do have the coherent state, instead of the Fock ones, we are not limited to only this state, the problem is, either in balanced or single-eyed version is that SNS obtained as a difference spectra between two states, and the background noise should stay the same for the reliable measurement. Unstabilized by phase interference will slowly drift, causing changes in the photon shot noise, seen by the detector and will render measurements useless. Introduction of PID loop for phase stabilization saved us from that problem, reducing the excess noise below $50\,\text{MHz}$ and allowing one to get to reliable long time accumulations, which leads to low probe power measurements and approaching the intrinsic relaxation times in the results. A well studied sample of n-doped bulk GaAs shows the limitation of that time by the tails of the absorption, meaning that the intrinsic time can still differ from the obtained in the SNS and be higher than that.

It is worth mentioning, that there is a room for improvements regarding the sensitivity of the setup, likewise by collecting and processing other scattering modes, present in 0D systems, such a system is QDs, where the element size is much smaller in comparison to the wavelength of the incoming optical radiation. [29, 12]. With that in mind, the proper choice of the LO mode would allow picking signal modes, propagating not collinear to the transmitted of the reflected beams. In this part of work, no any SN signal is seen out of the aperture of the forward scattered field.

Unfortunately, the required bandwidth is big enough to make the amplification of the diodes and, therefore, signal-to-noise ratio on order of $+10\,\text{dB}$ at maximum power on the diodes. This would be enough, if it would not be directly connected with the power, falling on the sample,

which naturally leads one to the idea of interfering the scattered light with light from the same laser, which does not go through the sample, local oscillator. The experimental measurements were done in following manner: the setup in interchangeable configuration between classical and homodyne, sample is n-doped bulk GaAs, the detection bandwidth maximal, 1 GHz, temperature controlled with supplied controller MercuryiTC and kept on the level of 6 K, Wavelength chosen on the edge of the luminescence spectra, internal locking scheme. For the convenience magnetic field was chosen to be 15 mT to produce Larmor peak well distanced from 0 Hz and not too high in order not to loose sensitivity due to diode response function and broadening of the peak. First, the power dependencies for the classical scheme were measured. One can clearly see the point, where the dominance of electronic noises restrict the signal acquisition. Second, and the longest part was to match the dependence for the homodyne scheme with the same powers on the diode and on the probe. At first even after scanning all the phase set points, one could get only half of the signal of that in classical scheme, the most probable reason for that was some phase averaging: there was a vacuum leak in the cryostat, causing possible thin film deposition on the sample, the piezo actuator was mounted to the whole translation stage, reducing the locking bandwidth to roughly 1 Hz or even lower, in first attempts in local oscillator beam no phase front distortion compensation was present as well as no additional purification of polarization prior to interference with signal beam on the nPBS. Resolving these issues allowed us to experimentally match the results of both methods, to show the possibility of quadrature measurements just by phase scan of the interferometer, and to get to lower power densities on the sample.

4.7 Summary

In this part of work, a polarization sensitive interferometry performed for obtaining both Faraday rotation and ellipticity. The spin noise of n-doped GaAs was measured in different quadratures by variation of the path difference in the arms of the Mach-Zehnder interferometer. Regimes of perturbation of the spin system are analyzed by measuring the electron spin relaxation time at excitation powers varied over several orders of magnitude while probing in the transparency region of GaAs. The quantitative analysis shows that for all reasonable intensities of the probe we find an amplification of the sensitivity of the homodyne detection scheme over the one of a conventional 45 degrees polarimetric setup. The obtained signal to noise ratio is found to be always larger in the former scheme and is limited only by the finite dynamic range of the photoreceiver. These findings might be used to implement weak measurements of spin dynamics on the nanoscale.

Most results in this chapter are published in Ref [67].

5 Proof of the scattered nature of the spin noise signal

In this chapter we apply the developed in chapter 4 homodyne technique to prove the formation mechanism of SNS. It was already pointed out by theoreticians a long time ago [29] that there are similarities between SNS and Raman scattering, and it was further analyzed theoretically[28, 46, 44, 47, 45, 48] with no any experimental proof. As of now, the only couple of articles, that address measurements of scattered light is [12, 14], but still neither of them detect the scattered light outside of the aperture of the reflected or transmitted light. For a solid proof of scattered nature of SN we study n-doped QDs in DBR structure.

5.1 Reminder on homodyne detection and sensitivity

As can be seen from the previous chapter 4 or the above-mentioned theorists, SNS depends quadratically on the probe intensity. Enhanced SNR at elevated probing intensities comes at a cost of a higher system disturbance, which is generally undesirable [18, 25].

To reduce the power and preserve SNR one can think of adoption of optical resonator(s), be it macro- or micro-resonator(s), the latter option advised in some works [88, 69, 19] as an efficient way of boosting the signal. One problem is that enlarged light-matter interaction compensates the reduced power and effectively the perturbation stays the same. The other problem is the high-speed balanced photodetector, which has high dark electronic noise, and therefore, cannot properly operate at such low light intensities.

The logical solution is to mix a weak signal with a strong reference and send it to the detection scheme. The described method is a homodyne detection [12, 82, 67].

5.2 Setup modification

The naive way to describe the spin noise signal generation is to assign it to the Faraday rotation on fluctuations of the magnetization. Actually, the Faraday-rotation-based detection can be explained either as the spin-flip Raman effect[29, 28] or as a light scattering in the medium with fluctuating gyrotropy[44], both versions being equally reliable and both rely on scattering.

From these points of view even the classical scheme is a self-homodyne one: the transmitted light interferes with the scattered field. So if we want to proof the scattered nature of the spin noise signal formation, there are two steps to be done. First of all, we substitute the transmitted light with the coherent light, whose path omits the sample. This part is just an implementation of the homodyne detection, which was done previously in chapter 4. Secondly, we need to excite the

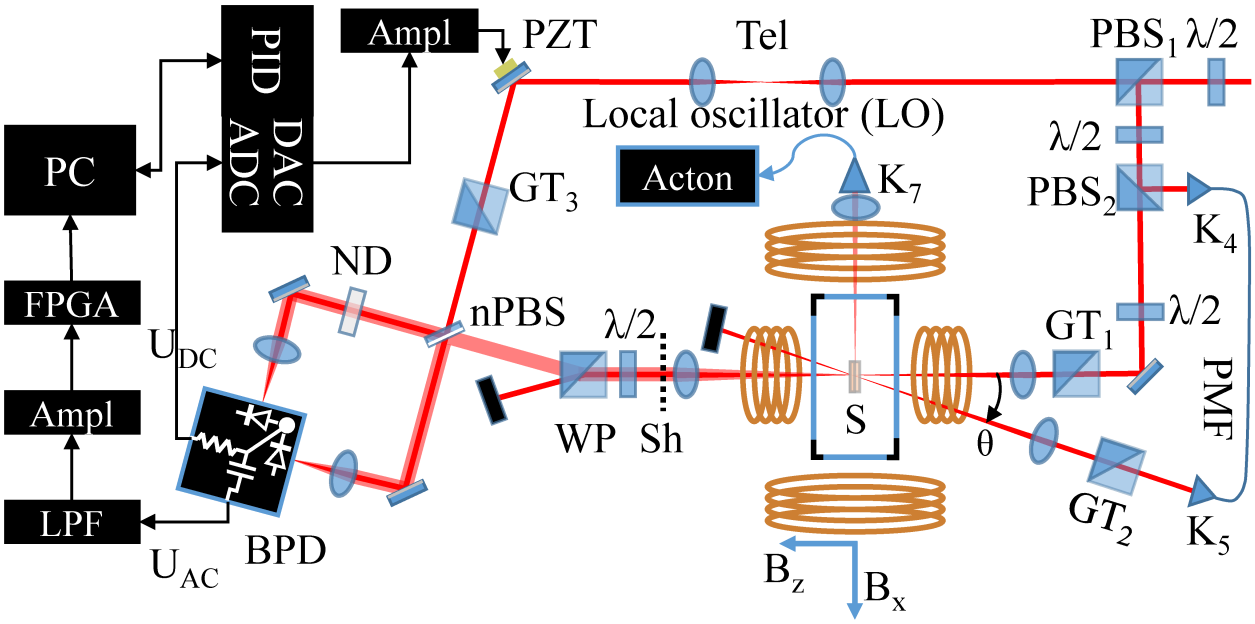

Figure 5.1. A homodyne detection scheme with side illumination is shown. As previously described, the main laser beam is divided into a Local Oscillator (LO) and a probe beam. The probe beam is then further divided into two beams: one that impacts the sample (S) normally, which we will continue to refer to as the probe, and an auxiliary (AUX) beam, which is directed at the same spot under an angle θ. Given the low intensity of scattered light, we employ a shutter (Sh) for the AUX reference measurements to eliminate all backgrounds not related to Spin Noise (SN). A half-wave plate ($\lambda/2$) and a Wollaston prism (WP) are used to select and spatially separate the polarizations of interest - the orthogonal one for Spin Noise Spectroscopy (SNS) signals and the same for adjustment purposes. The interference of electric fields, scattered by the sample light, and the Local Oscillator (LO) occurs at the 50:50 non-polarizing beam splitter (nPBS) and is measured at the photodiodes of the balanced receiver (BPD). The current difference is converted into the voltage signal $U(t)$. The *ac*-component of $U(t)(U_{\mathrm{AC}})$ has a 3 dB bandwidth ranging from 40 kHz to 650 MHz, and it goes through a low-pass filter (LPF) and an amplifier to the Field-Programmable Gate Array (FPGA) for calculation and accumulation of the spin noise power spectrum. The *dc*-component, with a 3 dB bandwidth from DC–15 kHz, is used for the piezo control in a PID loop. The relative optical phase is maintained by adjusting the piezo-actuated mirror to stabilize U_{DC} around the set point U_{SP}

scattered light so, that the stimulating beam is not going to the detection scheme at all, and only the scattered field is present.

To achieve the second requirement, we modify the scheme of the spin noise experiment with homodyne detection, see Figure 5.1, it is used for both characterization of samples and SNS measurements. This setup builds on the main part of the Mach-Zehnder interferometer described in [67] and introduces some crucial modifications. The key changes are:

- The probe beam is split into probe and auxiliary (AUX) beams. The latter is redirected

towards the goniometer arm for side illumination.

- The detection channel utilizes a Wollaston prism in place of a Glan-Thompson prism, as well as a wedged plate non-polarizing beam splitter (nPBS) rather than a cubic one. This approach reduces back reflections and mitigates arising parasite signals.

- It incorporates the capability to collect photoluminescence (PL) from the side of the sample.

In the modified setup, the vertically polarized AUX beam impacts the sample (S) at an angle θ relative to the normal incidence. Focusing and collimating lenses of $200\,\mathrm{mm}$ (spot diameter: $40\,\mu\mathrm{m}$) and $60\,\mathrm{mm}$ focal length, respectively, are employed.

To filter out the transmitted light component, which is orthogonally polarized to the scattered light [28], we use a half-wave plate ($\lambda/2$) and a Wollaston prism (GT). We collect the fraction of scattered light within the solid angle covered by the numerical aperture $\mathrm{NA} = 0.07$ of the collimating lens. This light is directed to the input of a 50:50 nPBS, together with the LO, which is sent through the second arm of the interferometer.

The interference of these two horizontally polarized linear fields results in photocurrents in a balanced photoreceiver with a $650\,\mathrm{MHz}$ bandwidth. The difference in their currents is converted into the voltage signal $U(t)$, the AC component of which is digitized using a $2\,\mathrm{GS/s}$ analog-to-digital converter and Fourier transformed using an FPGA-based real-time fast Fourier algorithm [16]. The DC component of $U(t)$ is routed to the error input of a proportional-integral-derivative (PID) control loop used to adjust the piezo voltage [67]. Hence, the relative optical phase between the two arms of the interferometer is maintained by tuning the piezo-actuated mirror (PZT) to the set point U_{SP}.

5.3 The Sample

In this part of the work, the capabilities of the homodyne version of the detection are studied further, as well as the physical characteristics of the spin noise signal. It could not happen without the proper sample, manufactured by our colleagues form Bochum. Prior to the growth, the geometry of the desired structure was numerically simulated and optimized for the transmission configuration of the measurement.

The $5\lambda/2$ cavity (λ is the design wavelength) enclosed in 14 bottom and 11 top pairs of AlAs/GaAs layers was grown on the GaAs substrate. There are 4 InGaAs QDs layers, each with a density of $10^{10}\,\mathrm{cm}^{-2}$ and positioned at antinode of the electric field, see the inset of Figure 5.2. Delta layers of Si mediate n-doping for the QDs. To minimize an unwanted absorption, these layers are deposited in the nodes of the field: there are two dopant layers for each layer of QDs, both exactly at a distance of $64.5\,\mathrm{nm}$ from the latter.

Created by Stranski–Krastanov mechanism, QDs experience very strong dispersion of size, the latter is connected to their optical transition energy via quantum confinement. In order to tune the QDs luminescence peak to the cavity transmission, a method called rapid thermal annealing (RTA) is applied. RTA - a short warm up to several hundreds degrees Celsius - manipulates concentration of indium, due to its small boiling temperature. The diffusion of the indium outwards of the QDs causes the drop in the stoichiometry ratio and, consequently, the rise of the band gap energy.

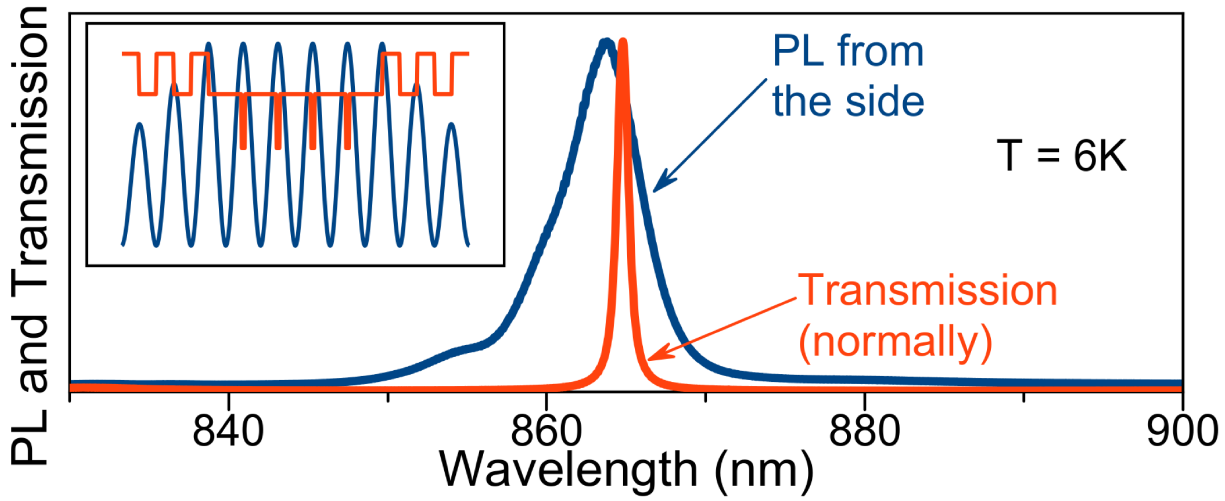

Figure 5.2. QDs PL measured along the cavity plane for 785 nm excitation (blue line) and cavity transmission (red line) measured for white light excitation. Inset is sketch of the $5\lambda/2$ cavity showing the electric field distribution (blue line) and 4 QD layers placed at the field antinodes seen as reduced potential levels. The red line gives the potential of the DBR structure with QDs.

Temperatures for RTA are high enough to activate migration of other atoms (Ga,As) too. This redistribution of material reduces size variation of quantum dots, narrowing their emission spectra.

A set of samples from one growth process was annealed at different temperatures. To access the unmodified by the distributed Bragg reflector (DBR) structure of the QDs, a photoluminescence (PL) was collected from the side of the sample (in the plane of DBR). The 785 nm excitation laser light was directed at a normal incidence. Figure 5.2 demonstrates the sample annealed at 900 °C, as it has the best overlap of white light cavity transmission (red line) and the QDs PL spectrum (blue line) at 6 K.

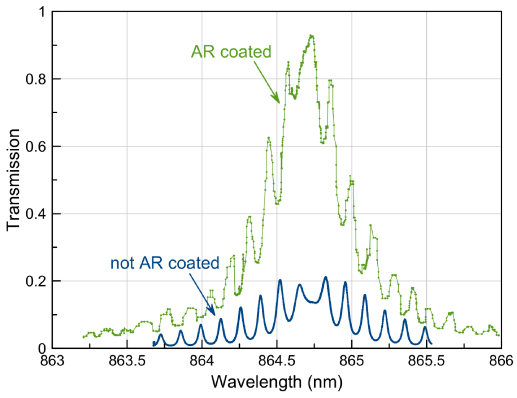

Figure 5.3. Comparison of cavity laser transmission spectra with (green) and without (blue) anti-reflection coating(AR).

First laser transmission spectra showed strong modulation, not seen in the white light, therefore, connected to the coherence. The etalon effect suits the angular behavior: decrease with the increasing angle due to lesser overlap of interfering reflexes. The optimized for the transmission structure should have had neglected the effect, effectively removing one of the substrate borders. It seems though, that the reflection occurs exactly in the substrate, while the thickness of the whole grown layer is less than 4.4 μm. To evade the etalon effect, the back side of the sample needed to be covered with anti-reflection coating, designed for the cavity resonant frequency (864.831 nm). The single layer thickness (d) was calculated as d=$\lambda/(4n_1)$, n_1 is the refraction index of coating material. Optimal coupling is achieved

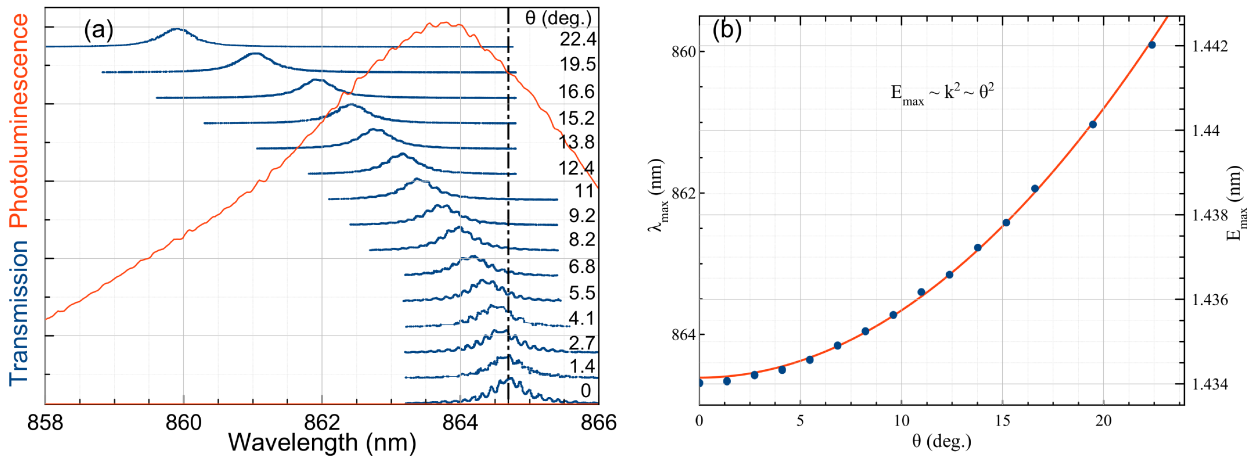

Figure 5.4. (a) Waterfall of DBR microcavity transmission spectra (blue) shifted vertically based on the angle of incidence, transmission measured by laser wavelength scan. At normal incidence θ = 0° the wavelength of the transmission maximum is λ_{max}=864.69 nm, it is denoted by the black dash-dotted line. The photoluminescence spectrum of QD emission (red) is measured from side (θ = 90°) to avoid spectral selection caused by DBR. (b) Transmission peak maximum position (blue dots) (λ_{max}) as a function of angle θ and its parabolic it, red line.

when $n_1 = \sqrt{n_0 * n_2}$, where $n_0 = 1$ refraction in air/vacuum and $n_2 = 3.6$ for GaAs at 5 K. HfO_2 has refraction index n=1.89 and matches the $n_1 = \sqrt{3.6} = 1.9$ perfectly. The 114.2 nm of HfO_2 were successfully deposited, the change in laser transmission spectra is shown in Figure 5.3. Note that the interference peaks did fall in the amplitude, but the whole transmission of the sample reached almost 95 percent.

To get a better understanding of upcoming angular dependencies, the effect of the DBR structure on the transmitted light intensity is studied as a function of the wave vector value (incidence). To measure the transmission spectra, the laser is scanned over the transparency window at each fixed angle. To enhance the SNR a lock-in amplification of the detector is used, a modulation comes from a mechanical chopper, that is placed in the probe beam path before coupler to the AUX. The behavior in the angle dependence fits perfectly the theoretically predicted parabolic behavior of the maximum transmission energy in Figure 5.4b.

5.4 Basic electron spin properties from the outside of the aperture

To get to the intrinsic electron spin relaxation time τ_s, the dependence of the Larmor peak parameters on the probe power is extracted, see Figure 5.7 (a) and Figure 5.7 (b), the parameters being $\lambda = 864.69$ nm, $B = 50$ mT and $T = 5$ K. Figure 5.7 (b) contains a log-log graph, showing the saturation of the amplitude of the peak at probing excitation exceeding 4 mW. With the help of fitting the data in Figure 5.7, one can get the expected value of Γ_{HWHM} at zero power, namely $\Gamma_0 = 54$ MHz, which can be recalculated to $\tau_s = 2.9$ ns. The very important point is the use of n-doped QDs, which in contrast to p-doped QDs (as shown in [26]) do not experience strong broadening of the

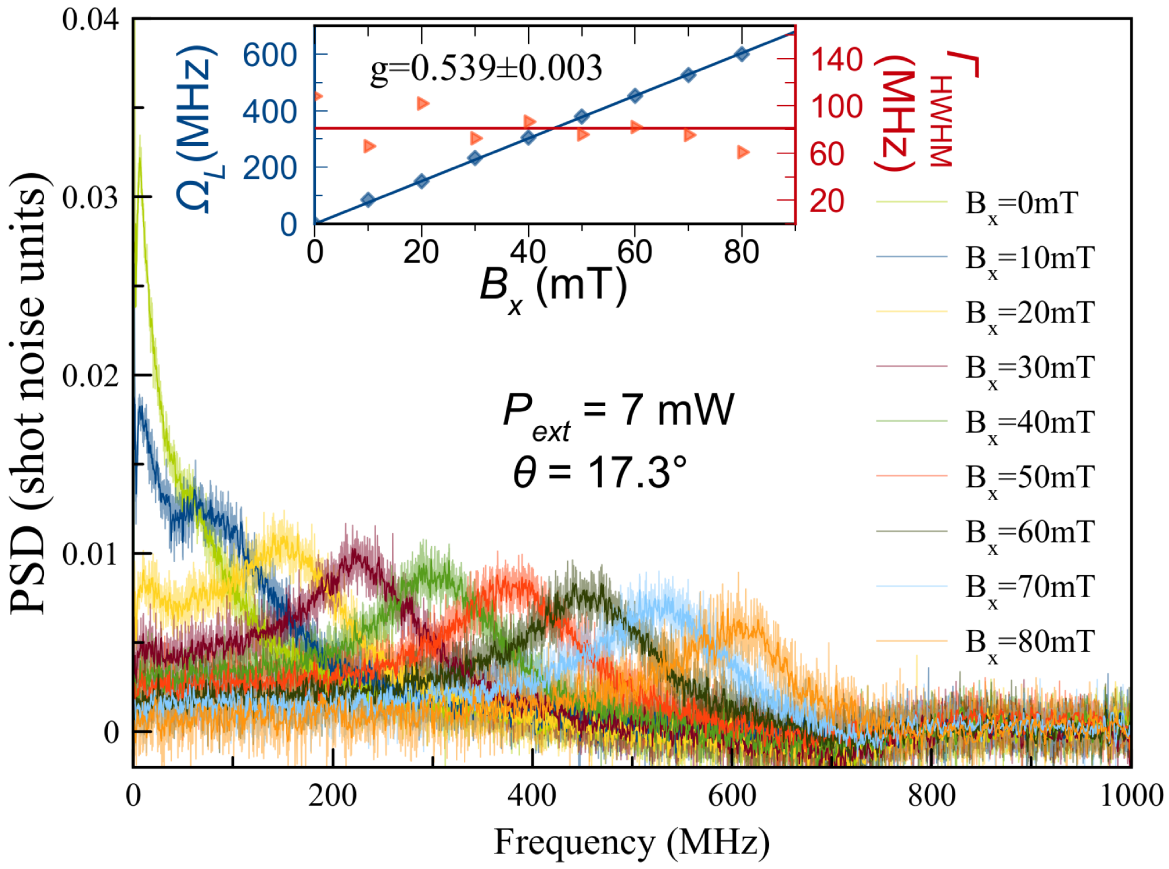

Figure 5.5. A series of SNS spectra as a function of external transversal magnetic field, when only the AUX beam is used and probe is blocked before it reaches the sample. On the inset one sees the peak position and width as a function of the above mentioned field. $\lambda = 864.69\,\mathrm{nm}$

SNS peak with the application of the magnetic field due to spread in the g-factors, Δg at least for some small fields, being locked to the fluctuating nuclear fields in the electron surrounding. ΔB_N [16, 53, 26] as $\Gamma_0 = (2\pi\tau_s)^{-1} = (2\pi\hbar)^{-1}\sqrt{(\Delta g \mu_B B)^2 + (g\mu_B \Delta B_N)^2}$. Here, the μ_B is the Bohr magneton and $\hbar$ is the reduced Planck constant. Peak width stays unaffected by the field in the used range, therefore, one allowed to assume $\Delta g = 0$, and get the $\Delta B_N = \hbar/(\tau_s g \mu_B) = 7.3\,\mathrm{mT}$, which corresponds to the quantity, obtained for the QDs without the DBR cavity in Ref. [26]. Worth noting that for a reasonably weak perturbation by probing during measurements, one had to lower the probe power by two orders of magnitude in QDs in DBR in comparison to just QDs. In such circumstances, the detection in homodyne scheme stays the only option, in order to stay in regime of shot-noise limited photodetection [82, 67].

One can see the case of measuring the spin noise magnetic field dependence series, using only the auxiliary beam to create the scattered light in Figure 5.5. $\theta = 17.3°$ ensures, that transmitted beam will not get into the detection scheme - it misses even the aperture of the collimating lens. $\lambda = 864.69\,\mathrm{nm}$ is the wavelength of normal transmission of the cavity, meaning, that the scattered

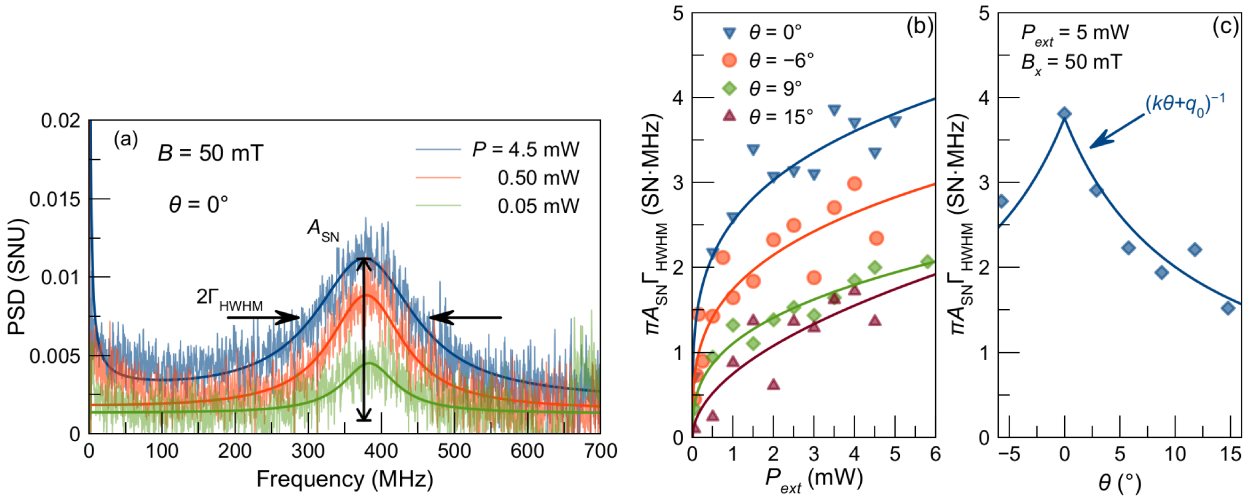

Figure 5.6. (a) Demonstration of a good peak separation at 50 mT for a calculation of a SN peak total power via its amplitude and width. (b,c) SN peak total power as a function of the AUX power and incidence angle. Experimental conditions: $T = 6\,K$, and $\lambda = 864.69$ nm.

light will also escape the cavity along its normal in the most effective way, for which configuration the homodyne part of the detection is aligned.

As one can clearly see for the small magnetic fields, spin noise signal does show up as two peaks - one centered at zero frequency and the other one, Larmor, moving with the magnetic field [16, 26]. Now we focus on the Larmor peak only, and pick up the essential parameters of the studied sample shown in Figure 5.6a. From the peak position one obtains g-factor $|g_e| = 0.54$, similar to the QDs investigated in Ref. [16], blue rhombuses in inset of Figure 5.5. Peak width Γ_{HWHM} is connected to the relaxation rate and a lifetime of a spin, $T_s = 1/(2\pi\Gamma_{\mathrm{HWHM}})$, where $1/T_s = 1/\tau_s + 1/\tau$. τ_s is the spin relaxation time and $\tau = n_0/G$ is the recombination time, which depends on the carrier concentration, n_0, and the generation rate of carriers, G [21, 81]. In the range of magnetic fields where the peak position appears at frequencies below 1 GHz, the Larmor peak width stays constant at $\Gamma_{\mathrm{HWHM}} = 81$ MHz corresponding to $T_s = 1.96$ ns, as shown by the red triangles in the inset of Figure 5.5.

This result uniquely shows the observation of spin noise outside the aperture of the transmitted probe, confirming the theoretical results of Refs. [29, 44], and supports a recent report in Ref. [14].

Results from the attempt to extract trends for the number of probed spins, which is proportional to the area under the peak, are shown in Figure 5.6b,c: there is a notable knick point for the power dependence at 1 mW, meaning, that most of the spins are already participating. The decrease in the number of probed spins with the increase of the angle can be mostly subscribed to the geometrical overlap of illumination with the detected volume.

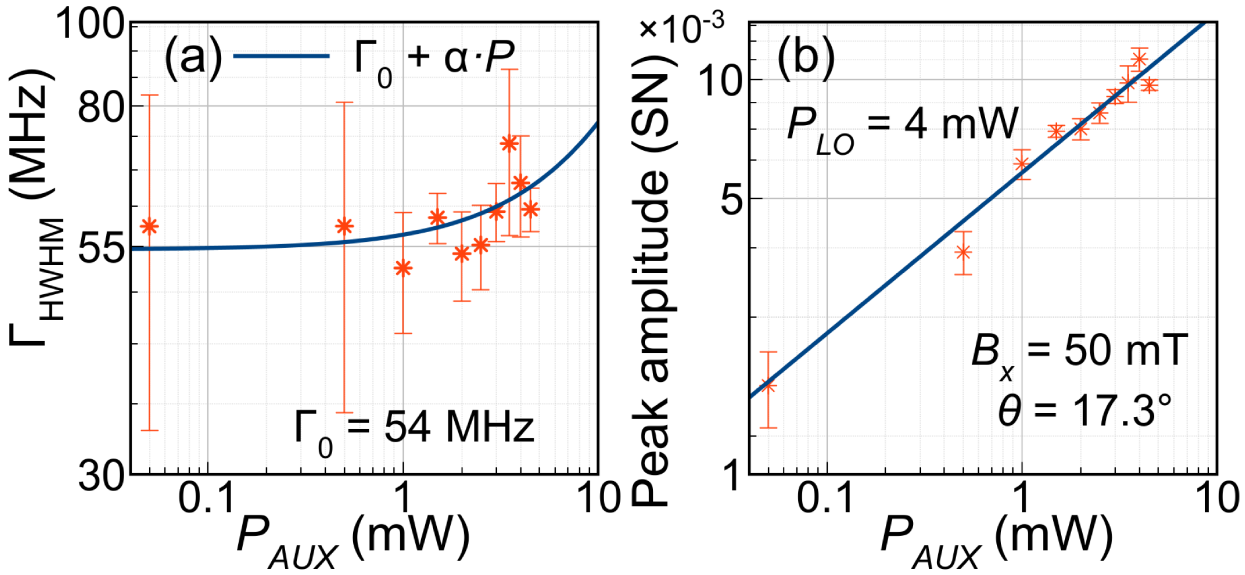

Figure 5.7. Experimental dependencies (red stars) of the Larmor peak width (a) and amplitude (b) on AUX power as well as their linear fits are depicted in log-log plots. According to the fit, peak width (a) has a zero-power limit of $\Gamma_0 = 54\,\mathrm{MHz}$. Spin noise amplitude (b) follows its linear fit in the whole measured range. Experimental conditions are: $T = 6\,K$, $\theta = 17.3°$, $B_x = 50\,mT$,$\lambda = 864.69\,\mathrm{nm}$ and $P_{\mathrm{LO}} = 4\,\mathrm{mW}$.

5.5 Scattering distribution and possibilities of signal amplification

One of prime interests is to amplify the signal by all accessible means. The simplest way is to increase illumination by increasing the probe power, but the saturation limits it quite fast. A bit more cumbersome path is to add another beam, which can potentially address other scatters, which are out of saturation, and therefore, amplify the scattered light intensity, given that the additional light is coherent and resonant with the first one, as discussed in Ref. [44].

As an implementation, we split a part of the probe radiation and directed it to the sample from the side at an angle $\theta = 17.4°$ to the normal one, being $\theta = 0°$. The polarization of both beams was kept vertical and additionally purified by GT prior to focusing on the sample. Figure 5.9 shows the outcome of these measurements. The brown rhombus represent the amplitude of SN peak at $B_x = 50\,\mathrm{mT}$ obtained for the different relative phase points between probe and LO, aux beam blocked[67]. The green cross at zero phase is the result of a experiment with only the aux beam, as no phase stabilization between him and LO was implemented, probe blocked. Blue squares are the mathematical sum of these two described measurement series. Such dependence would be the best case scenario for the amplification, when both beams are present [44].

The actual measurement is presented by red dots, revealing a non-trivial dependence of the auxiliary amplification on the relative phase between probe and LO. At $90°$ phase difference the resonant side illumination seems not to give any contribution to the detected scattered light (brown and red overlap), at the same time at $-90°$ it is close to direct sum. That is a clear evidence of

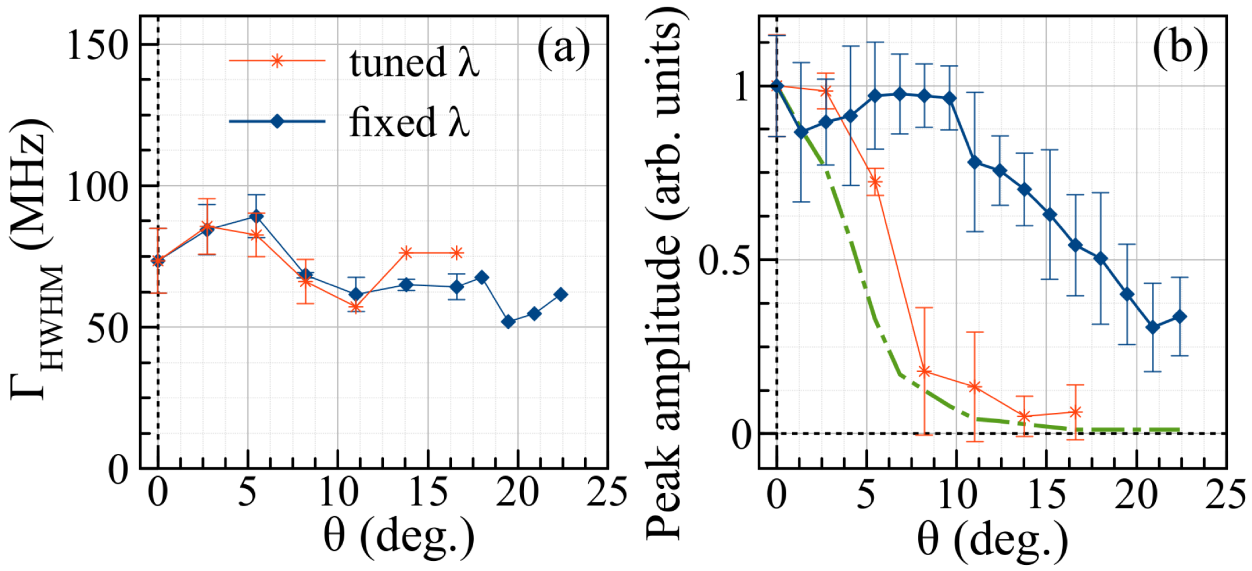

Figure 5.8. (a) Spin-noise Larmor peak widths at $B_x = 50$ mT as function of θ for two measurement modes: blue rhombuses for probe wavelength fixed at $\lambda_{\max}(\theta = 0°) = 864.69$ nm and red stars for probe wavelength tuned to $\lambda_{\max}$ for the current angle, see Figure 5.4a. Lines are guides to the eye. Error bars are calculated by averaging over three independent measurements. (b) Normalized amplitude of corresponding peaks as function of probe incidence angle θ. Green dash-dotted line corresponds to transmission intensity at fixed $\lambda = 864.69$ nm, as marked in the Figure 5.4b. Experimental conditions are: $T = 6\,K$, $P_{pr/AUX} = 2.3$ mW and $P_{\mathrm{LO}} = 4$ mW.

possibility to increase the scattering intensity with an auxiliary beam, still coming with its own dependence on the relative phase to the probe and LO beams. As discussed in Ref. [39] there are two kinds of scattered photons - they are either coherent or not. The first ones do have the same spectral properties as the laser radiation, which allows them to interfere with whichever beam of the laser (probe, aux, LO). The fact of phase dependence of the scattered light on the probe-aux phase, leads to conclusion, that the scattering on the QDs is indeed coherent. Important point is that to see any rise in scattering, total excitation caused by the probing beams -probe and aux - must be in the non-saturated regime of QDs transitions. Whichever beam has a higher power, it will dominate the effect and no visible amplification will be observed. That is a proof of low power scenario and a weak system perturbation (photons are in Heitler scattering regime) [63, 59, 74].

To measure the spatial distribution of the spin noise, the probe beam path was removed, and the auxiliary beam placed on the goniometer arm through the fiber to be able to smoothly change the incidence angle without the cumbersome realignment procedures. The collimation part after the sample is adjusted when the goniometer stays at 0 deg, ensuring, that the normally scattered light will interfere on the nPBS with the LO so, that the first Fresnel zone is in the center of the beam, going to the detector.

In Ref. [44] the course of interest was the diffusion of the carriers, which reduces the signal for larger wave vector values, which is proportional to the angle θ in our setup. That is the other reason to pick up a strongly localized electron system, being n-doped QDs, to be precise, n-doped (In,Ga)As/GaAs QDs, grown by our colleagues from Bochum on their MBE setup. As for the

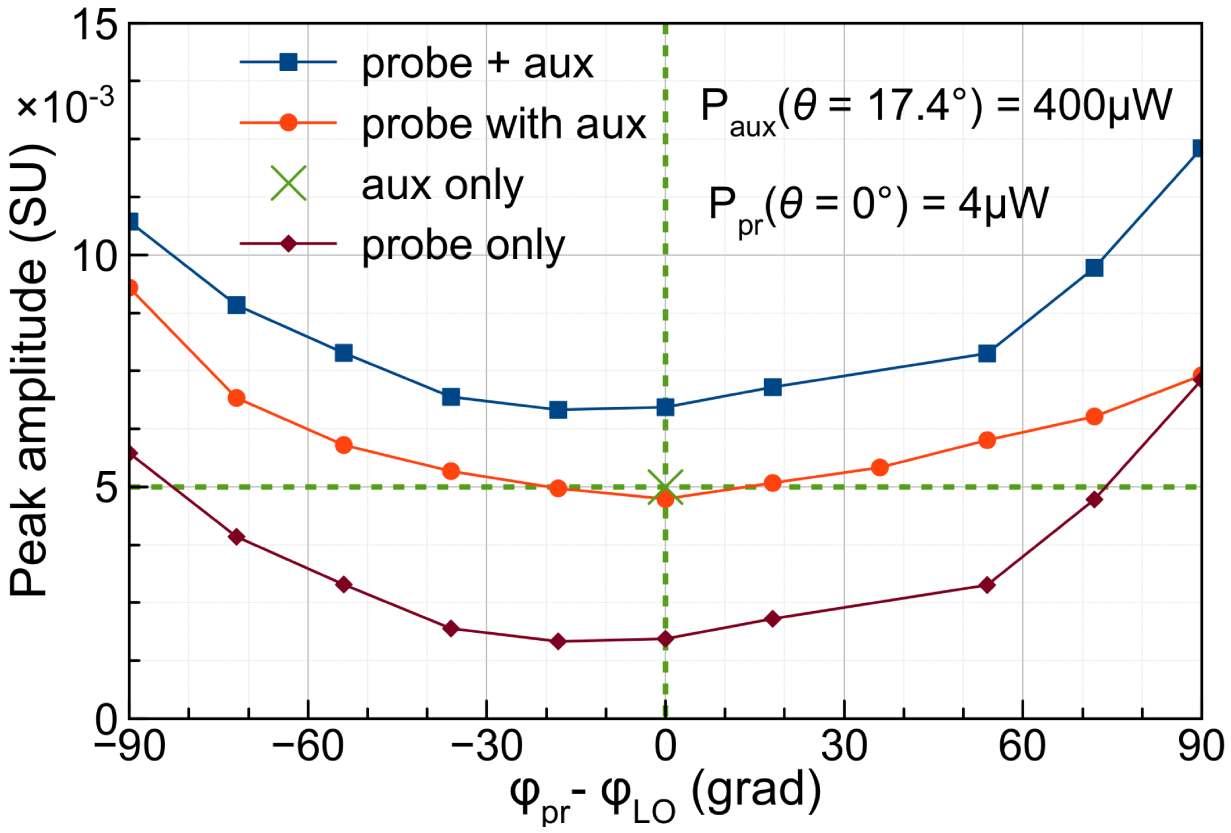

Figure 5.9. Amplitude of spin noise Larmor peak at $B_x = 50\,\mathrm{mT}$ as function of phase with (red points) and without (brown rhombuses) auxiliary beam illumination. The green cross with dashed guiding lines is obtained with only AUX beam present; as probe beam is closed, no phase stabilization is possible, so the arbitrary phase difference is manually assigned to be 0. Blue squares mark expected values of the signal with both AUX and probe present, a <probe only> curve shifted up by <aux only> value. Lines are guides to the eye. Experimental conditions are: $T = 6\,K$, $\lambda = 864.69\,\mathrm{nm}$ for all beams, and $P_{\mathrm{LO}} = 4\,\mathrm{mW}$.

DBR, Q, a quality factor was chosen to be intermediate, $Q \approx 10^3$ as seen from the simulations, with the thought to avert side effect of high-Q cavities [73, 75] namely, nonlinearities.

Figure 5.8 (a) and Figure 5.8 (b) show the parameters of the peak - width Γ_{HWHM} and amplitude - as a function of the incidence angle, the $B = 50\,\mathrm{mT}$ was fixed. As can be seen, two possibilities were picked up: a) to keep the wavelength the same, which maximize transmission at normal incidence, $\lambda = 864.69\,\mathrm{nm}$ (blue stars) or b) tune the wavelength in accordance with the shifting transmission maxima (red stars).

Using the first option, namely keeping the λ constant, one decrease the amount of light, that reaches QDs, by increasing the angle, as the dash-dotted line tells in Figure 5.4a and Figure 5.8 (b). Still, the collection of the emitted scattered light for this wavelength in the direction of the detection part is the most efficient. The estimated value for the aperture of the collected light cone is $\sim 8^\circ$ (NA$= 0.07$), that is specified by the microcavity Q factor, see Figure 5.4 (a). Keeping that in mind, the case can be explained by the amount of power getting to the QDs through the Bragg structure.

For $\theta < 10^\circ$ the amplitude of the peak do not show significant changes, seemingly because the incoming light still keeps the system at saturation or close to that. Meanwhile the $100\,\%$ drops to about $5\,\%$, or from $2.3\,\mathrm{mW}$ to about $0.1\,\mathrm{mW}$, see Figure 5.7. For greater angles the decay of the excitation power continues beyond the point of being enough, causing the decline in the amplitude as well as peak width, look at Figure 5.8 (a).

The second situation is other, follow the red stars in Figure 5.8 (a) and Figure 5.8 (b). The amount of power coming to the QDs stays close to maximum the whole time, but the outcoupling of the scattered light along the $\theta = 0^\circ$ becomes less and less effective, tracing the dash-dotted line in Figure 5.4a. Rephrasing it, tuning the wavelength to the maximum of transmission chooses the angle, under which the scattered light leaves the microcavity, in this case - along the incoming laser beam. That leads to the fact that the amount of normally out-coupled light drops. Noteworthy, again it is Q factor, defining the solid angle of the detection, which for the high values of Q factor means smaller range of wave vectors and causes trouble to experiments like mentioned in Ref. [14]. The other factor, possibly responsible for the signal reduction is shifting through the QDs sub-ensembles, but as one can see on the picture Figure 5.8 (a), the drop of the PL signal is not more than by 2 from the maxima in the whole range of measurements. Plus, all drastic changes occur from 0° up to 10°, where only the probed side is altered from the low energy to the high energy one and it normally does not make sufficient difference for the SNS [26]. Therefore it can not be accounted for the reason of the observed in experiment vanishing of the signal around $\theta = 10^\circ$.

5.6 Disussion

In the research area of spin noise, it was mentioned first in the Gorbovitskii-Perel paper, that the spin noise one can describe on the language of scattering, which was further developed here, here, here. Still on the experimental side there were made only following advancements. The most clear evidence is the detection of spin noise signal out of the aperture of the transmitted light. To get rid of diffusion broadening mechanism, the localized system - n-doped QDs were chosen. In order to increase the light-matter interaction, they were placed in medium-Q (1000) cavity. To be able to change the angle of incidence, a goniometer part was assembled, and the beam was fed to the fiber to enlighten the beam adjustment. First of all, the normal incidence experiments to check the system parameters, to assure what we see. Then, increase the angle, correct the overlap by the signal amplitude, measure. Surprisingly at first there was little or no changes in the amplitude, then we were able to get to 17°, still seeing the spin noise. As soon as cavity present, we measured the transmission spectra of the cavity, using goniometer and scanning the laser. As one would assume, already at 8° we are already strongly suppressed in terms of transmission. Repeating measurements with wavelength adjustments shows one, what he was waiting for previously: the curve follows the transmission of the cavity. It is now pretty clear, that we should account the focusing and collimating parts separately. When we do not change the probe wavelength, we always allow the scattered light to escape the cavity orthogonally, directly to the detection scheme, we just tune the ”excitation” power lower, which is big enough to keep the signal up to 10° on the constant level. When we do tune the wavelength, we guide the scattered light to be parallel to the probe beam and avoid the detection scheme.

5.7 Summary

As a sub-conclusion, it was demonstrated, that the SN signal is shaped by the parameters of the scattered light, the latter being significantly changed by the DBR structure. Such an effect obviously strongly depends on the Q-factor, therefore one need to use great precaution specifically for high-Q microcavities, so often used in polariton condensation experiments. It is clearly shown, that the spin noise amplitude may be strengthened, given that the system is not saturated. The presence of the phase dependence between probe and side illumination points out the nonperturbing character of the regime and should be taken into consideration in order to understand the spin noise. Some results in this chapter are published in Ref [34].

6 Nonlinear Faraday rotation in crystals, doped with rare earth ions

Crystals doped with the rare earth materials are widely studied by EPR method. EPR and SNS are relatively close methods, but SNS detects the noise of Faraday rotation. According to estimations in [87] RE dopants in crystals do not produce large SNS signal for being detected. On the other hand, in [89], the gain effect is described, which can provide sufficient amplification for the SNS to be detectable. As there can be no SNS without Faraday rotation, we look first on the Faraday rotation in crystals, doped with rare earth ions.

In this chapter we show the novel experimental way to measure *the gain factor* from Faraday rotation amplitude and theoretical approach to validate it. It is demonstrated, that diamagnetic part of the FR in RE-activated crystals depend different on the probe power density for different interconfigurational optical transitions. We use the high resolution nonlinear FR spectroscopy for determination of the homogeneous widths of inhomogeneously broadened transitions and extraction of *the gain factor* of the transitions.

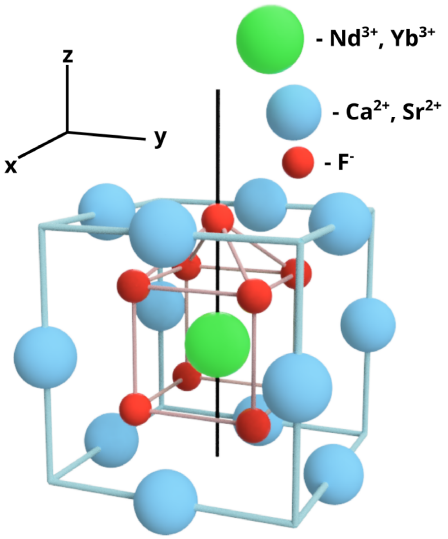

Figure 6.1. Schematic of the unit cell of a crystall with fluorite structure and the RE^{3+} center. An ion of Me^{2+}(blue sphere) is substituted by the RE^{3+} (green sphere) ion. An excess charge is compensated by the interstitial fluorine (red sphere) ion. A consequence of this is a reduction of the center symmetry from cubic down to tetragonal with principal axis (C_4) along the black line through RE-F.

6.1 Spectroscopy of impurity crystals

A structure under study is an ensemble of isolated defects. A simplest single defect is schematically presented in Figure 6.1. The matrix crystal with fluorite structure consists of two interleaving lattices. One lattice has doubly charged cations (blue spheres connected with blue gray rods) and the second lattice has F^- ions (red spheres connected with red gray rods). The doping with RE^{3+} ions (green sphere) occurs in the process of mold crystallization when such ion substitutes one of matrix cations. The excess positive charge is compensated by one F^- ion (red sphere with black rod), which is forced to occupy an interstitial position, causing the reduction of a local symmetry from the cube symmetry (O_h) to the symmetry of the cube with a square pyramid attached to it

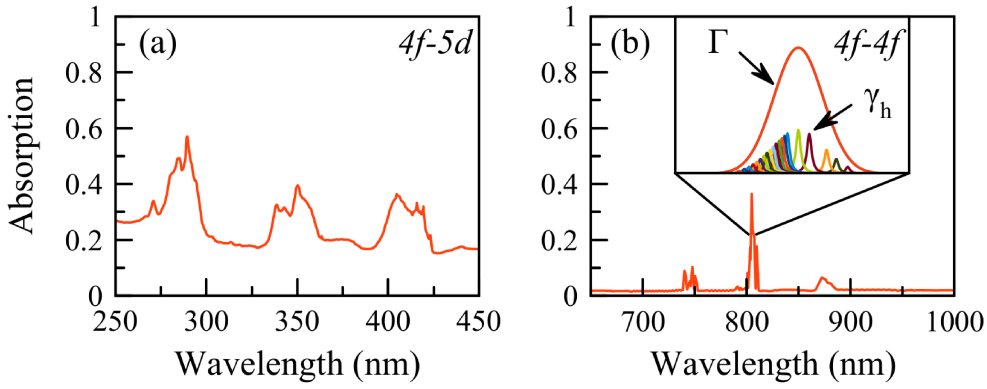

Figure 6.2. An example of different spectra components for rare-earth ions in crystals. ($a_{1,2}$) Typical spectra of absorption taken from [38]. The left and right (short- and long-wavelength) parts of the spectra show the bands of interconfigurational (f-d) and intraconfigurational (f-f) transitions of the ions, respectively.

(C_{4v}). Even though we will further focus only on transitions between deep 4f electron states of the RE^{3+} ion, inherent degeneracy is lifted by the low-symmetry surrounding [32, 33].

The studied system is similar to broadly known nitrogen vacancies in diamond: there is a defect in crystal matrix and an atom not present in matrix bound to it. A special thing about the system it has real atoms instead of artificial ones like in QDs. It is possible to find atoms with intrinsically narrow homogeneously broadened spectral lines. A specific feature of studied rare earth ions (lanthanides) is the presence of unfilled f-shell, where electrons are well shielded from the environment. It gives possibility to preserve the small homogeneous linewidth of transition even when the ion is embedded in crystal without the need to isolate single atoms in magneto-optical trap (MOT).

In addition to the doping with rare earth ions, the crystal has the thermally created defects. In thermodynamic equilibrium defects are uniformly distributed in the volume of the sample. Being in spatial proximity to the studied configuration of atoms Figure 6.1, it can change the transition energy.

Summing each impurity in the probed volume leads us to an inhomogeneously broadened absorption peak, which is composed of homogeneously broadened transitions. In principle, the ratio between homogeneous (γ_h) and inhomogeneous (Γ) broadening in Figure 6.2 (a_2) is not the only possible, the homogeneous one can be dominant as well, as seen in Figure 6.2 (a_1). These two sets of transitions for REE are named interconfigurational (4f-5d) with small Γ/γ_h ratio and intraconfigurational (4f-4f) with large ratio Γ/γ_h. The ratio Γ/γ_h negatively correlates with transition energy: in the UV region homogeneous linewidths are much wider than that of the IR.

The electron transition inside f-shell is normally parity forbidden in dipole approximation, but occurs in RE systems with no center of inversion [32]. If there is an absorption line, there will be a peculiarity in refractive index as a consequence of Kramers-Kronig relation. As a consequence the Faraday rotation amplitude (Figure 6.2 ($b_{1,2}$)) would also be enhanced in this region, if it is present. Estimating the conversion of FR in SNS one can expect that narrower absorption peaks are to have higher amplitude of the noise, but it turns out that the ratio Γ/γ_h is the defining factor (Figure 6.2 ($c_{1,2}$)).

6.2 Absorption and Faraday rotation

As depicted in Figure 6.3 experiments were performed with the method described in chapter 3. The linearly polarized laser beam was cut by iris opened to 2 mm diameter for a more precise management of the power density on the sample. Additionally, balanced photodiodes were replaced fro Newport Nirvana 2007. Due to the presence of the monitoring output for one of diodes, it was possible to calculate the absolute FR angle.

When it comes to the experimental procedure, one needs to keep in mind, that for a solid-state paramagnet solely the high probing power density is not sufficient to omit the paramagnetic term due to used cryogenic temperatures. Additionally, *the gain factor* is actually a relation of inhomogeneous broadening to the maximum value of homogeneous broadening and laser linewidth, which can be limiting factor of *the gain factor* as well. For the mentioned exclusion of the paramagnetic term, measurements are performed with sinusoidal change of magnetic field B_z (along light k-vector), the reference frequency ($f_m = 333$ Hz) from the lock-in was fed to the sound amplifier, which drove the longitudinal electromagnet coils, the output from the diodes was connected to lock in for the signal acquisition. 333 Hz is significantly higher than the inverted T_1 of the ground state sublevels.

The weak Faraday rotation of f-f transitions may give rise to a strongly enhanced spin noise power due to a large ratio of Γ/γ_h [89].

Among all the available crystals were chosen already relatively well known and studied SrF_2 co-activated with Nd^{3+} (0.5 mol %) and Yb^{3+} (0.15 mol %) and CaF_2:Nd^{3+} (0.1 mol %), as shown in Figure 6.4 (a). As the SNS is a mapping of medium magnetization on the polarization of the light, solely absorption presence does not guarantee one to see SN spectra at this transition.

For the accomplishment of measurements of the FR spectra, were chosen sole lines among the observed f-f transitions of Nd^{3+} and Yb^{3+} ions in the CaF_2 and SrF_2 matrices. The reason is that for a more complicated structure ambiguity during the peak identification does not allow produce any reliable result with such a simple model. Illustrative case depicted in Figure 6.4 demonstrates the development of the FR spectra of the transition at 862.68 nm of Nd^{3+} in CaF_2 with growth in probing power density. With respect to the literature [30] it is transition of the tetragonal center with very long-living excited state, ~ 1.5 ms.

One can see the transmission spectra in Figure 6.4 (a), there is an oscillating background from 75 % to 100 % due to the laser etaloning on the sample. Five sharp lines are clearly distinguishable: 859.31 nm with 56 % transmission, 860.68 nm with 45 % transmission, 862.24 nm with 35 % transmission, 862.69 nm with 70 % transmission and 863.79 nm with 52 % transmission. In comparison with the literature data [30], we assign the lines to Nd.

A good measure for magneto-optical activity is a Faraday rotation angle, the spectrum of its amplitude is given in Figure 6.4 (b) for different power densities of the probing light. The line at 862.69 nm have a pronounced increase of Faraday rotation with growing light intensity. The change in the form of the peak is best visible in the inset in Figure 6.4 (b): from an M form it goes to a simple Gaussian-like shape with a changed sign. The behavior of other transitions can be seen on a zoom of Figure 6.4 (b) in Figure 6.4 (c). Remarkably, lines with wavelength shorter than 861 nm do not change significantly neither in amplitude, nor in form, it is best seen in a further zoom in Figure 6.4 (c).

FR spectrum at several minimal power densities, which still should relate to the linear regime are seen in the inset, as well as its described beforehand behavior: low-power regime provides

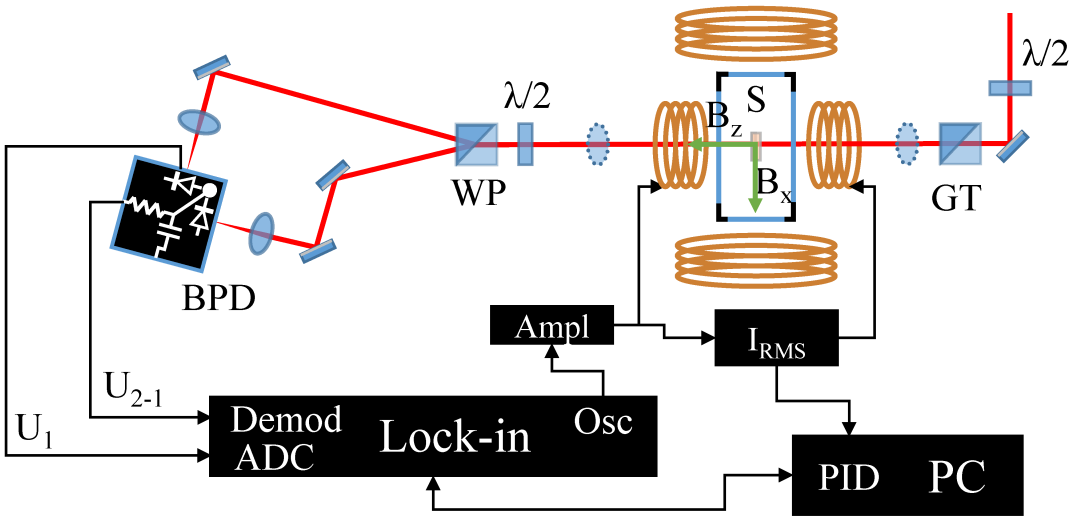

Figure 6.3. The drawing shows the experimental setup for the diamagnetic FR measurement: transmitted through the sample laser light is analyzed with the balanced photodiodes. A $\lambda/2$ and a Glan-Taylor (GT) prism after the laser allow one to control the incident power and the direction and quality of the linear polarization of the beam. A pair of lenses (L_1, L_2) were used for the high power density and were removed for the low power density measurements; the iris opened at 2 mm ensured the overlap of these regions. The audio amplifier works perfectly for 8 Ohm coils of the electromagnet and allows one to apply the AC magnetic field in the longitudinal direction with a very stable frequency, defined by the internal oscillator of the lock-in amplifier. The transmitted beam polarization is analyzed by a $\lambda/2$, and a Wollaston prism (WP), the signal from one diode (I_1) and the difference of $I_1 - I_2$ are fed to lock-in to be able to get the absolute rotation in a single measurement.

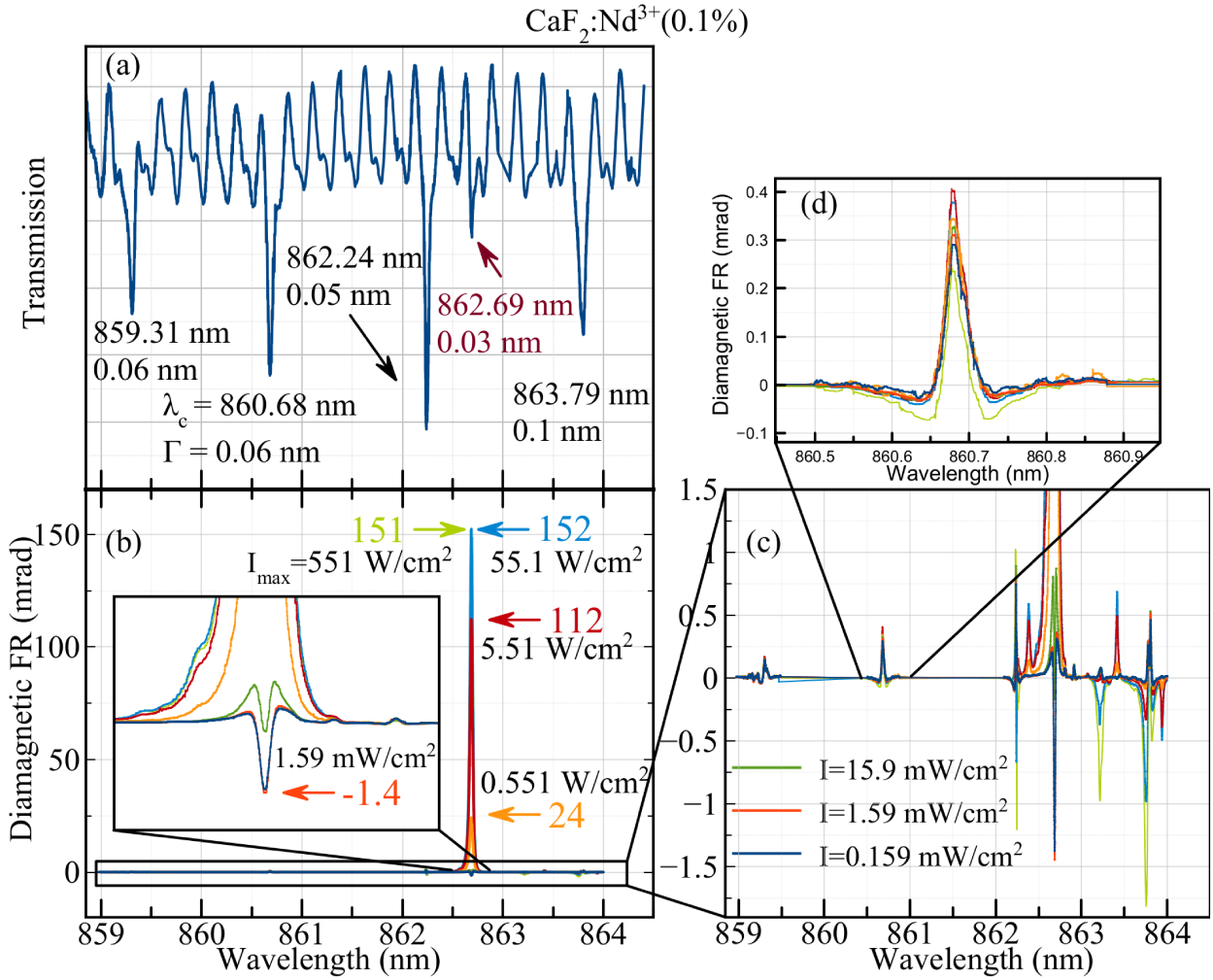

Figure 6.4. Laser scanning transmission spectra (a) and Faraday rotation spectra (b,c,d) for the CaF_2-Nd (0.1 mol %) crystal cooled down to 5.6 K. In pane (a) the transition with a measurable SN signal is marked with a different color. Faraday rotation spectra dependence on probe power density is shown in full scale in pane (b). Rotation amplitudes are written in colored font adjacent to horizontal arrows and corresponding values of laser power density. The unperturbed form of the peak is seen in the inset in pane (b) with its amplitude and maximal unperturbed power. For a bipolar signal logarithm scale is not suitable, so a magnified part of pane (b) of the same spectral range is shown in pane (c). One sees that there are other lines, that do change with the increase of power density, but even at its maximum intensity neither overcomes unperturbed value for line 862.69 nm. A more peculiar behavior is clearly seen on pane (d) for an identifiable transition: there is almost no change through all the measured power density range.

the second-derivative of Lorentzian line shape, with consistent enlargement of the incident power, FR in the center of the transition inverts its sign and explosively rises in amplitude (two orders of magnitude for the measured case). But such a behavior is not the only possible one, in Figure 6.5

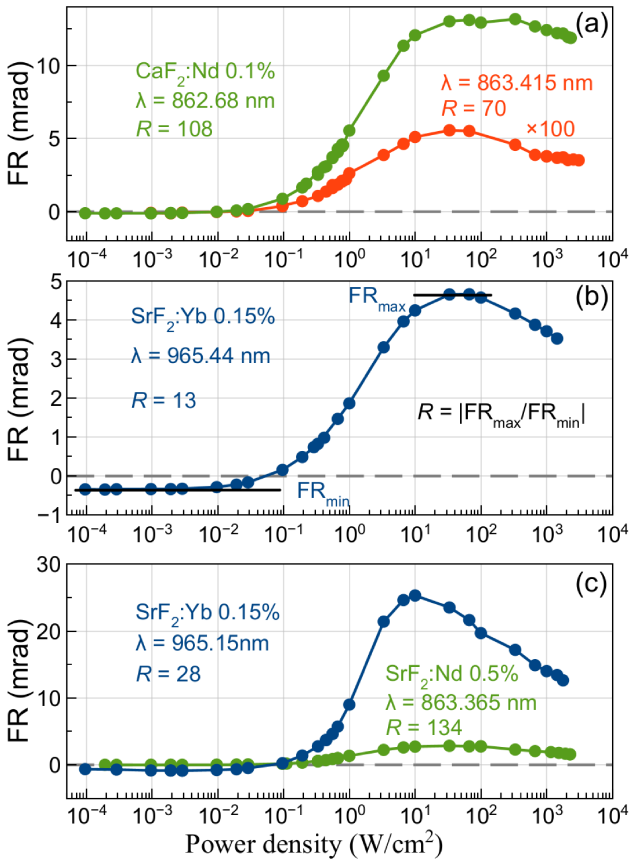

Figure 6.5. A set of experimentally obtained values for the FR in the middle of different absorption lines as a function of the probing power density at $T = 6\,\mathrm{K}$ with magnetic field $B_\sim = 0.3\,\mathrm{mT}$, $f_m = 333\,\mathrm{Hz}$. Studied transitions are identified by the matrix crystal name, dopant element with its concentration and λ, the centre wavelength of the absorption peak. The FR enhancement factor $R = |\mathrm{FR_{max}}/\mathrm{FR_{min}}|$, see panel (b).

one sees the complex transition between 859 and 859.5 nm that does not change even tiny bit at highest achieved power density, but being not identifiable, therefore the other one is presented in the inset. From Ref. [30] transition on 860.7 nm should be the Nd^{3+} M-center (pair center), which experience accelerated cross-relaxation between the levels of the Nd ions embodying the center, it leads to extreme shortened lifetime, 92 μs. One sees in Figure 6.4 that even at highest achieved probing power density the inversion of the sign did not occur, therefore it is fair to assume the line to be predominantly homogeneously broadened with little to no spectral hole produced.

For isolated lines we can reliably plot the amplitude of the Faraday rotation as a function of the light power density, the result is in Figure 6.5. For the CaF_2-Nd (0.1%) in Figure 6.5 (a) one sees in green the most prominent line, and in red the other one, multiplied by 100 times for the visibility. The green one goes from -0.12 up to 13 mrad, the red one from $-1.2{\cdot}10^{-3}$ to $6{\cdot}10^{-2}$ mrad. In pane Figure 6.5 (b) one sees clearly, that amplitude goes from a small negative value -0.3 to a higher positive 5 mrad for another element - Yb - in a different matrix - SrF_2. R is the absolute

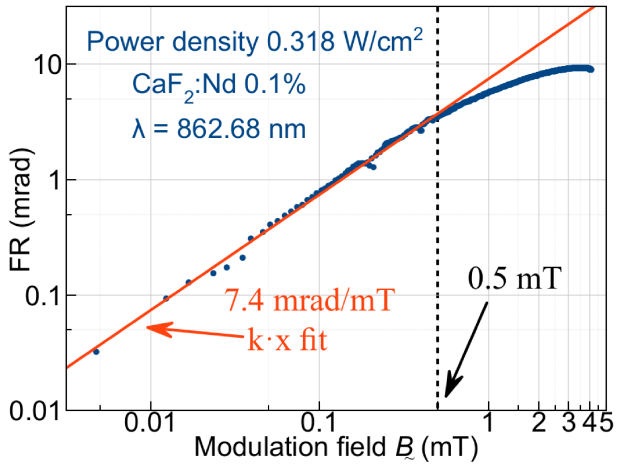

Figure 6.6. Saturation of the FR amplitude with the modulation field's growth at $T = 6\,\mathrm{K}$, $f_m = 333\,\mathrm{Hz}$. The estimated position of the breaking point is 0.5 mT and is marked by a vertical dashed line.

value of the ratio maximal to minimal Faraday rotation. In Figure 6.5 (c) we see case for lines for two different dopants on corresponding lines: on Yb from -0.8 to 0.025 mrad and on Nd from $-2.1{\cdot}10^{-2}$ to 2.8 mrad.

The increase of Faraday rotation amplitude is not unique for a chosen sample: we can change the matrix material and the dopant, as in Figure 6.5, and see the dependence of the amplitude on light power density at the center of the corresponding absorption line. From the theoretical expressions, the homogeneous width of the transition may be extracted by obtaining the coefficient of magnification of the nonlinear FR (R). In Figure 6.6 the results of the dependencies of the FR in the middle of transition on the probe intensity for a set of picked up transitions in the selected crystals. Their common performance corresponds to the modeled in Figure 6.7.

We define R as shown in Figure 6.5 (b) as the ratio of maximum to minimum Faraday rotation angles. It will be shown later that R is proportional to the ratio of inhomogeneous to homogeneous linewidths, which is a crucial parameter for the SNS. The described way makes it possible to use only one beam (see Figure 6.3) tuned to the absorption center, in contrast to the pump-probe method.

Both curves in Figure 6.5 (b) and blue curve in Figure 6.5 (c) correspond to transitions, that show SN signal. We can compare different lines of the same dopant to figure out the most crucial for the suitability for SNS: the difference in R and bare maximal amplitude of Faraday rotation angle.

Speaking of Faraday rotation spectra, for highest signal-to noise ratio one wants the magnetic field magnitude to be maximum possible one. The upper limit for the applied field is achieved when signal starts to drop: the Zeeman effect cause line splitting, effectively detuning laser from the transitions. In Figure 6.6 we see that the chosen magnetic field lies within the linear region and is fully acceptable for the measurements. This measurement also allow us to estimate the homogeneous linewidth.

6.3 Theoretical description

Assumptions for the forthcoming equations: $\bar{\omega}$ is the center of the inhomogeneously broadened transition, its spectral form is given by $\mathcal{P}(\omega) > 0$ ($\int \mathcal{P}(\omega)d\omega = 1$), so that $N\mathcal{P}(\omega_0 - \bar{\omega})d\omega_0$ gives the number of impurity centers pro unit volume, which transition frequencies do lay in borders $[\omega_0, \omega_0 + d\omega_0]$. With that in mind, the diamagnetic term can be rewritten:

$$\phi_A(\omega) = V \int d\omega_0 \mathcal{P}(\omega_0 - \bar{\omega}) p(\omega_0) \frac{\partial}{\partial \omega} f(\omega_0 - \omega). \tag{6.1}$$

As one sees from Equation 2.7 and Equation 6.1, $\phi_A(\omega)$ spectral shape follows that one of the derivative of the refractive index $n_\pm$ (at $\omega_L = 0$).

Low probing power densities leave the system almost untouched, therefore there is no discrepancy between the population of distinct spectral components $p(\omega_0) = p_{eq}$. With intensification of probing, arises the contrast betwixt close-to-resonance transitions and those located further in spectrum, which is known as a hole-burning effect, leading to the nonlinear FR.

For the linear case FR expectancy can be received as follows: the function $\mathcal{P}(\omega)$ differs from zero significantly within the borders $\omega \in [-\Gamma, \Gamma]$, where $\mathcal{P}(\omega) \sim 1/[2\Gamma] \equiv \bar{\mathcal{P}}$. Under this circumstances Γ stays for the inhomogeneous width and appears to be overwhelmingly bigger in comparison to γ_h. Let ϕ_{A0} be the FR at the center of the inhomogeneously broadened line ($\bar{\omega}$) measured far away from saturation, with considerations above one gets an approximation by setting $\omega = \bar{\omega}$ in Equation 6.1:

$$\phi_{A0} \sim -V p_{eq} \bar{\mathcal{P}} \int_{\bar{\omega}-\Gamma}^{\bar{\omega}+\Gamma} \frac{\partial}{\partial \omega_0} f(\omega_0 - \bar{\omega})\, d\omega_0 = -\frac{V p_{eq} \bar{\mathcal{P}}}{2\Gamma}. \tag{6.2}$$

Now, for the other limit case, optical saturation, FR is ϕ_{A1}. As mentioned before, this means that $p(\omega_0)$ receives deformity in the region $\omega_0 \approx \bar{\omega}$, where a spectral "hole" appeared. Let its form be a Gaussian-like $\mathcal{L}(\omega)$, with maximum at $\omega = 0$, an amplitude in range $0 < \mathcal{L}(\omega) < 1$ and a width of $\tilde{\gamma} > \gamma_h$. With that, the formula for $p(\omega_0)$:

$$p(\omega_0) = p_{eq}[1 - \mathcal{L}(\omega_0 - \bar{\omega})]. \tag{6.3}$$

From common sense or cumbersome theoretical calculations one can get restrictions, imposed on the function $\mathcal{L}(\omega)$: the magnitude of drop $\mathcal{L}(0)$ must change with the beam intensity I from $\lim_{I\to 0} \mathcal{L}(0) = 0$ to $\lim_{I\to\infty} \mathcal{L}(0) = 1$, as for FWHM $\tilde{\gamma}$ its lower limit is obviously $\lim_{I\to 0} \tilde{\gamma} = \gamma_h$, it should also stay close to it for $\mathcal{L}(0) \ll 1$ and start grow for higher powers.

Putting Equation 6.3 into Equation 6.1 and making the assumption $\Gamma \gg \tilde{\gamma}$, one can get for the FR angle ϕ_{A1}:

$$\begin{aligned} \phi_{A1} &= \phi_{A0} + V p_{eq} \int d\omega_0 \mathcal{P}(\omega_0 - \bar{\omega}) \mathcal{L}(\omega_0 - \bar{\omega}) \frac{\partial}{\partial \omega_0} f(\omega_0 - \bar{\omega}) \approx \\ &\approx \phi_{A0} + V p_{eq} \mathcal{P}(0) \int d\omega_0 \mathcal{L}(\omega_0 - \bar{\omega}) \frac{\partial}{\partial \omega_0} f(\omega_0 - \bar{\omega}). \end{aligned} \tag{6.4}$$

Combining the facts that the function $\mathcal{L}(\omega_0 - \bar{\omega})$ significantly differs from zero at $\omega_0 \in [\bar{\omega} - \tilde{\gamma}, \bar{\omega} + \tilde{\gamma}]$ (where $\sim \mathcal{L}(0)$), and that $\mathcal{P}(0) \sim \bar{\mathcal{P}}$, the formula for ϕ_{A1} modifies to:

$$\phi_{A1} \sim \phi_{A0} + V p_{eq} \bar{\mathcal{P}} \mathcal{L}(0) \int_{\bar{\omega}-\tilde{\gamma}}^{\bar{\omega}+\tilde{\gamma}} d\omega_0 \frac{\partial}{\partial \omega_0} f(\omega_0 - \bar{\omega}) \sim V p_{eq} \bar{\mathcal{P}} \left[\frac{\mathcal{L}(0)}{2\tilde{\gamma}} - \frac{1}{2\Gamma} \right]. \tag{6.5}$$

Remembering the above-mentioned restrictions on $\mathcal{L}(0)$ and $\tilde{\gamma}$, this function behave the following way: first rises ($\mathcal{L}(0)$ increases), then arrives to its supremum at $I = I_c$ and starts the gradual decay ($\mathcal{L}(0) \approx 1$, $\tilde{\gamma}$ increases). Equation 6.5 tells us that at some point the sign will be flipped, meaning that ϕ_{A1} is of opposite sign to ϕ_{A0}.

Apart of it, Equation 6.5 makes it possible to estimate *the gain factor* (ratio Γ/γ_h), that is very significant (Ref. [35]) for the SNS to be observable on a chosen dopant ion. At I_c, depth $\mathcal{L}(0)$ is almost 1, but FWHM $\tilde{\gamma}$ is still in the vicinity of the homogeneous width γ_h. Connecting Equation 6.5 and Equation 6.2, the conveniently accessible in the experiment ratio $R \equiv \phi_{A1}/\phi_{A0}$ may be approximately evaluated:

$$R|_{I=I_c} = \frac{\phi_{A1}|_{I=I_c}}{\phi_{A0}} \sim \frac{\Gamma}{\gamma_h}. \tag{6.6}$$

With this, big number for *the gain factor* does relate not only to the "giant SN gain effect" [35], but to a "giant nonlinear FR" as well.

Not being a part of this work, the thorough theoretical and numerical expressions lead to the following formula for the ratio R:

$$R = \frac{\Gamma^2 + \gamma_h^2}{\Gamma\gamma_h} \frac{\pi s}{2\sqrt{s+1}\left(\sqrt{s+1}+1\right)^2} - 1, s \equiv \frac{\Omega_R^2}{\gamma_h \gamma^{exc}}. \tag{6.7}$$

$\Omega_R \sim \sqrt{I}$ and γ^{exc} being the Rabi frequency and the excited-state decay rate, correspondingly. Illustration for the reliance $R(s)$ is demonstrated in Figure 6.7 The general behavior fulfills the expected one from the nonlinear FR: with monotonous growth of probing power density, the modulus of FR decreases until FR crosses zero and then increases with the inverted phase up to much higher values.

Conventionally $s \sim I$ stays for the *saturation factor*. Fraction with all s in Equation 6.7 has a supremum 0.27 located at $s = s_c = 4.81$, which is equivalent for the above-mentioned I_c.

Under above-mentioned assumption $\Gamma \gg \gamma_h$, Equation 6.7 provides a more precise outcome than the estimation in Equation 6.6:

$$R|_{I=I_c} = 0.27\frac{\Gamma}{\gamma_h}. \tag{6.8}$$

With this formula one can perform approximate evaluation of the homogeneous width from *the gain factor* and therefore the applicability of the SNS to the studied system.

6.4 Comparison of experimental results with theory

In Table 6.1 one finds the outcome of the determined from the experiment homogeneous linewidths of the considered transitions and Equation 6.8. It turned out that the γ_h is on the same order of magnitude for each end every examined via nonlinear FR transition - a few tens of MHz. As this value strongly deviates from the expected kHz range, an alternative way to check the accuracy of obtained results needs to be implemented. For that purpose was used the fact that amplitude

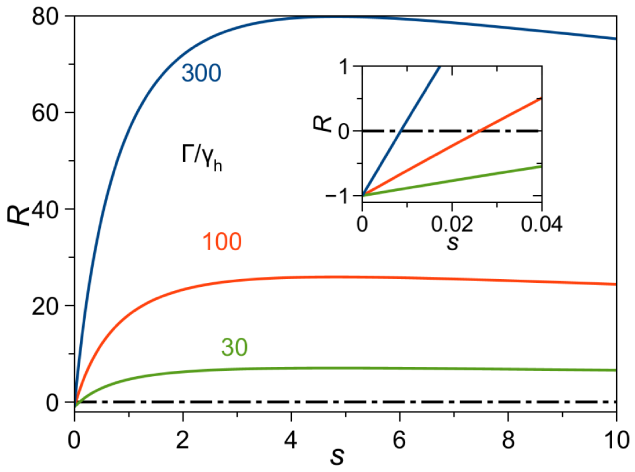

Figure 6.7. Dependence of the resonant nonlinear FR (in units of linear FR) on the probe beam intensity (in units of the saturation factor s) for three values of the ratio Γ/γ_h. The inset shows an inversion of the FR sign at low light intensities.

Table 6.1. Evaluation of the homogeneous width for some transitions of Nd^{3+} and Yb^{3+} in the studied crystals. λ is the probe wavelength at the transition, R is the FR enhancement factor, Γ is the measured spectral width of the transition, and γ_h is the homogeneous width of the transition, calculated using Equation 6.8.

Crystal	λ, nm	R	Γ, GHz	γ_h, MHz
SrF_2-Yb (0.15%)	965.44	13	2.68	44
SrF_2-Yb (0.15%)	965.15	28	4.0	31
SrF_2-Nd (0.5%)	863.365	134	26.8	54
CaF_2-Nd (0.1%)	862.68	108	15.2	38
CaF_2-Nd (0.1%)	863.415	70	12.8	50

of FR depends linearly on the magnetic field only if the Zeeman splitting is smaller than the linewidth, which works for the dependence of amplitude of nonlinear FR on the amplitude of oscillating magnetic field as well, the linewidth being the width of the burned spectral hole. So the approximate evaluation of the width may be made via scanning the amplitude of the magnetic field and recording the FR. That experiment was accomplished on the 862.68 nm line of Nd^{3+} in CaF_2, outcome is plotted in Figure 6.6. Power density, 0.3 W/cm^2 was chosen in the region of linear dependence of the nonlinear FR on probe power density - see Figure 6.6- where the FWHM of the spectral hole stays almost unaffected by the laser light. Noteworthy, the magnetic field amplitude for Figure 6.6 lays in the linear regime - see Figure 6.6 to justify the used small field approximation. In Figure 6.6 one identifies that divergence from a line occurs near 0.5 mT, this field corresponds to $g\mu_B B/h \approx 21$ MHz for the mean g factor 3. Such result lays close to the precisely obtained values in Table 6.1.

The theoretical calculations of the value are done in the work [35] or [48], where the following formulae [61] was used to get the magnetic dipole-dipole interaction, leading to the homogeneous broadening:

$$\gamma_h = \frac{\tilde{k} C \tilde{g}^2 \mu_B^2}{\hbar}, \tag{6.9}$$

$\tilde{g}$ being the characteristic g-factor of the impurity ion, $\tilde{k} \sim 2.53$ being a numerical parameter, ruled by the relative values and signs of two pairs of g-factors of the ground and excited states of the ion, and C being the impurity concentration. The approximate evaluation of γ_h with the help of Equation 6.9 for the tetragonal Nd^{3+} center in the CaF_2 crystal with $C = 2.46 \cdot 10^{19}$ cm^{-3} and $\tilde{g} = 4$ leads to $\gamma_h = 2\pi \cdot 16$ MHz, that without taking in account other possible broadening mechanisms and considering the experimental error is in a good agreement with the measured values of γ_h for the transitions listed in Table 6.1.

No results from the literature were acquired for experimentally measured homogeneous linewidths of the f-f transitions in exactly these transitions. Still, for other cases, different REE and their f-f transitions, reported values lay in the range from tens of Hz to several GHz [56, 54]. Specifically, in Ref. [7] the homogeneous width of the f-f transitions of Nd^{3+} in CaF_2 at 9 K was as high as 350 MHz. Such works dedicated mostly to the seeking for the narrowest transitions, as they are of interest for possible applications [57, 64, 83]. This work was not targeted for the optimization to lessen the homogeneous linewidth of the transitions, so with alternative RE-doped crystals and another transitions, it should be possible to observe even higher *the gain factor*, even by orders of magnitude.

6.5 Conclusions

In this part of the work particular peculiarities have been shown for the nonlinear resonant Faraday effect observed on the f-f transitions of trivalent rare-earth ions in crystals. It was demonstrated that in case of strongly inhomogeneously broadened transitions adequately strong probing, the diamagnetic term of FR can be boosted to be by orders of magnitude larger than itself at smaller power densities. I.e. *the gain factor*, being gigantic for SNS, hidden in the regular *linear* Faraday rotation may be unveiled in the *nonlinear* one, which becomes evenly gigantic. Performed measurements also approve the connection between the SNS amplitude and the homogeneous width

of the transition. Applied method of probing the optical transitions is good not exclusively for proofing the applicability for SNS to the system, but also as a single-beam approach for extracting the homogeneous width of the optical transitions of paramagnetic impurities in crystals.

Most of the presented results were published in [37].

7 Giant spin noise gain in crystals, doped with rare earth ions

As described theoretically in Ref. [89], the noise of the Faraday rotation in case of resonant probing can be significantly magnified by *the gain factor* and overcome its FR per unit spin density by orders of magnitude. *The gain factor* is the ratio of the inhomogeneous width to the homogeneous one.

In this chapter, triumphal experimental realization of detection of the ground-state magnetic resonance is performed on crystals with RE ion impurities due to the f-f transitions, which homogeneous and inhomogeneous widths are expected to be from kHz to GHz range.

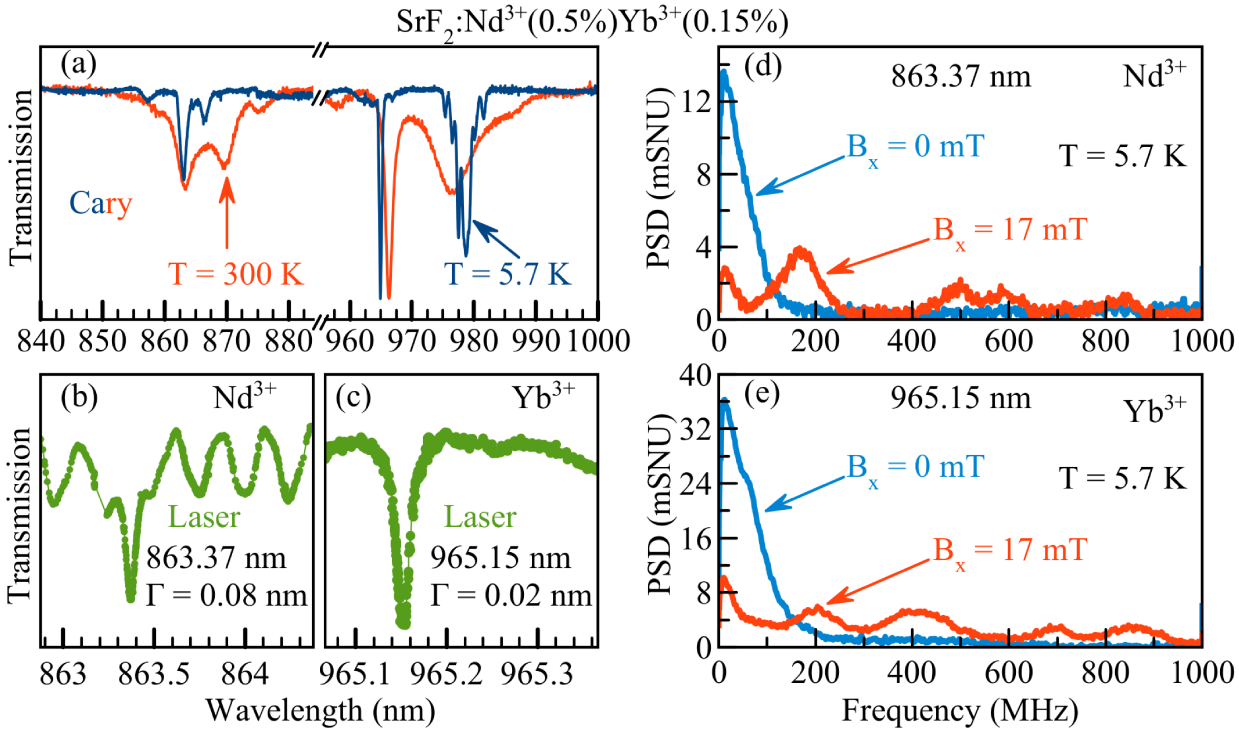

Figure 7.1. Transmission and SN spectra of the SrF_2:Nd^{3+} (0.5 %)Yb^{3+} (0.15 %) crystal. (a) Transmission spectra were obtained using a Cary spectrophotometer with a spectral resolution of 0.05 nm. (b,c) High-resolution Scanned-Wavelength Direct Absorption Spectroscopy performed with a tunable Ti:sapphire laser, beam power is 1 mW. The oscillating background signal is produced by a laser etaloning at the sample surfaces. (d,e) The magnetic field dependence of the SN power spectrum density (PSD) for the Nd^{3+} and Yb^{3+} ions, respectively. The spectra are detected for the same crystal orientation with respect to the magnetic field and light propagation. Colorful arrows mark the corresponding magnetic fields at which the spectra in shot noise units (SNU) are taken.

7.1 Spin noise spectroscopy on rare earth elements

It was previously [87] strongly believed, SNS signal on REE is too weak to be detected with reasonable experimental conditions.

Reasoning is simple: highest magneto-optical activity is observed in media with strong and narrow peculiarities in optical spectrum, therefore in SNS one needs to precisely tune laser wavelength. Crystals and glasses with REE have two types of transitions: allowed interconfigurational are mostly spectrally broad and narrow intraconfigurational are parity-forbidden, therefore, weak. Both of these terms seem to give small contribution to the refractive index. A good semiquantitative analysis is given in [87] with the help of the concept of the FR cross-section σ_F [24]. It turned out, that in bulk n-doped GaAs, which is both well studied by SNS and giving signals close to the edge of detection capabilities, the σ_F is on order of 10^{-15} rad cm^2. For the most prominent paramagnet from REE, CaF_2:Tm^{2+} σ_F is only 10^{-19} rad cm^2 even for strong interconfigurational transitions, being even smaller for intraconfigurational ones [58]. But in this chapter we are showing that SNS signal detection on classical EPR system -REE- is possible.

As specimens for SNS we use samples described in chapter 6: SrF_2:Nd^{3+} (0.5 %)Yb^{3+} (0.15 %) and CaF_2:Nd^{3+} (0.1 %) crystals. The transmission spectra in Figure 7.1 (a,b,c) are measured in regions, where transitions for Nd^{3+} and Yb^{3+} are expected. By cooling down from room temperature to helium one, absorption peaks narrow down to width unresolvable by the spectrophotometer. At low temperature a tunable laser direct Absorption Spectroscopy Figure 7.1 (b,c) is used to precisely determine the absorption line width for both Nd^{3+} and Yb^{3+}. Noticeable background modulation for laser scans originates from etaloning on sample.

Spin noise spectra in Figure 7.1 (d,e) are obtained with setup scheme in Figure 5.1. PID stabilizes laser wavelength on the center of the chosen transition. Each experimental line is the difference between spectra with scattered light and without. Such approach allows one to overcome spectra distortion at 0 Hz frequency caused by Faraday rotation taking place when magnetic field is modulated. To check that the visible at $B = 0$ mT peak relates to SNS, we apply magnetic field $B = 17$ mT and see a clear separation into several magneto-dependent components for both of the studied elements Figure 7.1 (d,e).

Actually the possibility to see the Larmor precession selectively originates from the optical nature of probing and is the significant advantage of optical SNS over conventional EPR measurements, where all transitions from both ions are visible simultaneously, making the interpretation of the experimental data significantly more cumbersome.

In principle single spectra at fixed known magnetic field like in Figure 7.1 (d,e) can be used to define the g-factors of the peaks, but a magnetic field series is more reliable both in terms of accuracy and peak-to-peak resolution. In Figure 7.2 we see single spin noise spectra for Nd^{3+}(a) and Yb^{3+}(b) along y-axis being stacked for transversal magnetic field up to 27 mT. Color-encoded amplitude of spectra makes it easier to notice that each of the components follows the linear trend, dictated by the Zeeman effect:

$$E_Z = \mu_B g B_{ext} m_j. \tag{7.1}$$

Despite the seemingly simple relation, the presence of two kind of atoms can cause additional reduction of the defect local symmetry, making the theoretical description and interpretation of experimental data too complicated for the scope of this work.

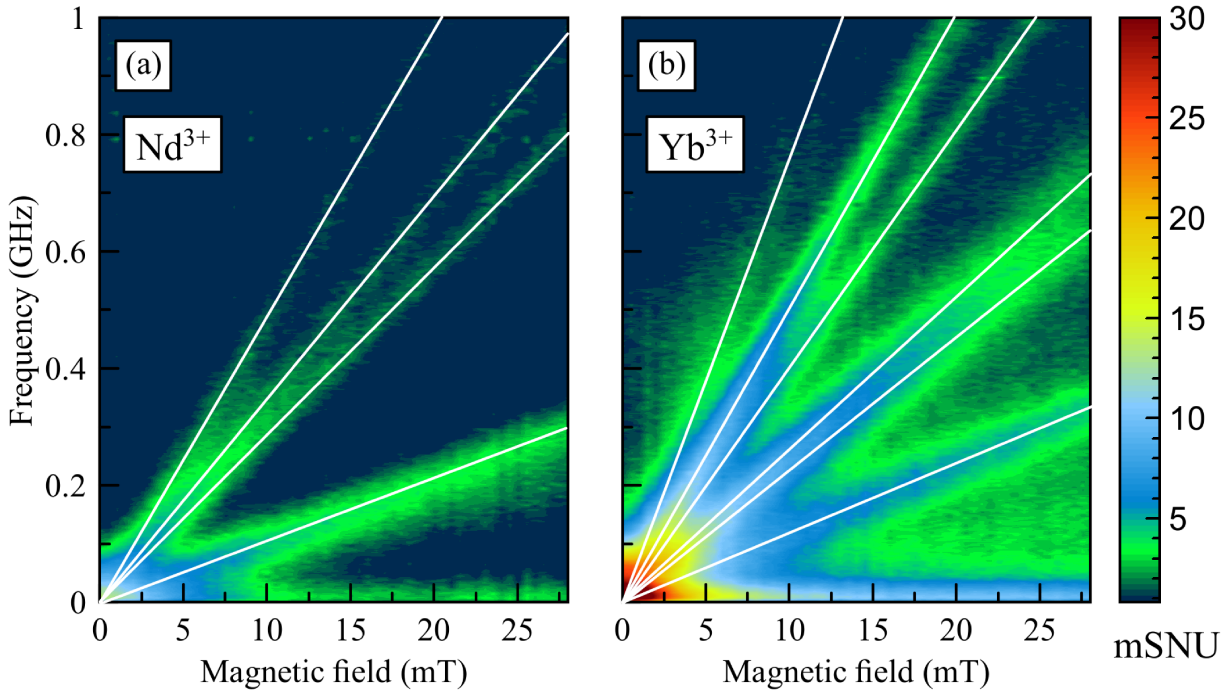

Figure 7.2. Dependencies of SN spectra on magnetic field for the SrF_2:Nd^{3+} (0.5 %)Yb^{3+} (0.15 %) crystal. Color maps demonstrate the behavior of the SN power spectrum density (PSD) for the Nd^{3+} and Yb^{3+} ions with increasing magnetic field. The spectra are detected for the same crystal orientation with respect to the magnetic field and light propagation. White lines are guide for the eye, showing Larmor frequency shift for different components, that normally determine the g-factor values for the involved spin carriers.

For the simplification of the above-mentioned procedures, we now focus on the sample with only Nd impurity. Laser scanning transmission spectrum in Figure 7.3 (a) reveals several absorption lines, that belong to the Nd^{3+} ion. These multiple absorption lines differ in both amplitude and width. For spin noise measurements in Figure 7.3 (b) and further we chose the line at $\lambda = 862.69$ nm as other lines did not show any noticeable signal. The detailed explanation of such behavior is given in chapter 6.

To check spin noise origin of the seen peak at $B = 0$ mT, we look for split components at nonzero magnetic field, in Figure 7.3 (b) it is $B = 17$ mT. The green Gaussian fit perfectly covering the experimental data shows that the studied system is a strongly inhomogeneously broadened ensemble, as the signal ought to be a Lorentzian curve for a homogeneously broadened system.

We see SNS as a function of magnetic field in Figure 7.4 (a). In nonzero magnetic fields one notice five distinct peaks, frequencies of which linearly Equation 7.1 increase with the increase in magnetic field. Let us notice, that for the experiment was picked up a geometry, where magnet field was oriented along one of the sample sides. To determine the g-factor tensor one needs to check all the possible orientations of the magnetic field with respect to the crystal. To achieve this goal we fixed the direction of the magnetic field and turned the sample along the light k-vector axis. Obtained values for g-factors one can see in Figure 7.4 (b).

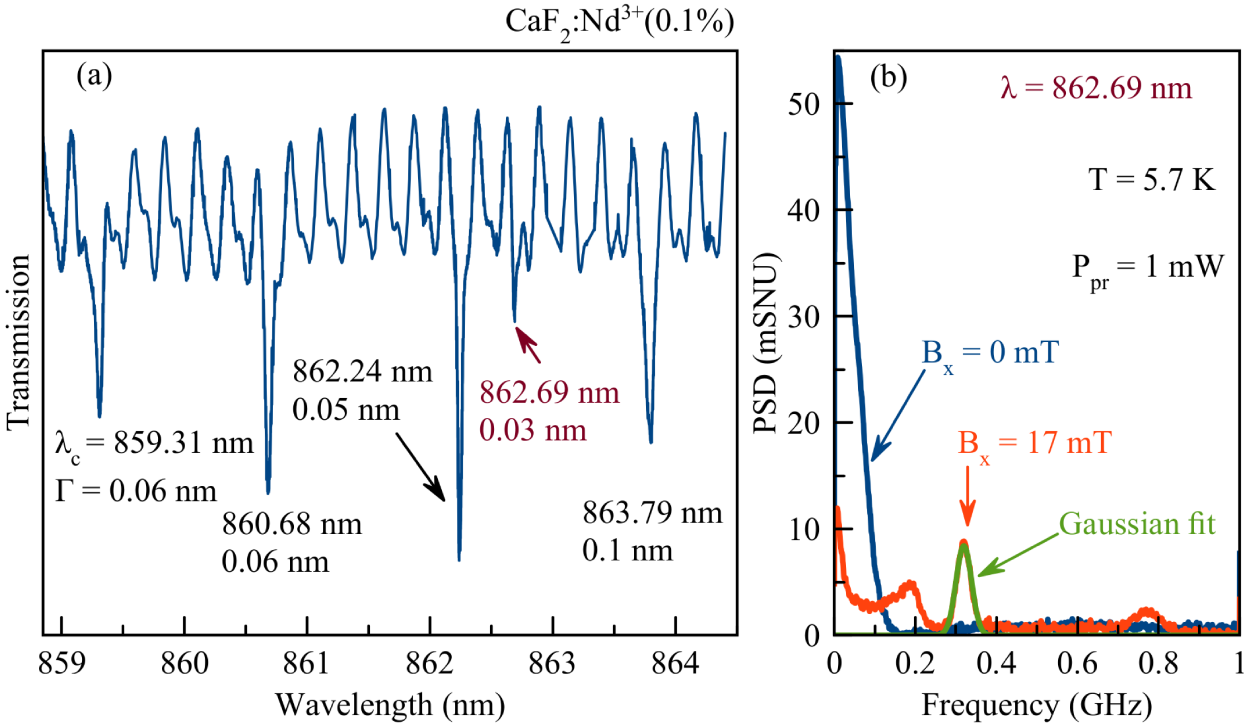

Figure 7.3. Transmission and spin noise spectra of the CaF_2:Nd^{3+} (0.1 %) crystal. (a) The laser transmission spectrum of the sample at 5.7 K. The oscillations are due to the etaloning effect of the laser by the sample. (b) The exemplary SN spectra detected at the absorption peak 862.69 nm at $B = 0$ mT and at $B = 17$ mT at the laser power of 1 mW. The most pronounced peak is well fitted by Gaussian function, pointing out the inhomogeneous nature of the detected signal (otherwise it would be Lorentzian).

CaF_2 is a cubic crystal, and g-factor tensor, being only the second rank one, cannot distinguish cubic lattice from isotropic medium, which is represented by just one independent value. Still, one needs to account for the lower local symmetry of the impurity, which in our case has only tetragonal symmetry, leading to 3 independent parameters. The problem is that the 3 independent parameters lie on diagonal only in the frame of reference of the impurity center, which can be arbitrarily rotated from the laboratory frame of reference. Using crack in the sample as a hint for its main axes is not reliable, as one can not trace the movement of peaks between the discrete steps shown in Figure 7.4 (b).

For the possible peak identification further modification of the method is essential, and is discussed in the next session.

7.2 Invariants in crystals, doped with rare earth ions

Peaks in spin noise spectra can originate from more than one defect type, each with its own g-factor tensor. To separate components of one g-factor tensor from another we study the SN angular dependence. We choose not to rotate the sample respective to the magnetic field direction: with

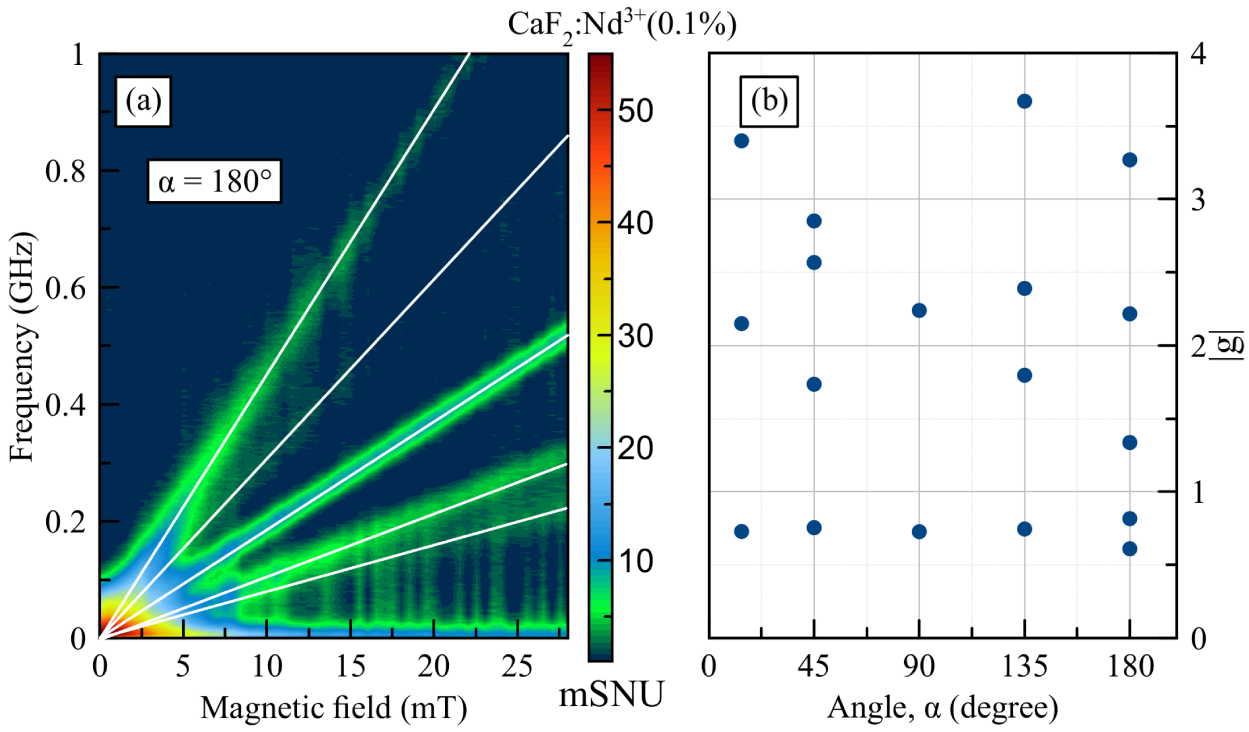

Figure 7.4. (a) Spin noise spectra magnetic field dependence in the form of color map for the CaF_2:Nd^{3+} (0.1 %) crystal with cleave oriented at 180° to the laboratory y-axis. Laser energy adjusted to match the absorption peak at 862.69 nm, laser power being 1 mW. (b) Extracted slopes for Larmor peak shifts at different orientations of the crystal cleave to the laboratory y-axis.

the current sample holder it would lead to a different probed volume. This change render results unreliable, as the sample is not uniform. To minimize the change in experimental conditions we fixed the point on sample and rotated the magnetic field. The modified setup is presented in Figure 7.5: the holder with the disk-shaped magnet can rotate perpendicular to the cylinder axis, keeping the fixed distance to sample. The magnetic field magnitude is defined by this distance and was calibrated by SN peak frequencies with B_x-dependencies from the electromagnet only.

In Figure 6.1 we illustrate a single defect with its symmetry axis along z direction, but it can be oriented along any of xyz axes. As the macroscopic crystal symmetry is cubic, all three configurations are degenerate and in thermodynamical equilibrium be equal amount of defects oriented along x-, y- and z-axis. For each orientation the reference values of the defect ground-state g-tensor are identical: $g_{\parallel}$ = 4.412 and $g_{\perp}$ = 1.301. [2]. Three projections of the g-factor tensor on an arbitrary oriented magnetic field results in three different components of the Zeeman splitting, which we observe as SN peaks. The experimentally obtained dependence of SN spectra on the magnet rotation angle is shown in Figure 7.6 as a color map. With the change of magnetic field orientation respective to the crystal axes, Larmor peaks frequencies in SN spectra are shifted according to Equation 7.2.

$$\hbar\omega/\mu B_m = \sqrt{a + b\cos[2\alpha] + c\sin[2\alpha]} \tag{7.2}$$

The most pronounced peaks all reach the same minimum position, defined by the value of $g_{\perp}$ as

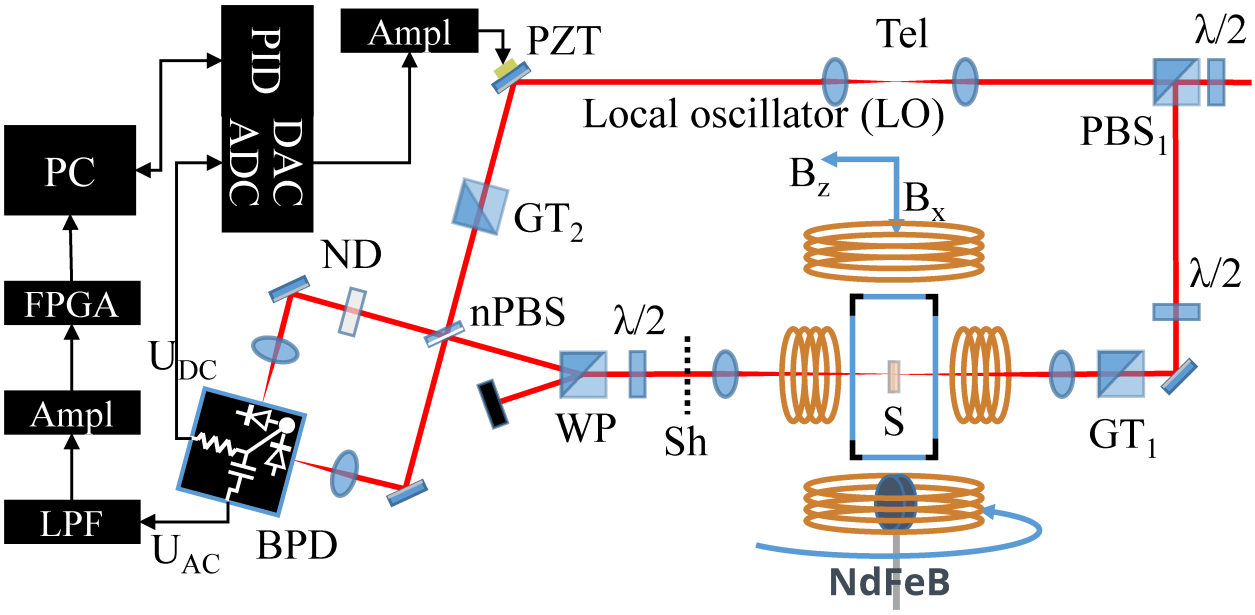

Figure 7.5. The homodyne-detection scheme with a constant amplitude rotating magnet field add-on. The latter is the only significant difference when comparing to Figure 5.1. The optical setup is still arranged as the Mach-Zehnder interferometer, with light splitting at PBS_1 into not yet signal-carrying probe path and local oscillator reference (LO) path. Due to the selection rules, scattered by the sample probing light has its polarization rotated by $90°$, which is easily separated by the Wollaston prism and routed for the interference with LO at 50:50 non-polarizing beam splitter (nPBS). The amplified signal is then detected by a broadband balanced photoreceiver, whose analogue high-frequency output is digitized and further processed by an FPGA-based spectrum analyzer board.

$\hbar\omega_i/\mu B_m = g_\perp, i = 1, 2, 3$.

The Equation 7.2 is a simplified form for curve fitting of an extensive theoretical description made by Kozlov and Zapasskii in Ref [36]. For the completeness of the physical picture it is reproduced below.

First of all, the system is a cubic crystal with anisotropic paramagnetic impurity centers, which can be modeled in the easiest way as putting the impurity at an arbitrary point of the elementary cell of the crystal and performing all the elements of the cubic group of symmetry. Such a group theory approach gives away all the equivalent points, which, due to the observed general isotropy of the crystal, should be populated uniformly with the dopant ions. Obviously, the number of orientationally distinguishable sites will depend on the local symmetry of the crystal in the chosen point: the lower the symmetry - the higher the number. As for the cubic crystal, this number may be 3 (tetragonal centers), 4 (trigonal centers), 6 (rhombic centers), and 12 or 24 (centers of lower symmetry). Each of these numbers (denote it N) denotes the number of magnetically non-equivalent centers of the appropriate symmetry. Keeping the number of impurities small enough to preserve the global cubic symmetry and taking into account high-temperature limit, the tensor χ of the static magnetic susceptibility ($\mathbf{M} = \chi\mathbf{B}$) is scalar, $\chi_{ik} = \chi_0\delta_{ik}$.

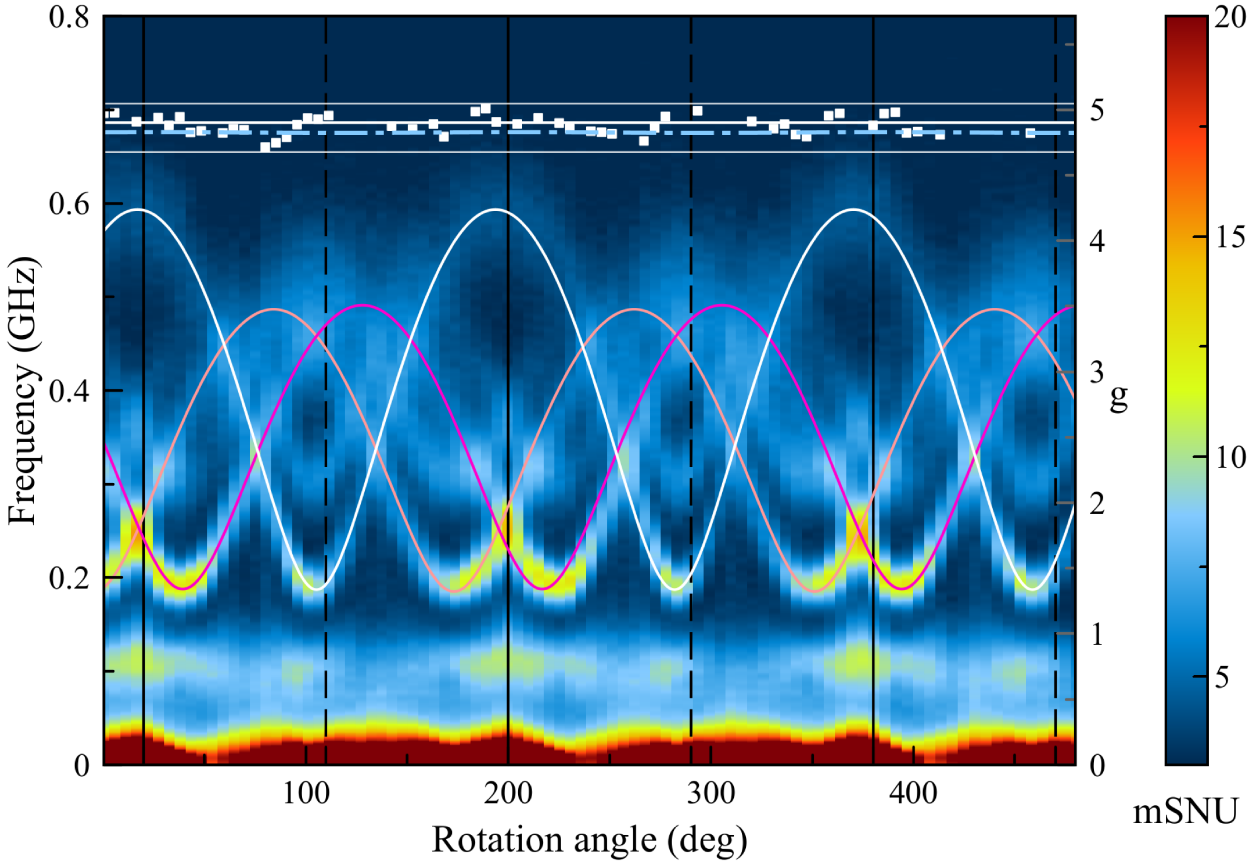

Figure 7.6. Spin noise spectra dependence on magnetic field orientation in the form of color map for the CaF_2:Nd^{3+} (0.1 %) crystal. The magnetic field was chosen to be 10 mT as a compromise between reliable peak resolution and limited by the component with highest slope bandwidth (see Figure 7.4). Dashed lines are experimental data fitted by $\hbar\omega/\mu B_m = \sqrt{a + b\cos[2\alpha] + c\sin[2\alpha]}$, the root of the sum of their squares at chosen angles is depicted as white points. The mean experimental value is solid white line and coincides well with the theoretically obtained dotted white line within the confidence interval (pale white stripe).

Let the superscript $\alpha = 1, 2, ..., N$ be an index for a group of magnetically equivalent centers, and the n be a concentration of the centers of each group. All of the partial magnetization components $\mathbf{M}^\alpha$ add up to to the full magnetization $\mathbf{M}$ of the system, each characterized by its own tensor χ^α:

$$M_i = \sum_{\alpha=1}^{N} M_i^\alpha = \sum_{\alpha=1}^{N} \chi_{ik}^\alpha B_k \Rightarrow \chi_{ik} = \sum_{\alpha=1}^{N} \chi_{ik}^\alpha \tag{7.3}$$

The summing of tensors of all the groups leads to total tensor χ of the crystal. The following evaluation of the tensor χ^α [2, 1] is provided to preserve the consistency. For an isolated center of a group the Hamiltonian is the scalar product of the operator of magnetic moment of the center $\mathbf{m}$ and the magnetic field vector $\mathbf{B}$: $H^\alpha = -m_i B_i$. The operator of the magnetic moment and the

operator of angular momentum (spin) **S** are connected through the symmetric g-tensor:

$$m_i = \mu g_{ik}^{\alpha} S_k, \tag{7.4}$$

where μ is the Bohr magneton. For the simplicity all paramagnetic centers accounted as two-level systems described by the effective spin $S = 1/2$, but the computations can be generalized to any spin. With that in mind, the spin operator matrices S_i turn into Pauli matrices, and the matrix H^{α} of the Hamiltonian of the center acquires the form:

$$\begin{aligned} H^{\alpha} &= -m_i B_i = -\mu g_{ik}^{\alpha} S_k B_i \equiv -\mu h_i^{\alpha} S_i, \\ |h^{\alpha}|^2 &= |B|^2 \left[(g_1^{\alpha})^2 \cos^2\theta_1 + (g_2^{\alpha})^2 \cos^2\theta_2 + (g_3^{\alpha})^2 \cos^2\theta_3 \right], \end{aligned} \tag{7.5}$$

h^{α} being the effective field, which amplitude is formulated in direction cosines ($\cos\theta_i, i = 1, 2, 3$) of the magnetic field in the diagonalizing eigenvector basis of the tensor g^{α} with principal values $g_i^{\alpha}, i = 1, 2, 3$. In the high-temperature limit, $\mu|h^{\alpha}| \ll k_B T$ (k_B is the Boltzmann constant),the equilibrium density matrix ρ^{α} can be written in the form:

$$\rho^{\alpha} = \frac{1 - \beta H^{\alpha}}{2}, \qquad \beta \equiv 1/k_B T. \tag{7.6}$$

The expected value of the i-th projection of the magnetization may be found like:

$$M_i^{\alpha} = n\mathrm{Sp}\rho^{\alpha} m_i = \frac{n\beta}{2}\mathrm{Sp}H^{\alpha} m_i = \frac{n\mu^2\beta}{2} B_j g_{jl}^{\alpha} g_{ik}^{\alpha} \overbrace{\mathrm{Sp}S_l S_k}^{\delta_{lk}/2}, \tag{7.7}$$

Sp being the trace of the matrix, and Kronecker symbol being the consequence of the orthogonality of Pauli matrices. Symmetry of the tensor g^{α} ($g_{ik}^{\alpha} = g_{ki}^{\alpha}$) allows the continuation of Equation 7.7:

$$M_i^{\alpha} = \frac{n\mu^2\beta}{4} g_{ik}^{\alpha} g_{kj}^{\alpha} B_j = \frac{n\mu^2\beta}{4} [g^{\alpha}]_{ij}^2 B_j = \chi_{ij}^{\alpha} B_j. \tag{7.8}$$

With the help of this relation, one can extract the expression for the tensor χ^{α}, and get by summing them up the magnetic susceptibility tensor of the whole crystal:

$$\chi^{\alpha} = \frac{n\mu^2\beta}{4}[g^{\alpha}]^2, \qquad \chi = \frac{n\mu^2\beta}{4}\sum_{\alpha=1}^{N}[g^{\alpha}]^2. \tag{7.9}$$

As noted in the starting assumptions, isotropy means $\chi_{ik} = \chi_0 \delta_{ik}$, where χ_0 is a scalar, so the above-mentioned sum must be scalar as well, $g_0^2 I$ (I is the unity matrix):

$$\sum_{\alpha=1}^{N}[g^{\alpha}]_{ik}^2 = g_0^2 \delta_{ik} \tag{7.10}$$

For the impurities in positions, that permute into each other under the symmetry transformations of the crystal, principal values of the g-tensors coincide $g_i^{\alpha} \equiv g_i, i = 1, 2, 3$, but the axis alignment does not. For such a situation the factor g_0^2 from Equation 7.10 may be decomposed into the

principal values of the g-tensors (g_1, g_2, and g_3) by taking the trace of the right- and left-hand sides of this formula:

$$g_0^2 = \frac{N}{3}[g_1^2 + g_2^2 + g_3^2] \tag{7.11}$$

As for the EPR resonance frequencies of the whole crystal, the α-th group of centers is responsible for a peak in the EPR spectrum at the frequency ω_α defined by the difference of eigenvalues of Hamiltonian (Equation 7.5): $\hbar\omega_\alpha = \mu|h^\alpha|$. Implementing the definition (Equation 7.5) for the components h_i^α of the effective field, the sum of squares of EPR frequencies can be written this way:

$$\begin{aligned}\sum_{\alpha=1}^{N}\omega_\alpha^2 = \frac{\mu^2}{\hbar^2}\sum_{\alpha=1}^{N}h_i^\alpha h_i^\alpha = \frac{\mu^2}{\hbar^2}\sum_{\alpha=1}^{N}g_{ik}^\alpha g_{ij}^\alpha B_k B_j = \\ = \frac{\mu^2}{\hbar^2}\sum_{\alpha=1}^{N}[g^\alpha]_{kj}^2 B_k B_j.\end{aligned} \tag{7.12}$$

A substitution of Equation 7.10 and Equation 7.11 gives the final formula:

$$\sum_{\alpha=1}^{N}\omega_\alpha^2 = \frac{N}{3}\left(\frac{\mu B}{\hbar}\right)^2[g_1^2 + g_2^2 + g_3^2]. \tag{7.13}$$

This way we got an analogous to the constant multidimensional squared Euclidean distance: the sum of squares of the EPR frequencies from all magnetically non-equivalent centers of the same type in a cubic crystal is invariant with respect to the magnetic field direction and is determined numerically by the sum of squares of the g-tensor components of these centers. With different types of centers, the amount of visualized lines raises, but for each type the invariant will be different. Generally, it does not stop the recognition from being ambiguous even for a cubic case, still the process is eased a lot. Noteworthy, Equation 7.12 may be rewritten to the form:

$$\sum_{\alpha=1}^{N}\omega_\alpha^2 = \frac{4}{n\beta\hbar^2}(\mathbf{M},\mathbf{B}), \quad \mathbf{M} \equiv \sum_{\alpha=1}^{N}\mathbf{M}^\alpha, \tag{7.14}$$

essentially meaning that independent of the crystal symmetry, the sum of squares of the EPR frequencies of paramagnetic centers is determined by the *projection* of the total magnetization **M** of these centers onto the magnetic field **B**. Therefore, a direct connection is given for the magnetization and EPR frequencies of the dopants in crystals with arbitrary symmetry. With the exception of cubic crystals, the sum is constant for uniaxial crystals if that the magnetic field is rotated in its "equatorial" plane.

Theoretical description of the observed EPR frequencies $\omega_i, i = 1,2,3$ for three groups of tetragonal centers in the experimental conditions look like:

$$\left(\frac{\hbar\omega_1}{\mu B_m}\right)^2 = g_\perp^2 + \frac{g_\parallel^2 - g_\perp^2}{2}\sin^2\Theta\left[1 + \cos 2\alpha\right] \tag{7.15}$$

$$\begin{aligned}\left(\frac{\hbar\omega_2}{\mu B_m}\right)^2 = \frac{g_\parallel^2 + g_\perp^2}{2} + \frac{g_\parallel^2 - g_\perp^2}{2}\times \\ \times\left[\left(\sin^2\Phi\cos^2\Theta - \cos^2\Phi\right)\cos 2\alpha + \sin 2\Phi\cos\Theta\ \sin 2\alpha - \sin^2\Phi\sin^2\Theta\right]\end{aligned} \tag{7.16}$$

$$\left(\frac{\hbar\omega_3}{\mu B_m}\right)^2 = \frac{g_\parallel^2 + g_\perp^2}{2} + \frac{g_\parallel^2 - g_\perp^2}{2} \times$$
$$\times \left[\left(\cos^2\Phi\cos^2\Theta - \sin^2\Phi\right)\cos 2\alpha - \sin 2\Phi\cos\Theta\,\sin 2\alpha - \cos^2\Phi\sin^2\Theta\right] \tag{7.17}$$

Where B_m is the modulus of the magnetic field, that does not change in that case. The angles Θ and Φ specify the orientation of the axis of rotation of the magnetic field in the crystal coordinate system. The angle α describes the rotation of the magnetic field in the plane perpendicular to the specified axis of rotation. Functions Equation 7.15 – Equation 7.17 are 180°-periodic and reaches minimum once per each 180°. As can be seen from the above expressions, all three minima are the same and are determined by the value of $g_\perp$ as $\hbar\omega_i/\mu B_m = g_\perp, i = 1, 2, 3$. These curves are depicted on the experimentally obtained color map.

To get the value of the motion integral, a precise study of the data was needed. All three groups having the same minima, close to $\omega_{min} = 2\pi \cdot 185 \cdot 10^6$ rad/sec (see Figure 7.6 made possible closer estimation of the real value B_m, $B_m = \hbar\omega_{min}/g_\perp\mu = 10\,\text{mT}$ (here $g_\perp = 1.301$). From Equation 7.15 – Equation 7.17, the spectral position of resonance peak is defined by $\hbar\omega/\mu B_m = \sqrt{a + b\cos[2\alpha] + c\sin[2\alpha]}$, where α is the angle of the magnetic field in the plane of its rotation.

7.3 Summary

This part of the work demonstrates *the gain factor*, which can turn the tiles of applicability of SNS for the RE paramagnetic impurities, extending the EPR spectroscopy with additional degrees of freedom, inaccessible in the classical implementation: optical access leads to the spectral selectivity and the focusing of the beam leads to the high spatial resolution in all dimensions. Continuing the comparison of the SNS to the conventional EPR, the absence of fixed-frequency source and ability to simultaneously obtain broadband spectra, no need in the state preparation and can be used in low magnetic fields. This benefit allowed us to show, that the sum of squares of the EPR frequencies for crystals with anisotropic paramagnetic centers is proportional to the projection of the magnetization of the centers onto the magnetic field. In case of cubic symmetry the magnetization is collinear to the applied field, and this sum stays constant upon rotation. The value of this constant is given through the impurity's g-tensor components and may be implemented for identification of the centers. With all these advantages, the SNS is promising for the development of the magnetic resonance spectroscopy of crystals and glasses with paramagnetic impurities.

Some results in chapter 7 are published in Ref [35], most of results in section 7.2 are published in Ref [36].

Bibliography

[1] A. Abragam and B. Bleaney. *Electron paramagnetic resonance of transition metal ions*. Clerendon Press, 1970. ISBN: 978-0-19-965152-8.

[2] S. A. Al'tshuler and B. M. Kozyrev, eds. *Electron Paramagnetic Resonance*. Academic Press, Jan. 1, 1964. ISBN: 978-1-4832-0053-8. DOI: 10.1016/B978-1-4832-0053-8.50001-8. URL: https://www.sciencedirect.com/science/article/pii/B9781483200538500018 (visited on 10/24/2022).

[3] E B Aleksandrov and Valerii S. Zapasskii. "Modulation magneto- optical spectroscopy of cross-relaxation resonances". In: 20 (1978), p. 679.

[4] Eugene Aleksandrov Alexandrov and Valerii Zapasskii. "Magnetic resonance in the Faraday-rotation noise spectrum". In: *Sov. Phys. JETP* 54 (Jan. 1981), p. 64.

[5] David L. Andrews. *Photonics, Volume 1: Fundamentals of Photonics and Physics*. New Jersey: Wiley, 2015. 472 pp. ISBN: 978-1-119-00971-9. URL: https://www.wiley.com/en-sg/Photonics%2C+Volume+1%3A+Fundamentals+of+Photonics+and+Physics-p-9781119009719 (visited on 10/12/2022).

[6] D. D. Awschalom, D. Loss, and N. Samarth, eds. *Semiconductor Spintronics and Quantum Computation*. Red. by Phaedon Avouris et al. NanoScience and Technology. Berlin, Heidelberg: Springer, 2002. ISBN: 978-3-642-07577-3 978-3-662-05003-3. DOI: 10.1007/978-3-662-05003-3. URL: http://link.springer.com/10.1007/978-3-662-05003-3 (visited on 10/12/2022).

[7] T. Basiev, A. Ya. Karasik, and V. V. Fedorov. "Optical echo spectroscopy and phase relaxation of Nd^{3+} ions in CaF$_2$ crystals". In: 86 (1998), p. 156.

[8] V. V. Belykh et al. "Electron charge and spin delocalization revealed in the optically probed longitudinal and transverse spin dynamics in n-GaAs". In: *Physical Review B* 96.24 (Dec. 7, 2017). Publisher: American Physical Society, p. 241201. DOI: 10.1103/PhysRevB.96.241201. URL: https://link.aps.org/doi/10.1103/PhysRevB.96.241201 (visited on 10/17/2022).

[9] V. V. Belykh et al. "Extended pump-probe Faraday rotation spectroscopy of the submicrosecond electron spin dynamics in n-type GaAs". In: *Physical Review B* 94.24 (Dec. 14, 2016). Publisher: American Physical Society, p. 241202. DOI: 10.1103/PhysRevB.94.241202. URL: https://link.aps.org/doi/10.1103/PhysRevB.94.241202 (visited on 10/16/2022).

[10] F. Bloch. "Nuclear Induction". In: *Phys. Rev.* 70.7 (Oct. 1946). Publisher: American Physical Society, pp. 460–474. DOI: 10.1103/PhysRev.70.460. URL: https://link.aps.org/doi/10.1103/PhysRev.70.460.

[11] A D Buckingham and P J Stephens. “Magnetic Optical Activity”. In: *Annual Review of Physical Chemistry* 17.1 (1966). _eprint: https://doi.org/10.1146/annurev.pc.17.100166.002151, pp. 399–432. DOI: 10.1146/annurev.pc.17.100166.002151. URL: https://doi.org/10.1146/annurev.pc.17.100166.002151.

[12] S. Cronenberger and D. Scalbert. “Quantum limited heterodyne detection of spin noise”. In: *Review of Scientific Instruments* 87.9 (Sept. 2016). Publisher: American Institute of Physics, p. 093111. ISSN: 0034-6748. DOI: 10.1063/1.4962863. URL: https://aip.scitation.org/doi/10.1063/1.4962863 (visited on 10/13/2022).

[13] S. Cronenberger et al. “Atomic-like spin noise in solid-state demonstrated with manganese in cadmium telluride”. In: *Nature Communications* 6.1 (Sept. 18, 2015). Number: 1 Publisher: Nature Publishing Group, p. 8121. ISSN: 2041-1723. DOI: 10.1038/ncomms9121. URL: https://www.nature.com/articles/ncomms9121 (visited on 10/13/2022).

[14] S. Cronenberger et al. “Spatiotemporal Spin Noise Spectroscopy”. In: *Physical Review Letters* 123.1 (July 2, 2019), p. 017401. ISSN: 0031-9007, 1079-7114. DOI: 10.1103/PhysRevLett.123.017401. URL: https://link.aps.org/doi/10.1103/PhysRevLett.123.017401 (visited on 10/12/2022).

[15] S. A. Crooker et al. “Spectroscopy of spontaneous spin noise as a probe of spin dynamics and magnetic resonance”. In: *Nature* 431.7004 (Sept. 2004). Number: 7004 Publisher: Nature Publishing Group, pp. 49–52. ISSN: 1476-4687. DOI: 10.1038/nature02804. URL: https://www.nature.com/articles/nature02804 (visited on 10/13/2022).

[16] S. A. Crooker et al. “Spin Noise of Electrons and Holes in Self-Assembled Quantum Dots”. In: *Physical Review Letters* 104.3 (Jan. 22, 2010). Publisher: American Physical Society, p. 036601. DOI: 10.1103/PhysRevLett.104.036601. URL: https://link.aps.org/doi/10.1103/PhysRevLett.104.036601 (visited on 10/13/2022).

[17] Scott A. Crooker, Lili Cheng, and Darryl L. Smith. “Spin noise of conduction electrons in n-type bulk GaAs”. In: *Physical Review B* 79.3 (Jan. 29, 2009). Publisher: American Physical Society, p. 035208. DOI: 10.1103/PhysRevB.79.035208. URL: https://link.aps.org/doi/10.1103/PhysRevB.79.035208 (visited on 10/13/2022).

[18] R. Dahbashi et al. “Measurement of heavy-hole spin dephasing in (InGa)As quantum dots”. In: *Applied Physics Letters* 100.3 (Jan. 16, 2012). Publisher: American Institute of Physics, p. 031906. ISSN: 0003-6951. DOI: 10.1063/1.3678182. URL: https://aip.scitation.org/doi/10.1063/1.3678182 (visited on 10/19/2022).

[19] Ramin Dahbashi et al. “Optical Spin Noise of a Single Hole Spin Localized in an (InGa)As Quantum Dot”. In: *Physical Review Letters* 112.15 (Apr. 14, 2014). Publisher: American Physical Society, p. 156601. DOI: 10.1103/PhysRevLett.112.156601. URL: https://link.aps.org/doi/10.1103/PhysRevLett.112.156601 (visited on 10/13/2022).

[20] “Discussion of ”A History of Some Foundations of Modern Radio-Electronic Technology””. In: *Proceedings of the IRE* 47.7 (1959), pp. 1253–1268. ISSN: 0096-8390. DOI: 10.1109/JRPROC.1959.287360. URL: http://ieeexplore.ieee.org/document/4065814/ (visited on 06/28/2023).

[21] R. I. Dzhioev et al. “Low-temperature spin relaxation in n-type GaAs”. In: *Physical Review B* 66.24 (Dec. 20, 2002). Publisher: American Physical Society, p. 245204. DOI: 10.1103/PhysRevB.66.245204. URL: https://link.aps.org/doi/10.1103/PhysRevB.66.245204 (visited on 10/19/2022).

[22] L. V. Fokina et al. “Spin dynamics of electrons and holes in $\text{InGaAs}/\text{GaAs}$ quantum wells at millikelvin temperatures”. In: *Physical Review B* 81.19 (May 4, 2010). Publisher: American Physical Society, p. 195304. DOI: 10.1103/PhysRevB.81.195304. URL: https://link.aps.org/doi/10.1103/PhysRevB.81.195304 (visited on 10/13/2022).

[23] M. Furis et al. “Bias-dependent electron spin lifetimes in n-GaAs and the role of donor impact ionization”. In: *Applied Physics Letters* 89.10 (Sept. 4, 2006). Publisher: American Institute of Physics, p. 102102. ISSN: 0003-6951. DOI: 10.1063/1.2345608. URL: https://aip.scitation.org/doi/full/10.1063/1.2345608 (visited on 03/23/2023).

[24] R. Giri et al. “Giant photoinduced Faraday rotation due to the spin-polarized electron gas in an ¡span class=”aps-inline-formula”¿¡math xmlns=”http://www.w3.org/1998/Math/MathML” display=”inline”¿¡mi¿n¡/mi¿¡/math¿¡/span¿-GaAs microcavity”. In: *Physical Review B* 85.19 (May 10, 2012). Publisher: American Physical Society, p. 195313. DOI: 10.1103/PhysRevB.85.195313. URL: https://journals.aps.org/prb/abstract/10.1103/PhysRevB.85.195313 (visited on 07/26/2022).

[25] P. Glasenapp et al. “Resources of polarimetric sensitivity in spin noise spectroscopy”. In: *Physical Review B* 88.16 (Oct. 24, 2013). Publisher: American Physical Society, p. 165314. DOI: 10.1103/PhysRevB.88.165314. URL: https://link.aps.org/doi/10.1103/PhysRevB.88.165314 (visited on 10/13/2022).

[26] Ph. Glasenapp et al. “Spin noise of electrons and holes in (In,Ga)As quantum dots: Experiment and theory”. In: *Physical Review B* 93.20 (May 19, 2016). Publisher: American Physical Society, p. 205429. DOI: 10.1103/PhysRevB.93.205429. URL: https://link.aps.org/doi/10.1103/PhysRevB.93.205429 (visited on 10/12/2022).

[27] M. M. Glazov and E. L. Ivchenko. “Spin noise in quantum dot ensembles”. In: *Physical Review B* 86.11 (Sept. 5, 2012). Publisher: American Physical Society, p. 115308. DOI: 10.1103/PhysRevB.86.115308. URL: https://link.aps.org/doi/10.1103/PhysRevB.86.115308 (visited on 10/12/2022).

[28] M. M. Glazov and V. S. Zapasskii. “Linear optics, Raman scattering, and spin noise spectroscopy”. In: *Optics Express* 23.9 (May 4, 2015), p. 11713. ISSN: 1094-4087. DOI: 10.1364/OE.23.011713. URL: https://opg.optica.org/abstract.cfm?URI=oe-23-9-11713 (visited on 10/13/2022).

[29] B. M. Gorbovitskii and V. I. Perel. “Aleksandrov and Zapasskii experiment and the Raman effect”. In: *Optics and Spectroscopy* 54.3 (Mar. 1983), pp. 229–230.

[30] T. P. J. Han, G. D. Jones, and R. W. G. Syme. "Site-selective spectroscopy of ${\mathrm{Nd}}^{3+}$ centers in ${\mathrm{CaF}}_{2}$:${\mathrm{Nd}}^{3+}$ and ${\mathrm{SrF}}_{2}$:${\mathrm{Nd}}
In: *Physical Review B* 47.22 (June 1, 1993). Publisher: American Physical Society, pp. 14706–14723. DOI: 10.1103/PhysRevB.47.14706. URL: https://link.aps.org/doi/10.1103/PhysRevB.47.14706 (visited on 10/25/2022).

[31] Jens Hübner et al. "The rise of spin noise spectroscopy in semiconductors: From acoustic to GHz frequencies". In: *physica status solidi (b)* 251.9 (2014). eprint: https://onlinelibrary.wiley.com/doi/pdf/10.
pp. 1824–1838. ISSN: 1521-3951. DOI: 10.1002/pssb.201350291. URL: https://onlinelibrary.wiley.com/doi/abs/10.1002/pssb.201350291 (visited on 10/13/2022).

[32] B. R. Judd. "Optical Absorption Intensities of Rare-Earth Ions". In: *Physical Review* 127.3 (Aug. 1, 1962). Publisher: American Physical Society, pp. 750–761. DOI: 10.1103/PhysRev.127.750. URL: https://link.aps.org/doi/10.1103/PhysRev.127.750 (visited on 10/25/2023).

[33] Brian Raymond Judd, W. A. Runciman, and Derek Ainslie Jackson. "Transverse Zeeman effect for ions in uniaxial crystals". In: *Proceedings of the Royal Society of London. A. Mathematical and Physical Sciences* 352.1668 (Jan. 1997). Publisher: Royal Society, pp. 91–108. DOI: 10.1098/rspa.1976.0165. URL: https://royalsocietypublishing.org/doi/10.1098/rspa.1976.0165 (visited on 07/13/2023).

[34] A. N. Kamenskii et al. "Detection and amplification of spin noise using scattered laser light in a quantum-dot microcavity". In: *Physical Review B* 101.4 (Jan. 2, 2020). Publisher: American Physical Society, p. 041401. DOI: 10.1103/PhysRevB.101.041401. URL: https://link.aps.org/doi/10.1103/PhysRevB.101.041401 (visited on 07/14/2023).

[35] A. N. Kamenskii et al. "Giant spin-noise gain enables magnetic resonance spectroscopy of impurity crystals". In: *Physical Review Research* 2.2 (June 11, 2020). Publisher: American Physical Society, p. 023317. DOI: 10.1103/PhysRevResearch.2.023317. URL: https://journals.aps.org/prresearch/abstract/10.1103/PhysRevResearch.2.023317 (visited on 07/11/2022).

[36] A. N. Kamenskii et al. "Invariants in the paramagnetic resonance spectra of impurity-doped crystals". In: *Physical Review B* 105.1 (Jan. 14, 2022). Publisher: American Physical Society, p. 014416. DOI: 10.1103/PhysRevB.105.014416. URL: https://link.aps.org/doi/10.1103/PhysRevB.105.014416 (visited on 07/14/2023).

[37] A. N. Kamenskii et al. "Nonlinear Faraday effect and spin noise in rare-earth activated crystals". In: *Physical Review B* 104.17 (Nov. 22, 2021). Publisher: American Physical Society, p. 174430. DOI: 10.1103/PhysRevB.104.174430. URL: https://journals.aps.org/prb/abstract/10.1103/PhysRevB.104.174430 (visited on 07/11/2022).

[38] Miros law Karbowiak, Czes law Rudowicz, and Jakub Cichos. "Extension of High-Resolution Optical Absorption Spectroscopy to Divalent Neodymium: Absorption Spectra of Nd2+ Ions in a SrCl2 Host". In: *Angewandte Chemie International Edition* 56.36 (2017). eprint: https://onlinelibrary.wiley.com/doi/pdf/10.1002/anie.201704559, pp. 10721–10724. ISSN: 1521-3773. DOI: 10.1002/anie.201704559. URL: https://onlinelibrary.wiley.com/doi/abs/10.1002/anie.201704559 (visited on 10/11/2023).

[39] Khaled Karrai and Richard J. Warburton. “Optical transmission and reflection spectroscopy of single quantum dots”. In: *Superlattices and Microstructures* 33.5 (May 2003), pp. 311–337. ISSN: 07496036. DOI: 10.1016/j.spmi.2004.02.007. URL: https://linkinghub.elsevier.com/retrieve/pii/S0749603604000114 (visited on 10/19/2022).

[40] J. M. Kikkawa and D. D. Awschalom. “Resonant Spin Amplification in n -Type GaAs”. In: *Physical Review Letters* 80.19 (May 11, 1998), pp. 4313–4316. ISSN: 0031-9007, 1079-7114. DOI: 10.1103/PhysRevLett.80.4313. URL: https://link.aps.org/doi/10.1103/PhysRevLett.80.4313 (visited on 03/23/2023).

[41] Robert H. Kingston. *Detection of Optical and Infrared Radiation*. Red. by David L. MacAdam. Vol. 10. Springer Series in Optical Sciences. Berlin, Heidelberg: Springer Berlin Heidelberg, 1978. ISBN: 978-3-662-15830-2 978-3-540-35948-7. DOI: 10.1007/978-3-540-35948-7. URL: http://link.springer.com/10.1007/978-3-540-35948-7 (visited on 10/12/2022).

[42] Šimon Kos et al. “Spin noise of itinerant fermions”. In: *Physical Review B* 81.6 (Feb. 9, 2010). Publisher: American Physical Society, p. 064407. DOI: 10.1103/PhysRevB.81.064407. URL: https://link.aps.org/doi/10.1103/PhysRevB.81.064407 (visited on 01/20/2022).

[43] G. G. Kozlov. “Noise spectroscopy of an optical microresonator”. In: *Journal of Experimental and Theoretical Physics* 116.5 (May 1, 2013), pp. 749–754. ISSN: 1090-6509. DOI: 10.1134/S1063776113040055. URL: https://doi.org/10.1134/S1063776113040055 (visited on 10/13/2022).

[44] G. G. Kozlov, I. I. Ryzhov, and V. S. Zapasskii. “Light scattering in a medium with fluctuating gyrotropy: Application to spin-noise spectroscopy”. In: *Physical Review A* 95.4 (Apr. 10, 2017). Publisher: American Physical Society, p. 043810. DOI: 10.1103/PhysRevA.95.043810. URL: https://link.aps.org/doi/10.1103/PhysRevA.95.043810 (visited on 10/13/2022).

[45] G. G. Kozlov, I. I. Ryzhov, and V. S. Zapasskii. “Spin-noise spectroscopy of randomly moving spins in the model of light scattering: Two-beam arrangement”. In: *Physical Review A* 97.1 (Jan. 29, 2018). Publisher: American Physical Society, p. 013848. DOI: 10.1103/PhysRevA.97.013848. URL: https://link.aps.org/doi/10.1103/PhysRevA.97.013848 (visited on 10/13/2022).

[46] G. G. Kozlov, V. S. Zapasskii, and I. I. Ryzhov. *Optical spin noise spectroscopy: application for study of gyrotropy spatial correlations*. Nov. 7, 2016. arXiv: 1611.02080[cond-mat]. URL: http://arxiv.org/abs/1611.02080 (visited on 10/12/2022).

[47] G. G. Kozlov, V. S. Zapasskii, and P. Yu Shapochkin. “Heterodyne detection of scattered light: application to mapping and tomography of optically inhomogeneous media”. In: *Applied Optics* 57.7 (Mar. 1, 2018). Publisher: Optica Publishing Group, B170–B178. ISSN: 2155-3165. DOI: 10.1364/AO.57.00B170. URL: https://opg.optica.org/ao/abstract.cfm?uri=ao-57-7-B170 (visited on 10/13/2022).

[48] G. G. Kozlov et al. “Raman scattering model of the spin noise”. In: *Optics Express* 29.4 (Feb. 15, 2021). Publisher: Optica Publishing Group, pp. 4770–4782. ISSN: 1094-4087. DOI: 10.1364/OE.415034. URL: https://opg.optica.org/oe/abstract.cfm?uri=oe-29-4-4770 (visited on 07/13/2023).

[49] Andreas V. Kuhlmann et al. “Charge noise and spin noise in a semiconductor quantum device”. In: *Nature Physics* 9.9 (Sept. 2013). Number: 9 Publisher: Nature Publishing Group, pp. 570–575. ISSN: 1745-2481. DOI: 10.1038/nphys2688. URL: https://www.nature.com/articles/nphys2688 (visited on 10/13/2022).

[50] J. M. LaForge and G. M. Steeves. “Noninvasive optical amplification and detection of Faraday rotation”. In: *Applied Physics Letters* 91.12 (Sept. 17, 2007). Publisher: American Institute of Physics, p. 121115. ISSN: 0003-6951. DOI: 10.1063/1.2785111. URL: https://aip.scitation.org/doi/10.1063/1.2785111 (visited on 10/13/2022).

[51] Joshua M. LaForge and Geoffrey M. Steeves. “A Mach–Zehnder interferometer for the detection and noninvasive optical amplification of polarization rotation”. In: *Review of Scientific Instruments* 79.6 (June 2008). Publisher: American Institute of Physics, p. 063106. ISSN: 0034-6748. DOI: 10.1063/1.2948309. URL: https://aip.scitation.org/doi/10.1063/1.2948309 (visited on 07/28/2022).

[52] M. D. Levenson and G. L. Eesley. “Polarization selective optical heterodyne detection for dramatically improved sensitivity in laser spectroscopy”. In: *Applied physics* 19.1 (May 1, 1979), pp. 1–17. ISSN: 1432-0630. DOI: 10.1007/BF00900531. URL: https://doi.org/10.1007/BF00900531 (visited on 10/12/2022).

[53] Yan Li et al. “Intrinsic Spin Fluctuations Reveal the Dynamical Response Function of Holes Coupled to Nuclear Spin Baths in (In,Ga)As Quantum Dots”. In: *Physical Review Letters* 108.18 (May 3, 2012). Publisher: American Physical Society, p. 186603. DOI: 10.1103/PhysRevLett.108.186603. URL: https://link.aps.org/doi/10.1103/PhysRevLett.108.186603 (visited on 10/12/2022).

[54] Guokui Liu and Bernard Jacquier. *Spectroscopic Properties of Rare Earths in Optical Materials*. Publication Title: Spectroscopic Properties of Rare Earths in Optical Materials ADS Bibcode: 2005spre.book.....L. Jan. 1, 2005. URL: https://ui.adsabs.harvard.edu/abs/2005spre.book.....L (visited on 10/25/2022).

[55] Vito Giovanni Lucivero et al. “Squeezed-light spin noise spectroscopy”. In: *Physical Review A* 93.5 (May 2, 2016). Publisher: American Physical Society, p. 053802. DOI: 10.1103/PhysRevA.93.053802. URL: https://link.aps.org/doi/10.1103/PhysRevA.93.053802 (visited on 10/13/2022).

[56] Roger M Macfarlane. “High-resolution laser spectroscopy of rare-earth doped insulators: a personal perspective”. In: *Journal of Luminescence* 100.1 (Dec. 1, 2002), pp. 1–20. ISSN: 0022-2313. DOI: 10.1016/S0022-2313(02)00450-7. URL: https://www.sciencedirect.com/science/article/pii/S0022231302004507 (visited on 10/22/2022).

[57] Neil B. Manson et al. “Hole burning of rare earth ions with kHz resolution”. In: *Journal of Luminescence*. Spectral Hole Burning and Related Spectroscopies 64.1 (May 1, 1995), pp. 19–23. ISSN: 0022-2313. DOI: 10.1016/0022-2313(95)00004-A. URL: https://www.sciencedirect.com/science/article/pii/002223139500004A (visited on 10/25/2022).

[58] Arnold S. Marfunin. *Spectroscopy, Luminescence and Radiation Centers in Minerals*. Berlin, Heidelberg: Springer Berlin Heidelberg, 1979. ISBN: 978-3-642-67114-2 978-3-642-67112-8. DOI: 10.1007/978-3-642-67112-8. URL: http://link.springer.com/10.1007/978-3-642-67112-8 (visited on 10/22/2022).

[59] Clemens Matthiesen, Anthony Nickolas Vamivakas, and Mete Atatüre. “Subnatural Linewidth Single Photons from a Quantum Dot”. In: *Physical Review Letters* 108.9 (Feb. 28, 2012). Publisher: American Physical Society, p. 093602. DOI: 10.1103/PhysRevLett.108.093602. URL: https://link.aps.org/doi/10.1103/PhysRevLett.108.093602 (visited on 10/19/2022).

[60] Bogdan Mihaila et al. “Quantitative study of spin noise spectroscopy in a classical gas of $^{41}\mathrm{K}$ atoms”. In: *Physical Review A* 74.4 (Oct. 30, 2006). Publisher: American Physical Society, p. 043819. DOI: 10.1103/PhysRevA.74.043819. URL: https://link.aps.org/doi/10.1103/PhysRevA.74.043819 (visited on 10/13/2022).

[61] W. B. Mims. “Phase Memory in Electron Spin Echoes, Lattice Relaxation Effects in CaW${\mathrm{O}}_{4}$: Er, Ce, Mn”. In: *Physical Review* 168.2 (Apr. 10, 1968). Publisher: American Physical Society, pp. 370–389. DOI: 10.1103/PhysRev.168.370. URL: https://link.aps.org/doi/10.1103/PhysRev.168.370 (visited on 10/25/2022).

[62] Georg M. Müller et al. “Gigahertz spin noise spectroscopy in n-doped bulk GaAs”. In: *Physical Review B* 81.12 (Mar. 31, 2010). Publisher: American Physical Society, p. 121202. DOI: 10.1103/PhysRevB.81.121202. URL: https://link.aps.org/doi/10.1103/PhysRevB.81.121202 (visited on 10/13/2022).

[63] H. S. Nguyen et al. “Ultra-coherent single photon source”. In: *Applied Physics Letters* 99.26 (Dec. 26, 2011). Publisher: American Institute of Physics, p. 261904. ISSN: 0003-6951. DOI: 10.1063/1.3672034. URL: https://aip.scitation.org/doi/10.1063/1.3672034 (visited on 10/19/2022).

[64] Mattias Nilsson et al. “Hole-burning techniques for isolation and study of individual hyperfine transitions in inhomogeneously broadened solids demonstrated in ${\mathrm{Pr}}^{3+}{:\mathrm
In: *Physical Review B* 70.21 (Dec. 30, 2004). Publisher: American Physical Society, p. 214116. DOI: 10.1103/PhysRevB.70.214116. URL: https://link.aps.org/doi/10.1103/PhysRevB.70.214116 (visited on 10/25/2022).

[65] M. Oestreich et al. “Spin Noise Spectroscopy in GaAs”. In: *Physical Review Letters* 95.21 (Nov. 17, 2005). Publisher: American Physical Society, p. 216603. DOI: 10.1103/PhysRevLett.95.216603. URL: https://link.aps.org/doi/10.1103/PhysRevLett.95.216603 (visited on 10/13/2022).

[66] Yuriy V. Pershin et al. “Two-beam spin noise spectroscopy”. In: *Applied Physics Letters* 102.20 (May 20, 2013). Publisher: American Institute of Physics, p. 202405. ISSN: 0003-6951. DOI: 10.1063/1.4807011. URL: https://aip.scitation.org/doi/10.1063/1.4807011 (visited on 10/12/2022).

[67] M. Yu. Petrov et al. “Increased sensitivity of spin noise spectroscopy using homodyne detection in n-doped GaAs”. In: *Physical Review B* 97.12 (Mar. 16, 2018). Publisher: American Physical Society, p. 125202. DOI: 10.1103/PhysRevB.97.125202. URL: https://link.aps.org/doi/10.1103/PhysRevB.97.125202 (visited on 07/14/2023).

[68] S. V. Poltavtsev et al. “Optics of spin-noise-induced gyrotropy of an asymmetric microcavity”. In: *Physical Review B* 89.20 (May 13, 2014). Publisher: American Physical Society, p. 205308. DOI: 10.1103/PhysRevB.89.205308. URL: https://link.aps.org/doi/10.1103/PhysRevB.89.205308 (visited on 10/13/2022).

[69] S. V. Poltavtsev et al. “Spin noise spectroscopy of a single quantum well microcavity”. In: *Physical Review B* 89.8 (Feb. 10, 2014). Publisher: American Physical Society, p. 081304. DOI: 10.1103/PhysRevB.89.081304. URL: https://link.aps.org/doi/10.1103/PhysRevB.89.081304 (visited on 10/13/2022).

[70] M. Römer, J. Hübner, and M. Oestreich. “Spatially resolved doping concentration measurement in semiconductors via spin noise spectroscopy”. In: *Applied Physics Letters* 94.11 (Mar. 16, 2009). Publisher: American Institute of Physics, p. 112105. ISSN: 0003-6951. DOI: 10.1063/1.3098074. URL: https://aip.scitation.org/doi/10.1063/1.3098074 (visited on 10/13/2022).

[71] M. Römer, J. Hübner, and M. Oestreich. “Spin noise spectroscopy in semiconductors”. In: *Review of Scientific Instruments* 78.10 (Oct. 2007). Publisher: American Institute of Physics, p. 103903. ISSN: 0034-6748. DOI: 10.1063/1.2794059. URL: https://aip.scitation.org/doi/10.1063/1.2794059 (visited on 10/13/2022).

[72] T. Rosenband et al. “Frequency Ratio of Al^+ and Hg^+ Single-Ion Optical Clocks; Metrology at the 17th Decimal Place”. In: *Science* 319.5871 (Mar. 28, 2008), pp. 1808–1812. ISSN: 0036-8075, 1095-9203. DOI: 10.1126/science.1154622. URL: https://www.science.org/doi/10.1126/science.1154622 (visited on 03/19/2023).

[73] I. I. Ryzhov et al. “Spin noise amplification and giant noise in optical microcavity”. In: *Journal of Applied Physics* 117.22 (June 14, 2015), p. 224305. ISSN: 0021-8979, 1089-7550. DOI: 10.1063/1.4922405. URL: http://aip.scitation.org/doi/10.1063/1.4922405 (visited on 10/12/2022).

[74] D. Scalbert. “Fundamental limits for nondestructive measurement of a single spin by Faraday rotation”. In: *Physical Review B* 99.20 (May 13, 2019). Publisher: American Physical Society, p. 205305. DOI: 10.1103/PhysRevB.99.205305. URL: https://link.aps.org/doi/10.1103/PhysRevB.99.205305 (visited on 10/19/2022).

[75] D. Scalbert. "Intrinsic limitation of cavity-enhanced Faraday detection of spin noise in quantum wells and quantum dots". In: *Superlattices and Microstructures* 92 (Apr. 1, 2016), pp. 348–352. ISSN: 0749-6036. DOI: 10.1016/j.spmi.2016.02.014. URL: https://www.sciencedirect.com/science/article/pii/S074960361630057X (visited on 10/12/2022).

[76] Bonny Schumaker. "Noise in homodyne detection". In: *Optics letters* 9 (June 1984), pp. 189–91. DOI: 10.1364/OL.9.000189.

[77] Marlan O. Scully and M. Suhail Zubairy. *Quantum Optics*. Cambridge: Cambridge University Press, 1997. ISBN: 978-0-521-43595-6. DOI: 10.1017/CBO9780511813993. URL: https://www.cambridge.org/core/books/quantum-optics/08DC53888452CBC6CDC0FD8A1A1 (visited on 10/10/2022).

[78] David S. Simon, Gregg Jaeger, and Alexander V. Sergienko. *Quantum Metrology, Imaging, and Communication*. Quantum Science and Technology. Cham: Springer International Publishing, 2017. ISBN: 978-3-319-46549-4 978-3-319-46551-7. DOI: 10.1007/978-3-319-46551-7. URL: http://link.springer.com/10.1007/978-3-319-46551-7 (visited on 10/12/2022).

[79] Nikolai A. Sinitsyn and Yuriy V. Pershin. "The theory of spin noise spectroscopy: a review". In: *Reports on Progress in Physics* 79.10 (Sept. 2016). Publisher: IOP Publishing, p. 106501. ISSN: 0034-4885. DOI: 10.1088/0034-4885/79/10/106501. URL: https://doi.org/10.1088/0034-4885/79/10/106501 (visited on 10/13/2022).

[80] D. S. Smirnov et al. "Measurement back action and spin noise spectroscopy in a charged cavity QED device in the strong coupling regime". In: *Physical Review B* 96.16 (Oct. 23, 2017). Publisher: American Physical Society, p. 165308. DOI: 10.1103/PhysRevB.96.165308. URL: https://link.aps.org/doi/10.1103/PhysRevB.96.165308 (visited on 10/13/2022).

[81] D. S. Smirnov et al. "Theory of spin inertia in singly charged quantum dots". In: *Physical Review B* 98.12 (Sept. 14, 2018). Publisher: American Physical Society, p. 125306. DOI: 10.1103/PhysRevB.98.125306. URL: https://link.aps.org/doi/10.1103/PhysRevB.98.125306 (visited on 10/19/2022).

[82] Pavel Sterin et al. "Optical Amplification of Spin Noise Spectroscopy via Homodyne Detection". In: *Physical Review Applied* 9.3 (Mar. 5, 2018). Publisher: American Physical Society, p. 034003. DOI: 10.1103/PhysRevApplied.9.034003. URL: https://link.aps.org/doi/10.1103/PhysRevApplied.9.034003 (visited on 10/13/2022).

[83] Y Sun et al. "Recent progress in developing new rare earth materials for hole burning and coherent transient applications". In: *Journal of Luminescence*. Proceedings of the Seventh International Meeting on Hole Burning, Single Molecules and Related Spectroscopies: Science and Applications 98.1 (July 1, 2002), pp. 281–287. ISSN: 0022-2313. DOI: 10.1016/S0022-2313(02)00281-8. URL: https://www.sciencedirect.com/science/article/pii/S0022231302002818 (visited on 10/25/2022).

[84] H.P. Yuen and V.W.S. Chan. "Noise in homodyne and heterodyne detection". In: *Opt. Lett.* 8 (Mar. 1983), pp. 177–179. DOI: 10.1364/OL.8.000177.

[85] I. A. Yugova et al. “Pump-probe Faraday rotation and ellipticity in an ensemble of singly charged quantum dots”. In: *Physical Review B* 80.10 (Sept. 29, 2009). Publisher: American Physical Society, p. 104436. DOI: 10.1103/PhysRevB.80.104436. URL: https://link.aps.org/doi/10.1103/PhysRevB.80.104436 (visited on 10/12/2022).

[86] V S Zapasskii and G G Kozlov. “Evolution in the optical detection of magnetization”. In: *Physics-Uspekhi* 60.6 (June 30, 2017), pp. 628–637. ISSN: 1063-7869, 1468-4780. DOI: 10.3367/UFNe.2016.10.037904. URL: https://iopscience.iop.org/article/10.3367/UFNe.2016.10.037904 (visited on 11/02/2022).

[87] V. S. Zapasskii. “Polarimetry of Regular and Stochastic Signals in Magnetooptics”. In: *Physics of the Solid State* 61.5 (May 1, 2019), pp. 847–852. ISSN: 1090-6460. DOI: 10.1134/S106378341905038X. URL: https://doi.org/10.1134/S106378341905038X (visited on 03/14/2022).

[88] V. S. Zapasskii and S. G. Przhibelskii. “Cavity-enhanced optical anisotropy and all-optical spin noise spectrometer”. In: *Optics and Spectroscopy* 110.6 (June 1, 2011), pp. 917–924. ISSN: 1562-6911. DOI: 10.1134/S0030400X11690038. URL: https://doi.org/10.1134/S0030400X11690038 (visited on 10/12/2022).

[89] V. S. Zapasskii et al. “Optical Spectroscopy of Spin Noise”. In: *Physical Review Letters* 110.17 (Apr. 23, 2013). Publisher: American Physical Society, p. 176601. DOI: 10.1103/PhysRevLett.110.176601. URL: https://link.aps.org/doi/10.1103/PhysRevLett.110.176601 (visited on 10/13/2022).

[90] Valerii S. Zapasskii. “Spin-noise spectroscopy: from proof of principle to applications”. In: *Advances in Optics and Photonics* 5.2 (June 30, 2013). Publisher: Optica Publishing Group, pp. 131–168. ISSN: 1943-8206. DOI: 10.1364/AOP.5.000131. URL: https://opg.optica.org/aop/abstract.cfm?uri=aop-5-2-131 (visited on 10/13/2022).